

Modelling waves and their impact on moored ships

Rijnsdorp, Dirk

DOI

[10.4233/uuid:c34395a2-43c8-44f2-bc13-01d42bec992e](https://doi.org/10.4233/uuid:c34395a2-43c8-44f2-bc13-01d42bec992e)

Publication date

2016

Document Version

Final published version

Citation (APA)

Rijnsdorp, D. (2016). *Modelling waves and their impact on moored ships*. [Dissertation (TU Delft), Delft University of Technology]. <https://doi.org/10.4233/uuid:c34395a2-43c8-44f2-bc13-01d42bec992e>

Important note

To cite this publication, please use the final published version (if applicable).
Please check the document version above.

Copyright

Other than for strictly personal use, it is not permitted to download, forward or distribute the text or part of it, without the consent of the author(s) and/or copyright holder(s), unless the work is under an open content license such as Creative Commons.

Takedown policy

Please contact us and provide details if you believe this document breaches copyrights.
We will remove access to the work immediately and investigate your claim.

MODELLING WAVES AND THEIR IMPACT ON MOORED SHIPS

MODELLING WAVES AND THEIR IMPACT ON MOORED SHIPS

Proefschrift

ter verkrijging van de graad van doctor
aan de Technische Universiteit Delft,
op gezag van de Rector Magnificus prof. ir. K. C. A. M. Luyben,
voorzitter van het College voor Promoties,
in het openbaar te verdedigen op woensdag 14 september 2016 om 15:00 uur

door

Dirk Pieter RIJNSDORP

civiel ingenieur
geboren te Haarlem, Nederland

Dit proefschrift is goedgekeurd door de

promotor: Prof. dr. J. D. Pietrzak
copromotor: Dr. ir. M. Zijlema

Samenstelling promotiecommissie:

Rector Magnificus,	voorzitter
Prof. dr. J. D. Pietrzak,	Technische Universiteit Delft, promotor
Dr. ir. M. Zijlema,	Technische Universiteit Delft, copromotor

Onafhankelijke leden:

Prof. dr. H. B. Bingham,	Danmarks Tekniske Universitet
Prof. dr. ir. R. H. M. Huijsmans,	Technische Universiteit Delft
Prof. ir. T. Vellinga,	Technische Universiteit Delft
Dr. F. Arduin,	Université de Bretagne Occidentale

Overige leden:

Prof. dr. ir. G. S. Stelling,	Technische Universiteit Delft
Prof. dr. ir. A. J. H. M. Reniers,	Technische Universiteit Delft, reservelid



Printed by: Gildeprint

Cover design: Jonathan Roorda

Copyright © 2016 by D.P. Rijnsdorp

An electronic version of this dissertation is available at
<http://repository.tudelft.nl/>

Panta rhei (alles stroomt)

– Heraclitus

ABSTRACT

Ships that are moored at a berth in coastal waters are subject to various external forcings, including the hydrodynamic loads that are induced by the local wave field. If the ship motions resulting from these wave-induced loads become too large, they may hamper safe operations (e.g., the loading of a container ship). Accurate predictions of the hydrodynamic loads are therefore desired to ensure safe operations of moored ships.

In a coastal environment, the wave field is generally dominated by short waves. The majority of these waves originate from the open ocean, where they are generated by the wind. If the short waves are energetic at a berth, they may cause a significant response of a moored ship. In addition, nonlinear wave effects can excite significant ship motions, which may even occur during relatively calm wave conditions or in a region that is sheltered from energetic short waves. This significant response is primarily related to the presence of infragravity waves, which are excited through nonlinear interactions amongst pairs of short waves. An accurate description of this nonlinear wave field is therefore indispensable when predicting the hydrodynamic loads that act on a ship which is moored in coastal waters.

The range of scales and physical processes involved in such studies make this a challenging problem to solve using numerical models. At present, the existing models that can predict the wave impact on a moored ship based on an offshore wave climate are restricted to relatively mild wave conditions. This thesis set out to develop a new modelling approach to advance our capabilities in solving this complex problem. The proposed model aims to be applicable at the scale of a realistic coastal or harbour region (say in the order of $1 \times 1 \text{ km}^2$), while accounting for the relevant physical processes. This includes the processes that govern the nonlinear wave evolution over a varying bottom topography (e.g., the nonlinear interactions that excite infragravity waves), and the interactions between the waves and a moored ship (e.g., the scattering of waves by a fixed floating body). The approach is based on the recently developed non-hydrostatic wave-flow model SWASH, which has been successfully applied to simulate a range of wave related processes. This work pursues the development of a new modelling approach through a further development and evaluation of the SWASH model in (i) simulating the nonlinear wave dynamics in a coastal region, and (ii) simulating the interactions between waves and a restrained ship.

The first crucial step in this development is to determine if the model can resolve the nonlinear wave field in a coastal environment. Previous studies showed that models like SWASH can resolve the short-wave dynamics in coastal waters. However, they did not address if such models can resolve the dynamics of the infragravity-wave field. Furthermore, most of these studies focussed on laboratory applications due to computational limitations, whereas field scale applications of non-hydrostatic models have been rarely reported. With the ever increasing computational capabilities, such scales are now within the reach of the state-of-the-art computer systems. To advance the capability of

the non-hydrostatic approach towards such realistic applications, this work presents a thorough evaluation of the SWASH model in resolving the nonlinear wave dynamics at the scale of a realistic coastal region. Given the importance of infragravity waves with respect to the wave-induced response of a moored ship, this work particularly determines if the model can resolve their nearshore evolution.

The model was validated using both laboratory and field experiments, covering a range of wave conditions (varying from bichromatic waves to short-crested sea states). A comparison between model predictions and laboratory measurements showed that the model captures the frequency dependent cross-shore evolution of infragravity waves with a coarse vertical resolution (2 layers), including their steepening and eventual breaking close to the shoreline. These results demonstrate that the model can efficiently resolve the dominant processes that affect their nearshore evolution (e.g., nonlinear interactions, shoreline reflections, and dissipation), permitting applications at the scale of a realistic harbour or coastal region.

To determine the capability of the model at such scales, SWASH was applied to study the infragravity wave dynamics at a field site near Egmond aan Zee (the Netherlands), which is characterised by a complex bottom topography. The model was used to reproduce a total of six sea states (including mild and storm conditions), which were measured as part of a two month field campaign. For all conditions, the predicted wave field gave a good representation of the natural conditions, supporting a further study into the infragravity wave dynamics. A unique feature of these predictions is their extensive spatial coverage, allowing analyses of the wave dynamics at scales not easily covered by in-situ measurement devices. Amongst others, this study showed that a significant portion (up to 50%) of the infragravity wave motion can be trapped at a nearshore bar. This shows the potential of the model to improve our understanding of such complex wave dynamics.

The findings of the flume and field studies further show that the SWASH model provides a powerful tool to predict the nonlinear wave field at a coastal berth based on an offshore wave climate. To predict the impact of this wave field on a ship that is moored at such a berth, the next crucial step in the model development is to account for the interactions between the waves and a restrained ship. For this purpose, a fixed floating body was schematised within SWASH. The model was validated by comparing model results with an analytical solution, a numerical solution, and two laboratory experiments that consider the wave impact on a restrained ship for a range of wave conditions (varying from a solitary wave to a short-crested wave field). These comparisons showed that the model captures the scattering of waves, and the hydrodynamic loads that act on the body. Remarkably, a coarse vertical resolution sufficed to resolve these dynamics. This shows the potential of the model in efficiently simulating the wave-ship interactions.

The findings of this thesis demonstrate that, with the inclusion of a fixed floating body in SWASH, a novel modelling approach has been developed that can efficiently resolve the key dynamics that govern the nearshore evolution of waves and their interactions with a restrained ship. Although further work is required, for example, accounting for the motions of a moored ship, this demonstrates the approach has the potential to simulate the wave-induced response of a ship that is moored in coastal waters. This thesis thereby sets the stage to advance our modelling capabilities towards such realistic applications in a complex coastal environment.

SAMENVATTING

Een schip dat is afgemeerd in een kustgebied wordt beïnvloed door een verscheidenheid aan externe factoren, waaronder de golf-geïnduceerde krachten. Wanneer de scheepsbewegingen door deze golven te groot worden belemmeren ze het laden en lossen van het schip. Nauwkeurige voorspellingen van de golfkrachten zijn daarom van groot belang om vast te stellen dat deze processen al dan niet ongestoord kunnen plaatsvinden.

In kustgebieden wordt het golfveld veelal gedomineerd door zogenaamde korte golven. Het merendeel van deze golven is afkomstig uit oceanen, waar ze worden opgewekt door de wind. Als deze golven energierijk zijn kunnen ze significante scheepsbewegingen veroorzaken. Naast deze korte golven kunnen niet-lineaire golfeffecten tevens voor ongewenste scheepsbewegingen zorgen. Deze problemen kunnen zelfs optreden gedurende kalme golfcondities, bijvoorbeeld in een haven die is afgeschermd van hoge golven. Dergelijke ongewenste bewegingen worden met name geassocieerd met de aanwezigheid van relatief lange golven, zogenaamde *infragravity waves*, welke worden gegenereerd door interacties tussen paren van korte golven. Om die reden is een nauwkeurige beschrijving van het niet-lineaire golfveld van groot belang wanneer men de krachten op een afgemeerd schip wenst te voorspellen.

De verscheidenheid aan fysische processen met uiteenlopende tijd- en ruimteschalen die van belang zijn in dergelijke studies maakt dit een uitdagend probleem om op te lossen met behulp van een computer model. De huidige generatie modellen die dit probleem kunnen oplossen zijn alleen geschikt voor relatief kalme golfcondities. Dit proefschrift stelt zich ten doel om een alternatieve numerieke methode te ontwikkelen, met het streven om ons begrip om dit complexe probleem op te lossen uit te breiden. Het te ontwikkelen model dient toepasbaar te zijn op de schaal van een realistisch kust of haven gebied (in de orde van $1 \times 1 \text{ km}^2$), en dient de relevante fysische processen te kunnen beschrijven. Dit betreft zowel de evolutie van het golfveld (inclusief de excitatie van de lange golven), als de interacties tussen de golven en het afgemeerde schip. Het in dit proefschrift ontwikkelde model is gebaseerd op het niet-hydrostatische model SWASH, dat tot nu toe succesvol is toegepast in verscheidene golf gerelateerde studies. Dit werk beschrijft de ontwikkeling van een nieuwe modeler techniek door middel van een verdere uitbreiding en validatie van het SWASH model in (i) het simuleren van de niet-lineaire golfdynamica in een kustgebied, en (ii) het simuleren van de interacties tussen de golven en een gefixeerd schip.

De eerste cruciale ontwikkeling is om te bepalen of het model een adequate weergave geeft van het niet-lineaire golfveld in een kustgebied. Voorgaande studies hebben aangetoond dat modellen zoals SWASH in staat zijn om de dynamica van de korte golven te beschrijven. De dynamica van de lange golven is echter nog niet onderzocht met behulp van dit soort modellen. Bovendien beperkten de meeste studies zich tot geïdealiseerde condities in, bijvoorbeeld, een golfgoot. Toepassingen op de schaal van een realistisch kustgebied zijn daarentegen slechts zelden uitgevoerd. Echter, met de continue ontwik-

keling van de computer technologie zijn zulke grootschalige toepassingen tegenwoordig uitvoerbaar op de meer geavanceerde computer systemen. Om de toepasbaarheid van het model voor zulke realistische applicaties in kaart te brengen, presenteert dit werk een nauwgezette validatie van het SWASH model in het simuleren van de niet-lineaire golfdynamica op de schaal van een realistisch kustgebied. Dit werk besteedt met name aandacht aan de correcte beschrijving van de lange golven, aangezien deze van groot belang zijn met betrekking tot de respons van een afgemeerd schip.

Het model was geverifieerd aan de hand van zowel proeven in golfgoten als een meetcampagne in het veld, welke een verscheidenheid aan golfcondities beslaan (variërend van bi-chromatische tot kortkammige golven). De vergelijkingen tussen de modelresultaten en de gootproeven toonden aan dat het model een nauwkeurige beschrijving geeft van de evolutie van het lange golfveld, inclusief het opstelen en breken van deze golven nabij de vloedlijn. Uit deze resultaten blijkt dat het model een correcte weergave geeft van de lange golfdynamica. Tevens maakt de efficiëntie waarmee dit model deze processen weergeeft grootschalige applicaties in een haven of kustgebied mogelijk.

Om het model op dergelijke schalen te toetsen was het toegepast om de lange golfdynamica bij de kust van Egmond aan Zee te bestuderen. In totaal zijn er zes golfcondities doorgerekend (variërend van milde tot stormachtige condities), welke eerder waren gemeten als onderdeel van een meetcampagne. Voor alle zes condities gaf het model een goede weergave van de gemeten golfcondities. Een bijzondere eigenschap van deze voorspellingen is dat ze een groot gebied beslaan, wat de mogelijkheid biedt om de golfdynamica te analyseren op een schaal die niet eenvoudig kan worden geïnstrumenteerd met behulp van in situ meetapparatuur. Aan de hand van de voorspellingen is onder meer aangetoond dat een significant gedeelte (tot wel 50%) van de lange golfbeweging gevangen kan zijn boven een zandbank. Dit demonstreert dat het model de mogelijkheid biedt om onze kennis van zulke complexe golfdynamica te vergroten.

De bevindingen van deze studies laten bovendien zien dat SWASH een effectief model is om het niet-lineaire golfveld ter plaatse van een afgemeerd schip te voorspellen aan de hand van een golfklimaat op zee. De volgende cruciale stap in de modelontwikkeling was om een gefixeerd drijvend object in het model te schematiseren, om zodoende de impact van de golven op het schip te kunnen simuleren. Het hiermee ontwikkelde model was gevalideerd aan de hand van een analytische oplossing, een numerieke oplossing, en twee lab experimenten die de golfimpact op een gefixeerd schip beschouwen voor een verscheidenheid aan golfcondities (variërend van een soliton tot kortkammige golven). Uit deze validatie blijkt dat het ontwikkelde model een correcte beschrijving geeft van de interacties tussen de golven en het schip, en de resulterende golfkrachten. Bovendien bleek dat het model deze interacties op een efficiënte wijze kan simuleren.

Met deze bevindingen presenteert dit proefschrift een nieuw model dat op een efficiënte manier zowel de evolutie van de golven als hun interacties met een gefixeerd schip kan simuleren. Alhoewel er meer werk nodig is, zoals het verdisconteren van de bewegingen van het afgemeerde schip, toont dit proefschrift aan dat deze aanpak de potentie heeft om de golf geïnduceerde respons van een afgemeerd schip te voorspellen. Hiermee legt dit werk de basis voor de uitbreiding van onze modelleer capaciteiten in de richting van dergelijke realistische applicaties in een complex kustgebied.

CONTENTS

Abstract	vii
Samenvatting	ix
1 Introduction	1
1.1 Background	1
1.2 Objective and outline	4
2 Modelling waves and their interactions with ships	7
2.1 Wave models	7
2.2 Wave-body interactions	12
2.3 Moored ships in coastal waters	14
3 Modelling infragravity waves at laboratory scales	17
3.1 Introduction	17
3.2 Numerical model	19
3.3 A second-order boundary condition to generate incident bound infragravity waves	22
3.4 Infragravity waves induced by bichromatic waves over a plane slope	23
3.5 Infragravity waves induced by random waves over a barred beach	30
3.6 Discussion	35
3.7 Conclusions	37
Appendices	37
3.A Second-order boundary condition	38
3.B SWASH second-order response	39
4 Modelling infragravity waves at field scales	41
4.1 Introduction	42
4.2 Methodology	43
4.3 Results: Model data comparison	52
4.4 Results: Infragravity wave dynamics	56
4.5 Discussion	63
4.6 Conclusions	64
Appendices	64
4.A Numerical wavemaker	65
4.B Second-order boundary condition	66
4.C Target wave conditions	67

5	Modelling waves and their interactions with a restrained ship	69
5.1	Introduction	70
5.2	Numerical Methodology	72
5.3	Scattering of linear monochromatic waves by a pontoon	83
5.4	Scattering of solitary wave by a pontoon	86
5.5	Scattering of regular waves by a pontoon	87
5.6	Wave impact on a container ship	89
5.7	Discussion	96
	Appendices	97
5.A	Porous flow	98
5.B	Quantitative model-data comparison.	98
5.C	Regular wave impact on a container ship	99
6	Conclusions and outlook	103
6.1	Conclusions.	103
6.2	Outlook	105
	Bibliography	109
	Acknowledgements	127
	List of publications	129
	Curriculum Vitæ	131

1

INTRODUCTION

1.1. BACKGROUND

Ships that are moored at a berth located in a harbour or coastal region are subject to a range of external forcing terms, which may cause the ship to move. For example, environmental conditions such as waves, currents and wind, but also the mooring system itself induce loads that act on a moored ship. If the ship motions resulting from these loads are large, they may hamper safe operations (e.g., loading of a container ship). In extreme environmental conditions, significant loads may even cause mooring lines to break. Such unfavourable conditions may require ships to leave the berth, resulting in undesired economic losses. Traditionally, berths have been located in sheltered regions to reduce the wave-induced response of a moored ship. However, recent developments have led to the construction of berths at locations that are exposed to more energetic waves. For example, the increase of the ship dimensions has resulted in the construction of berths which are located closer to the harbour entrance (e.g., Van der Molen, 2006), and the growth of the Liquefied Natural Gas industry has motivated the construction of marine terminals (e.g., De Jong et al., 2009). Furthermore, harbours and maritime terminals have to continuously improve their efficiency to cope with the increasing demand for maritime transport (e.g., González-Marco et al., 2008). This highlights that accurate predictions of the wave-induced loads and the resulting ship motions are desired to ensure safe and continuous operations.

In a harbour or coastal region, the wave field is generally dominated by waves with typical periods of 2-20 s, commonly referred to as short waves or wind generated waves (e.g., Holthuijsen, 2007). At exposed berths like maritime terminals, significant ship motions are expected in the case of energetic short waves. In contrast, the short-wave induced response of a moored ship is typically small at sheltered berths. However, the response of a moored ship is not only determined by the short waves. In coastal waters, nonlinear wave effects can also cause significant ship motions, which may even occur during relatively calm wave conditions in sheltered regions. This significant response is linked to the presence of so-called infragravity waves. Infragravity waves, with typical periods of 20 – 250 s, are generated through nonlinear interactions between pairs

of short waves (e.g., Longuet-Higgins and Stewart, 1960; Hasselmann, 1962; Symonds et al., 1982). At the typical water depths where ships are moored, their amplitudes are generally an order of magnitude smaller compared to the short waves. Despite their small amplitudes, infragravity waves can induce significant motions of a moored ship (e.g., González-Marco et al., 2008; Sakakibara and Kubo, 2008; López and Iglesias, 2014). This is primarily caused by the relative low frequency of infragravity waves, which may lie close to the natural frequency of a mooring system. If the frequencies approximately align, the waves cause a (near) resonant response of the moored ship. In addition, infragravity waves may cause harbour resonance (e.g., Bowers, 1977; Okihiro et al., 1993), which can adversely affect the operability of a harbour.

The foregoing illustrates that an accurate description of the nonlinear wave field at the berth is critical when predicting the wave-induced response of a ship that is moored in a coastal environment. In this context, two scales can be distinguished. In general, the majority of the waves that dominate the nearshore wave field originate from waves that are generated by the wind on the open ocean. After their generation on the ocean, a range of physical processes affect the evolution of the waves as they propagate in the shoreward direction. This includes processes like shoaling, refraction, diffraction, nonlinear interactions, and wave breaking (e.g., Holthuijsen, 2007). We refer to these wave related processes as the far field problem. In the vicinity of the ship, the physical processes that dominate the interactions between the waves and the moored ship are important, which we call the near field problem. These interactions occur on relatively small scale, and include the scattering of waves due to the presence of the ship, and the radiation of waves due to the motions of the floating body (e.g., Newman, 1977).

A vast body of literature exists that focusses on the numerical modelling of either the far field or the near field problem (see Chapter 2 for a comprehensive overview). To solve the far field problem, a number of wave models of varying complexity have been developed. These models can be grouped in two main model categories: the stochastic (phase-averaging) and the deterministic (phase-resolving) model class (e.g., Battjes et al., 2004).

Stochastic (or spectral) wave models describe the spatial and temporal variation of the wave field by means of the wave spectrum. They represent the wave dynamics such as the generation by wind, nonlinear interactions, and breaking of waves by so-called source terms, which rely on different levels of parametrisations. At ocean basin and regional scales, spectral models have been widely applied to simulate the evolution of waves in oceanic waters (e.g., Tolman, 1991; Booij et al., 1999; Holthuijsen, 2007). At present, they represent the only model class that is routinely applied at such large scales, and that accounts for the wind generation of waves. Stochastic models typically provide reasonable predictions of the bulk wave parameters, such as the significant wave height and mean wave period (e.g., Cavaleri et al., 2007). However, their inherent limitations restrict their applicability in coastal waters and harbour regions, where waves are nonlinear and inhomogeneous effects can be important. For example, they do not account for the excitation of infragravity waves, and do not intrinsically account for the effect of wave diffraction.

An alternative to the stochastic approach is the deterministic approach, which resolves the evolution of the individual waves rather than a spectral representation thereof.

Depending on the underlying formulations, such phase-resolving wave models can intrinsically account for a range of wave processes; including shoaling, refraction, diffraction, and nonlinear interactions. One of the first deterministic models that was able to resolve both refraction and diffraction effects over variable bottom topography is based on the mild-slope equations (Berkhoff, 1972). In their original form, mild-slope models are restricted to linear monochromatic waves and gently sloping bottoms. Since their introduction, efforts have been made to extend their applicability to resolve weak wave nonlinearity, the effect of wave breaking, and the evolution of short-crested wave fields (e.g., Kirby and Dalrymple, 1983, 1986; Chawla et al., 1998).

Besides mild-slope models, the nonlinear evolution of waves in a coastal environment can be simulated using the more advanced deterministic models based on the well known Boussinesq approach (e.g., Peregrine, 1967; Madsen and Sørensen, 1992; Wei et al., 1995; Bonneton et al., 2011) or the recently developed non-hydrostatic approach (e.g., Stelling and Zijlema, 2003; Yamazaki et al., 2009; Zijlema et al., 2011; Cui et al., 2012; Ma et al., 2012). These models can resolve the evolution of an arbitrary wave field (ranging from monochromatic to short-crested waves), and intrinsically account for the relevant processes that affect its nearshore transformation (although they necessarily parametrise some processes such as bottom friction, wave breaking, and lateral mixing). Such phase-resolving models require a significant computational effort compared to the stochastic wave models or mild-slope models. Nonetheless, advances in computer technology permit the use of such models at the typical scale of a coastal or harbour region (e.g., a spatial scale of $\mathcal{O}(10)$ wave lengths, and a temporal scale of $\mathcal{O}(100)$ wave periods). This makes them the most advanced modelling tool that is currently available to predict the nonlinear wave field at a coastal berth based on an offshore wave climate.

Admittedly, more detailed numerical models are available to simulate the evolution of waves in a coastal region. This includes models based on the Volume of Fluid (VOF) and Smooth Particle Hydrodynamic (SPH) approach. Such models have shown great potential in resolving the nonlinear wave dynamics in the surf zone, even including the turbulent details of a breaking wave (e.g., Lin and Liu, 1998; Dalrymple and Rogers, 2006; Farahani and Dalrymple, 2014; Zhou et al., 2014). However, they are not applicable at the spatial and temporal scales that are considered in this thesis, as computational limitations restrict their application to scales of a few wave lengths and wave periods.

To solve the interactions between waves and floating bodies, numerous near field models have been developed (see Bertram, 2012, for a concise overview). The first effort to simulate such interactions were based on potential flow theory in which the flow is assumed to be irrotational and inviscid (e.g., Korvin-Kroukovsky and Jacobs, 1957; Hess and Smith, 1962). In this context, the Boundary Element Method (BEM) has been a popular method to solve the potential flow equations, in which the flow problem is mapped onto the boundaries of the fluid (e.g., the hull of the ship). To simulate the wave-ship interactions, numerous BEM models (which are also known as panel models) have been developed that vary in complexity. Amongst others, this includes panel models based on linear, higher-order, and fully nonlinear potential theory (e.g., Eatock Taylor and Chau, 1992; Liu et al., 2001; You and Faltinsen, 2015). More recently, models based on the Finite Element Method (FEM) have been developed to solve the nonlinear potential flow problem (e.g., Ma et al., 2001a; Ma and Yan, 2009). In contrast with the BEM, the whole fluid

domain is discretised in the FEM. These potential flow models share that they rely on predictions of the wave field in the vicinity of the ship as they are not designed to simulate the evolution of waves at relatively large scales. Furthermore, they are not suited for large wave impacts and significant ship motions, when the assumptions of potential flow are violated.

In such conditions, an alternative approach is required to simulate the interactions between waves and ships. With the continuous increase of computational powers, various models have been developed that can resolve the turbulent flow field in the vicinity of a ship. This includes models based on the Reynolds averaged Navier Stokes (RANS) equations (e.g., Hadžić et al., 2005; Wilson et al., 2006; Stern et al., 2013; Mousaviraad et al., 2016), and SPH models (e.g., Bouscasse et al., 2013; Ren et al., 2015). For example, such models have shown great potential in resolving the self propelled seakeeping of ships, including the detailed flow patterns in the wake of a rotating propeller (e.g., Carrica et al., 2010; Mofidi and Carrica, 2014). Due to their great complexity, computational restraints limit the application of such detailed models to scales of a few wave lengths and periods. At present, they are therefore primarily suited to solve the near field problem.

In contrast to the vast body of literature that focusses on either the far field or the near field problem, less research attempted to solve the combined problem. To solve this complicated problem, the most advanced method presented so far combined a Boussinesq or non-hydrostatic model with a panel model based on linear potential theory (Bingham, 2000; Van der Molen and Wenneker, 2008; Dobrochinski, 2014). This coupled approach combines the advantages of both methods: The wave model captures the nonlinear evolution of waves in a coastal or harbour region, and the panel model accounts for the interactions between the waves and the moored ship. However, the wave-ship interactions are computed using linear potential theory, which restricts this approach to weakly nonlinear wave conditions.

For more energetic waves, a more accurate – but computationally intensive – near field model is required to accurately simulate the wave-ship interactions. For example, panel models based on nonlinear potential theory or RANS models can be used to resolve these interactions. Although such near field models are available, they were not used in conjunction with a wave model to solve the combined problem. Consequently, predictions of the wave-induced response of a moored ship in coastal waters are restricted to relatively mild wave conditions (e.g., when a ship is moored in a harbour basin).

1.2. OBJECTIVE AND OUTLINE

This thesis pursues an alternative approach to solve the combined far and near field problem. The ultimate goal is to develop a single model that can simulate the wave-induced response of a ship that is moored in coastal waters based on an offshore wave climate. In this context, an accurate description of the nonlinear wave field and the hydrodynamic loads that act on a restrained (i.e., non-moving) ship are of vital importance. The aim of this thesis is to develop a new model that seamlessly accounts for the evolution of waves, and their impact on a restrained ship. The model aims to be applicable at the scale of a realistic harbour or coastal region, while accounting for the relevant pro-

cesses that determine the wave-induced loads on a restrained ship. This includes the processes that affect the evolution of waves in coastal waters, and the processes that govern the interactions between the waves and a fixed floating body.

Given the importance of accurately describing the nonlinear wave field, the model is based on the non-hydrostatic approach. More specifically, this work is based on the recently developed non-hydrostatic wave-flow model SWASH¹ (Zijlema et al., 2011). This thesis works towards the development of a new modelling approach through (i) a further development and evaluation of the SWASH model in resolving the nonlinear wave dynamics in a coastal environment, and (ii) a further development of the model to account for the interactions between the waves and a restrained ship.

So far, several studies demonstrated the capability of the non-hydrostatic approach in simulating the evolution of nonlinear waves over variable bottom topographies (e.g., Ma et al., 2012; Smit et al., 2013, 2014). However, these studies focussed on the nearshore evolution of the short waves and their super harmonics, but did not address the evolution of infragravity waves. Furthermore, such studies primarily focussed on laboratory conditions, whereas field scale applications have not been widely reported due to computational limitations. With the ever increasing computational capabilities, such field scale applications are now feasible on multi-core computer systems. To advance the capability of the non-hydrostatic approach, this work evaluates the potential of the SWASH model in resolving the nonlinear wave dynamics, and in particular the infragravity wave field, in a realistic coastal region.

The structure of this thesis is as follows. First, Chapter 2 discusses the computational tools that have been developed to simulate the evolution of waves in coastal waters, and to simulate the wave-ship interactions. This chapter, in combination with the present chapter, provides the background and the motivation of this thesis.

The two following chapters, Chapter 3 and 4, focus on the modelling of the nonlinear wave transformation in a coastal region. Given the importance of infragravity waves with respect to the wave-induced response of a moored ship, Chapters 3 and 4 address the ability of SWASH in resolving the evolution of infragravity waves in a coastal environment. First, Chapter 3 presents a thorough assessment of the model capability in resolving the cross-shore evolution of infragravity waves over a sloping bottom. The model was used to reproduce two flume experiments, which cover the evolution of bichromatic wave groups over a plane beach, and the evolution of spectral waves over a barred beach. Chapter 4 continues on this work, and presents a field scale application of the model to study the nearshore evolution of infragravity waves at a natural site.

Subsequently, Chapter 5 presents a further development of the SWASH model to resolve the wave-ship interactions. To account for the interactions between the waves and a restrained ship, a fixed floating body was schematised in the numerical domain. The model was verified using an analytical solution, a numerical solution, and two experimental campaigns that were conducted in a wave basin. These four test cases consider the wave impact on a restrained ship, and focus on the wave scattering and the hydrodynamic loads that act on the body.

In Chapter 6, the conclusions of the individual chapters are summarised, followed by

¹Simulating WAves till SHore (SWASH), available under the GNU GPL license at <http://swash.sourceforge.net/>.

a discussion concerning the implications of this work. This chapter finishes with an outlook for future developments that concern the non-hydrostatic modelling of nonlinear waves and their impact on moored ships.

2

MODELLING WAVES AND THEIR INTERACTIONS WITH SHIPS

This chapter presents an overview of the computational methods that have been developed to simulate waves, and their interactions with moored ships. Research into this topic has typically focussed on one of the two fields, that is, either the modelling of waves, or the modelling of wave-ship interactions. The first two sections of this chapter discuss the separate developments in these two fields. This is followed by a section that presents an overview of several recent studies that attempted to bridge the gap between these two fields, including an introduction to the methodology that has been developed in this thesis, in order to predict the wave-induced response of a moored ship in coastal waters.

2.1. WAVE MODELS

During the past decades, various modelling techniques have been developed to simulate the evolution of waves over variable bottom topographies. These models can be grouped into two main model classes: the deterministic and the stochastic model class (e.g., Battjes, 1994). Deterministic models solve the basic equations (i.e., the Navier Stokes (NS), or the Euler equations), or simplifications thereof (e.g., the RANS equations, and linear potential theory). They resolve the evolution of the individual waves, while accounting for a number of physical processes that affect their dynamics, depending on the assumptions of the underlying equations. As an alternative to directly solving the deterministic equations, stochastic evolution equations can be derived from the basic equations. The resulting stochastic wave models do not resolve the evolution of the individual waves, but describe the spatial and temporal variation of statistical wave properties (e.g., the wave spectrum).

STOCHASTIC WAVE MODELS

Present-day operational stochastic wave models (or spectral wave models) are based on the assumption that the waves can be represented by a quasi-homogeneous and a quasi-stationary Gaussian process. With this assumption, the wave field is fully described by the variance density spectrum, and its spatial and temporal evolution can be solved by means of the action balance equation (e.g., Holthuijsen, 2007). This equation includes so-called source terms, which account for the effect of various wave related processes. Over the past decades, a number of source terms have been developed (based on varying degrees of parametrisations) to account for most relevant physical processes that occur in oceanic and coastal waters. This includes processes like wave generation by wind (e.g., Miles, 1957; Phillips, 1957), white capping (e.g., Hasselmann, 1974), nonlinear wave interactions (e.g., Hasselmann and Hasselmann, 1985; Eldeberky, 1996), and wave breaking (e.g., Battjes and Janssen, 1978; Janssen and Battjes, 2007; Salmon et al., 2015).

So far, most studies focussed on the development and improvement of the source terms, whereas the underlying assumptions of the action balance equation remained unchanged (i.e., a near homogeneous Gaussian wave field). Recently, Smit et al. (2013) derived an extension of the action balance equation to resolve coherent wave effects like refractive wave focussing. Although this approach successfully simulated coherent effects on the bulk wave statistics for waves propagating over a variable bottom topography (Smit et al., 2015a,b), it assumes that depth variations are small with respect to a wave length. Consequently, this approach does not intrinsically resolve diffraction effects caused by the presence of breakwaters (which can be interpreted as strong bottom variations).

Since their introduction, stochastic models have been widely applied for research and engineering purposes (e.g., Tolman, 1991; Booij et al., 1999; Holthuijsen, 2007), and have been successfully used to predict the (bulk) wave statistics in oceanic and coastal regions (e.g., Cavaleri et al., 2007). At present, stochastic models represent the only model class that is routinely used at the scale of an ocean basin, and which can include the effect of wind generation (albeit parametrised). However, the assumptions of a (quasi) homogeneous and Gaussian wave field restricts their validity in coastal regions (where waves are nonlinear), and in harbour regions (where coherent effects, such as wave diffraction can be important).

Furthermore, stochastic models do not account for the excitation and propagation of infragravity waves. To account for the effect of these waves on processes in a coastal region (e.g., dune erosion), several authors combined a (stochastic) wave group model with a deterministic model based on the Nonlinear Shallow Water Equations (NSWE) (e.g., Van Dongeren et al., 2003; Reniers, 2004; Roelvink et al., 2009). In this approach, the stochastic model, which accounts for the evolution of short-wave groups over a variable bottom topography, provides the forcing for the deterministic model that resolves the evolution of infragravity waves. However, the use of a stochastic approach to resolve the short-wave groups implies that this methodology does not fully capture nonlinear wave effects, and does not account for wave diffraction. For a more complete description of the nonlinear wave field, deterministic models that solve the basic equations are preferable over the stochastic approach.

DETERMINISTIC WAVE MODELS

Numerous deterministic models have been developed to resolve the evolution of waves in a coastal region. With the introduction of digital computers in the second half of the 20th century, the first efforts were made to solve the deterministic equations, but the computational power at that time was not sufficient to directly solve the basic equations. To cope with this limitation, the first deterministic models were based on simplifications of the basic equations (e.g., Peregrine, 1967; Berkhoff, 1972; Hibberd and Peregrine, 1979).

To simplify the problem, the equations were typically scaled using two wave parameters. The first parameter represents the frequency dispersion of the waves, which is expressed as the ratio of the water depth h over the wave length L ($\mu = h/L$). The second parameter characterises the wave nonlinearity as the ratio of the wave amplitude a over the water depth ($\delta = a/h$). In coastal waters, dispersive effects weaken as the water depth decreases, $\mu \rightarrow 0$, whereas nonlinear effects become increasingly important, $\delta \rightarrow \mathcal{O}(1)$. If the wave nonlinearity dominates, the basic equations reduce to the NSWE. Models based on the NSWE can be used to simulate the wave evolution in shallow water, including breaking waves and the wave run-up at the shoreline (e.g., Hibberd and Peregrine, 1979; Kobayashi et al., 1989). However, this approach is not valid in progressively deeper water, where nonlinear effects weaken and dispersive effects become significant.

The former condition gave rise to one of the first deterministic methods that was able to resolve both refraction and diffraction effects over a variable bottom topography (Berkhoff, 1972). This method is based on the Mild Slope Equation (MSE), which is derived from linear potential theory assuming that the vertical variation of the wave motion on a sloping bottom can be described by the linear wave theory for a constant depth (e.g., Dingemans, 1994). This assumption holds if the mild slope condition is satisfied: $\beta_h/kh \ll 1$, where β_h is the bottom slope, and k is the wavenumber. The MSE describes the evolution of a monochromatic wave over mildly sloping bottoms, without any restrictions concerning μ . Several extensions of the MSE have been proposed to resolve, for example, weak wave nonlinearity (e.g., Kirby and Dalrymple, 1983), the effect of wave breaking (e.g., Kirby and Dalrymple, 1986), and the evolution of spectral waves (e.g., Chawla et al., 1998). Such developments have led to the formulation of various mild slope models, which have been typically used for engineering purposes, and, in particular, to study the wave agitation in a harbour region (e.g., Morison and Imberger, 1992; Panchang et al., 2000; Diaz-Hernandez et al., 2015).

However, in relatively shallow water depths, mild slope models do not give a proper description of the wave field as they assume that δ is small. To accurately resolve the wave dynamics in a nearshore region, a model has to account for both the nonlinear and the dispersive effects. Assuming that nonlinear effects are small and of similar importance as dispersive effects, $\delta = \mathcal{O}(\mu^2)$, Peregrine (1967) derived the classical Boussinesq formulation to simulate the evolution of waves over a sloping bottom.¹ The resulting equations are almost identical to the NSWE, but include some additional terms that account for the wave dispersion. However, this classical formulation breaks down when nonlinear wave effects become significant, for example, in coastal regions where waves

¹The classical Boussinesq formulation can be derived from the Euler equations by using a power series to remove the vertical dependence of the flow, and omitting the terms of $\mathcal{O}(\delta\mu^2)$ and higher (e.g., Kirby, 1997).

are breaking.

Since the pioneering work of Peregrine (1967), the applicability of the Boussinesq approach was extended towards realistic coastal applications (e.g., Kirby, 2003; Brocchini, 2013). This includes various extensions that pushed their capabilities towards the coast, where waves become nonlinear, break, and inundate the shore. To capture the nonlinear evolution of the wave field, the original assumption of weak nonlinearity was relaxed with the derivation and development of fully nonlinear Boussinesq models (e.g., Wei et al., 1995; Bonneton et al., 2011). Furthermore, various parametrisations were suggested to account for the bulk dissipation of a breaking wave (e.g., Karambas and Koutittas, 1992; Schäffer et al., 1993; Tonelli and Petti, 2012), and several numerical techniques were developed to capture the wave runup at the shore (e.g., Zelt, 1991; Kennedy et al., 2000; Lynett et al., 2002). Besides a push towards shallower water, several authors extended the Boussinesq framework towards deeper water (or shorter waves), by deriving new sets of Boussinesq equations with improved dispersive properties (e.g., Madsen and Sørensen, 1992; Lynett and Liu, 2004).

Since their introduction, various Boussinesq-type wave models have been developed to simulate the evolution of waves in a coastal environment, of which the accuracy depends on the underlying formulations (e.g., weakly nonlinear versus fully nonlinear equations). They have been widely used for scientific and engineering purposes to simulate waves (and their related processes) in a coastal environment (e.g., Kirby, 2003; Brocchini, 2013). Their success is in part related to their computational efficiency, as only the horizontal domain needs to be discretised. This allows for simulations of the wave dynamics at relatively large spatial scales of $\sim 1 \times 1$ km. For example, Boussinesq models have been used to simulate wave oscillations in a harbour region (e.g., Abbott et al., 1978), the evolution of waves over variable bottom topography (e.g., Madsen et al., 1997), and wave-induced currents in a coastal environment (e.g., Chen et al., 1999; Feddersen, 2014).

With the ever increasing computational powers, new modelling techniques were developed that solve the basic equations, rather than simplifications thereof. Such models solve the (RA)NS equations on fine spatial and temporal scales, and intrinsically account for the relevant processes that govern the nearshore evolution of waves. This includes processes like shoaling, refraction, diffraction, nonlinear interactions and wave breaking. Several methodologies were developed to solve the RANS equations, which mainly differ in the treatment of the free surface. Several techniques have been proposed to capture the free surface, for example, the marker and cell method (e.g., Harlow and Welch, 1965), the VOF method (Hirt and Nichols, 1981), and the level set method (e.g., Osher and Sethian, 1988). As an alternative to such models which are solved on a computational mesh, the meshfree SPH method was developed more recently, which computes the trajectory of particles of fluid that interact based on the NS equations (Monaghan, 1994).

Such detailed models have been successfully applied to simulate the evolution of waves in the surf zone (e.g., Lin and Liu, 1998; Dalrymple and Rogers, 2006; Farahani and Dalrymple, 2014; Zhou et al., 2014). However, solving the wave dynamics at such great detail requires a significant computational effort. At present, computational limitations restrict such models to relatively small scales (e.g., a spatial scale of a few wave

lengths and a time scale of a few wave periods). Barring revolutionary developments in computing techniques (e.g., the quantum computer), such methods will likely remain restricted to small scales in the foreseeable future.

As an alternative to solving the RANS equations while accounting for the complex dynamics of the free surface in the presence of, for example, breaking waves; a significant simplification can be made by assuming that the free surface can be represented by a single valued function. This simplification has led to the development of the so-called non-hydrostatic approach, which provides a more efficient method to solve the RANS equations (Mahadevan et al., 1996; Stansby and Zhou, 1998; Casulli and Stelling, 1998). Non-hydrostatic models have been developed to simulate a variety of physical processes, including both barotropic (e.g., Casulli and Stelling, 1998; Fang et al., 2015) and baroclinic applications (e.g., Marshall et al., 1997; Vitousek and Fringer, 2014). The following focusses on the developments that have been pursued to simulate the evolution of surface waves.

In the non-hydrostatic approach, a fractional step technique is used to solve the pressure field. With this technique, a provisional velocity field is first computed based on the NSWE (in which the pressure is assumed to be hydrostatic), followed by a correction of the velocities by solving a Poisson type equation for the non-hydrostatic pressure (to ensure that the velocity field is divergence free). The accuracy with which the non-hydrostatic approach resolves the nonlinear wave dynamics primarily depends on the grid resolution. In horizontal direction, this imposes similar requirements on the grid resolution as Boussinesq type models (which is determined by the wave length of interest). In the vertical direction, the use of standard numerical techniques would require fine vertical resolutions (in the order of 10 vertical layers) to resolve the wave dynamics. Such vertical resolutions imply a significant computational effort, and would make non-hydrostatic models an order of magnitude slower compared to Boussinesq-type wave models.

To improve the efficiency of the method in resolving the wave dynamics, Stelling and Zijlema (2003) proposed to use the Keller-box scheme (Lam and Simpson, 1976) to discretise the vertical non-hydrostatic pressure gradient. In this scheme, the non-hydrostatic pressure is positioned at a cell face, which allows for a straightforward inclusion of the zero pressure condition at the free surface. With this scheme, Stelling and Zijlema (2003) found that a coarse vertical resolution (1 – 3 layers) is sufficient to capture the dispersion of waves in coastal waters.

However, a non-hydrostatic wave model based on these principles does not necessarily capture the discontinuities of the flow field that are associated with a breaking wave, and the wave runup at the shoreline. To capture such discontinuities, the governing equations must be solved by means of a shock capturing numerical scheme (e.g., Stelling and Duijnmeijer, 2003; Yamazaki et al., 2009; Ma et al., 2012). Although a shock capturing non-hydrostatic model does not resolve the detailed dynamics of a breaking wave (e.g., wave overturning, and wave generated turbulence), it does capture the initiation and subsequent dissipation of a breaking wave without the need for any additional model parameters (Smit et al., 2013). However, a fine vertical resolution (10 – 20 layers) is required to capture the onset of breaking, especially compared to the resolution that can be used outside the surf zone (1 – 3 layers). As an alternative, Smit et al. (2013) proposed

a breaking formulation, which parametrises the initiation of wave breaking, to capture the onset of wave breaking with a coarse vertical resolution.

In the last decade, a number of wave models have been developed based on the non-hydrostatic framework, albeit with different numerical techniques. This includes models that solve the equations on structured grids (e.g., Yamazaki et al., 2009; Zijlema et al., 2011; Ma et al., 2012), but also models that solve the equations on unstructured grids using the finite volume (e.g., Cui et al., 2012) or the finite element method (e.g., Wei and Jia, 2014). Furthermore, recent studies improved the efficiency of the framework by enhancing its dispersive properties (Bai and Cheung, 2013; Cui et al., 2014).

Since their introduction, non-hydrostatic wave models have become a popular alternative for the Boussinesq approach to simulate the evolution of waves over a variable bottom topography. The success of the non-hydrostatic framework is, amongst others, related to several of its key features (e.g., Smit, 2014). One of these features is the computational efficiency of this approach, which is comparable to Boussinesq-type models. Furthermore, the dispersive properties of non-hydrostatic models can be easily improved by using more vertical layers, which extends their applicability towards deeper water (or shorter waves). Thereby, it provides a flexible modelling framework to simulate a range of wave related processes.

So far, non-hydrostatic wave models have been successfully used to simulate a range of wave phenomena at various spatial and temporal scales. For example, they have been applied to simulate the propagation of tsunamis at oceanic scales (e.g., Walters, 2005; Yamazaki et al., 2011; Shimozono et al., 2014). At smaller scales, they have been used to simulate a range of wave processes in a coastal environment. This includes the evolution of waves over sloping bottoms (e.g., Zijlema and Stelling, 2008; Ai et al., 2011; Ma et al., 2012), the nonlinear wave dynamics in a surf zone (Smit et al., 2014), and the wave runup at a beach (Ruju et al., 2014).

2.2. WAVE-BODY INTERACTIONS

Most models that aim to resolve the interactions between waves and ships are based on the potential flow equations, which can be derived from the Euler equations assuming that the flow is irrotational (e.g., Mei et al., 2005). A further simplification is often made by linearising the boundary conditions at the free surface, which forms the basis of the linear potential theory. Using this theory, the first techniques to model the interactions between waves and floating bodies were developed in the 1950's (e.g., Beck and Reed, 2001). For example, Korvin-Kroukovsky and Jacobs (1957) initiated the development of a slender body theory known as the strip theory to simulate wave-ship interactions. In this approach, the ship is divided into a number of cross sections (or strips), which reduces the three-dimensional problem to a summation of two dimensional problems. This theory is only valid for linear waves with a length in the order of the ship's beam. Despite this limitation, strip theory is still used in the early design stage of ships to analyse their seakeeping properties even though far more advanced computational methods have been developed (Beck and Reed, 2001; Bertram, 2012).

Following these initial developments, more sophisticated three dimensional techniques were introduced in the following decades. Hess and Smith (1962) introduced the first three-dimensional technique based on the BEM to simulate incompressible poten-

tial flows without a free surface. In this approach, the flow problem is not solved in the interior of the flow, but it is mapped onto the boundaries of the fluid using Green's theorem. This requires a discretisation of the boundaries (such as the bottom, the free surface, and the hull of the ship) by a number of elements, or panels. The first applications of this method, also known as the panel method, to problems involving a free surface were based on linear potential theory, and used quadrilateral flat panels to discretise the boundaries. For a horizontal bottom of arbitrary depth, Green functions were derived that exactly satisfy the boundary condition at the bottom and the linearised boundary conditions at the free surface (e.g., Newman, 1985). This greatly simplifies the problem, because only the hull of the ship needs to be discretised.

When the primary wave field is well represented by linear potential theory (which is the case if the wave amplitudes are small), such panel methods can be successfully used to predict the linear wave-induced response of a floating body in deep water (e.g., Newman and Lee, 2002; Newman, 2005) and in relatively shallow water (e.g., Van Oortmerssen, 1976). However, in coastal regions nonlinear wave effects such as infragravity waves can cause a significant response of a moored ship. Formally, panel methods based on linear potential theory do not account for such higher-order effects, and one has to rely on methods that solve higher-order² or fully nonlinear potential theory. As an alternative to solve such higher-order theories, a number of approximate methods have been developed to estimate the second-order wave load based on the first-order solution (e.g., Newman, 1974; Molin, 1979; Pinkster, 1980). Such approximations can successfully predict the magnitude of the low-frequency second-order wave load (e.g., De Hautecloque et al., 2012; Pessoa and Fonseca, 2013; You and Faltinsen, 2015). However, for a complete description of the nonlinear response of a moored ship, panel models based on higher-order or fully nonlinear potential theory are required.

Following the development of models based on linear potential theory, various panel models based on higher-order or fully nonlinear panel theory have been developed to intrinsically account for nonlinear wave effects (e.g., Eatock Taylor and Chau, 1992; Liu et al., 2001; You and Faltinsen, 2015). The main difficulty in solving the higher-order or fully nonlinear problem is attributed to the nonlinearity of the boundary conditions at the free surface. To compute a higher-order or fully nonlinear solution, the free surface has to be discretised as well, because the Green function does not satisfy the nonlinear boundary conditions at the free surface.

In addition, a large number of panels are required to compute accurate higher-order solutions using the panel method, increasing the computational burden. This motivated the development of higher-order accurate panel methods, which require less panels to obtain accurate solutions compared to the original (lower-order) panel method, thereby improving the computational efficiency. In such methods, the panels and potential on the hull are represented by a continuous function, rather than the constant potential on a quadrilateral flat panel as used in the original panel method (e.g., Eatock Taylor

²In higher-order potential theory, the velocity potential ϕ is expanded using a perturbation expansion in the wave steepness $\epsilon (= a/L)$: $\phi = \epsilon\phi^{(1)} + \epsilon^2\phi^{(2)} + \dots$, where the superscript indicates the order of ϕ (e.g., Kevorkian and Cole, 1981). Substitution of the expanded velocity potential in the potential flow equations, and grouping the terms of equal order in ϵ , results in a set of equations for the first-order potential (equivalent to linear potential theory), and a set of equations for each higher-order potential (of which the solution depends upon the lower order solutions).

and Chau, 1992; Newman and Lee, 2002; Newman, 2005). However, higher-order and fully nonlinear solutions still require a discretisation of the free surface, resulting in a significant increase in the number of unknowns. The solution of the resulting system of unknowns, which yields a large and dense matrix, involves a significant computational effort compared to a panel method based on linear potential theory. Since their introduction, panel models have become a popular tool to simulate the interactions between waves and floating bodies in both offshore and coastal waters. For example, they have been used to study the hydrodynamics of side-by-side moored vessels (e.g., Huijsmans et al., 2001; Hong et al., 2005), higher-order wave effects on offshore structures (e.g., Zhou and Wu, 2014), and second-order wave effects on ships moored in shallow water (e.g., You and Faltinsen, 2015).

As an alternative to the panel method, the nonlinear potential flow problem has been solved by means of the FEM to study interactions between waves and structures (e.g., Ma et al., 2001a,b; Ma and Yan, 2009). In contrast to the BEM, the interior of the fluid domain is discretised in the FEM. Although this results in a larger number of unknowns, the resulting matrix is sparse and may require less storage space compared to the dense matrix that results from the BEM. For interactions between waves and moving bodies, Wu and Eatock Taylor (1995) found that the FEM can be computationally more efficient than the BEM when solving the fully nonlinear potential flow problem.

Although they differ in solution technique, all near field methods discussed so far were based on potential flow theory, limiting their applicability to conditions in which turbulent effects are negligible. However, in the case of large wave impacts or significant ship motions, the assumptions of potential theory are violated and alternative methods are required to simulate the wave-ship interactions. As discussed previously in §2.1, RANS and SPH type models can capture the turbulent effects which are important in such conditions. These models are not only suited to resolve the evolution of waves over sloping bottoms, but can also be used to simulate the interactions between waves and (floating) structures. For example, these methods have been used to simulate the green water on a deck (e.g., Kleefsman et al., 2005; Gómez-Gesteira et al., 2005), to study the interactions between waves and floating bodies (e.g., Hadžić et al., 2005; Bouscasse et al., 2013), and to simulate the seakeeping of ships (e.g., Wilson et al., 2006; Stern et al., 2013). Given their great detail and complexity, the RANS and SPH approach are computationally more expensive compared to the potential flow models. This makes them particularly suited for conditions in which turbulent effects are important, such as large wave impacts on structures (e.g., Veldman et al., 2011) and the (self-propelled) seakeeping of ships (e.g., Carrica et al., 2006; Mofidi and Carrica, 2014).

2.3. MOORED SHIPS IN COASTAL WATERS

To predict the wave-induced response of a ship that is moored in coastal waters based on an offshore wave climate, a numerical model should account for the wave evolution in a coastal or harbour region, and for the interactions between the waves and the moored ship. Compared to the vast body of literature that focusses on either the far field problem (§2.1) or the near field problem (§2.2), less research has focussed on the combined problem.

Ohyama and Tsuchida (1997) presented one of the first approaches to simulate the wave-induced motions of a ship that is moored inside a harbour region based on off-shore wave conditions. They derived an extension to the original MSE, to account for the interactions between the waves and a moored ship. As this method is based on the MSE, it only captures the evolution of the linear wave field and their interactions with a moored ship, and does not account for nonlinear wave effects. This approach is thus only suited to predict the linear response of a moored ship when nonlinear wave effects are negligible. However, in coastal environments this is typically not the case as, for example, the presence of infragravity waves may lead to a disruption of harbour operations.

Van der Molen et al. (2006) coupled a wave model with a near field model to simulate the response of a moored ship to the infragravity wave field. The wave field at the berth (undisturbed by the presence of the moored ship) was predicted using a wave model that combines a stochastic approach to solve the wave groups and a deterministic approach to solve the infragravity wave field (previously discussed in §2.1). The wave-induced response of the moored ship was subsequently computed assuming that the waves are long (which is a valid assumption for the infragravity waves). Consequently, this approach is restricted to conditions in which the response of a moored ship is dominated by infragravity waves.

To simulate the response of a moored ship to the combined short and infragravity wave field, several authors combined a deterministic model based on the Boussinesq or non-hydrostatic approach with a panel method (Bingham, 2000; Van der Molen and Wenneker, 2008; Dobrochinski, 2014). In this approach, the undisturbed wave field at a berth is predicted using a wave model that accounts for the nonlinear evolution of waves over a variable bottom topography. Based on this wave field, the interactions between the waves and the ship were computed using a lower-order panel method based on linear potential theory. This coupled model can simulate the nonlinear response of a moored ship in coastal waters if the wave nonlinearity is small ($ak/\tanh(kh) \ll 1$, which reduces to $ak \ll 1$ in deep water and $a/h \ll 1$ in the shallow water limit) in the vicinity of the ship (Bingham, 2000).

For wave conditions that do not satisfy this constraint, more accurate but computationally intensive methods are likely necessary to capture the nonlinear wave-ship interactions (e.g., a nonlinear potential flow model or a RANS model). In principal, such methods can be used in conjunction with a wave model, but, to the author's knowledge, such efforts to simulate wave-ship interactions have not been reported yet. At present, predictions of the wave-induced response of moored ship in coastal waters are thus restricted to weakly nonlinear wave conditions. This limits such predictions to relatively calm wave conditions, for example, when a ship is moored in a harbour basin.

This thesis aims to develop an alternative approach to simulate the nonlinear evolution of waves and their impact on a moored ship in a realistic coastal or harbour region. Here, the development of a single numerical model is pursued, rather than a coupled approach, to solve the combined far and near field problem. This development is based on the non-hydrostatic approach, and the SWASH model in particular (Zijlema et al., 2011).

The non-hydrostatic approach is essentially a numerical implementation of the RANS equations, and provides a flexible modelling framework to simulate a range of wave re-

lated processes. As it is based on the basic equations that govern the hydrodynamics of an incompressible fluid, there are no inherent limitations to apply this method for flows that are bounded by the hull of a ship. As such, the non-hydrostatic approach can be naturally extended to account for the interactions between the waves and a moored ship. Conceptually, the resulting model captures the fully nonlinear wave-ship interactions, as it makes no a-priori assumptions on the characteristics of the wave and flow field. However, it is unclear if this approach can accurately capture these interactions at acceptable computational costs, which would allow for applications at the scales of a realistic coastal or harbour region.

In the context of simulating the wave-induced response of a moored ship, this thesis pursues a further development and verification of the SWASH model to simulate the nearshore evolution of waves and their interactions with a restrained ship. First, this work studies whether the model can simulate the evolution of waves – and infragravity waves in particular – at the scale of a realistic coastal region (Chapter 3 and 4). Next, the model is further developed to resolve the interactions between the waves and a fixed floating body (Chapter 5). With these efforts, this thesis explores the potential of the non-hydrostatic approach to resolve the evolution of waves and their impact on a moored ship at the scale of a realistic coastal or harbour region.

3

NON-HYDROSTATIC MODELLING OF INFRAGRAVITY WAVES UNDER LABORATORY CONDITIONS*

ABSTRACT

The non-hydrostatic wave model SWASH is compared to flume observations of infragravity waves propagating over a plane slope and barred beach. The experiments cover a range of infragravity wave conditions, including forcing by bichromatic and irregular waves, varying from strongly dissipative to strongly reflective, so that model performance can be assessed for a wide range of conditions. The predicted bulk wave parameters, such as wave height and mean wave period, are found to be in good agreement with the observations. Moreover, the model captures the observed breaking of infragravity waves. These results demonstrate that SWASH can be used to model the nearshore evolution of infragravity waves, including nonlinear interactions, dissipation and shoreline reflections.

3.1. INTRODUCTION

As short-wave groups propagate towards the shore they force longer waves with periods ranging from 20s to 250s. Such low-frequency motions are commonly referred to as infragravity waves. Infragravity waves are found to be significant for harbour resonance (e.g., Bowers, 1977), moored vessel motions (e.g., Naciri et al., 2004), collapse of ice shelves (Bromirski et al., 2010) and dune erosion (e.g., Van Thiel de Vries et al., 2008), which makes them an important subject for coastal and harbour engineers.

Two main mechanisms for the generation of infragravity waves have been identified. Longuet-Higgins and Stewart (1962, 1964) proposed that groups of short waves

*This chapter has been published as Rijnsdorp, D. P., Smit, P. B., and Zijlema, M. (2014): Non-hydrostatic modelling of infragravity waves under laboratory conditions. *Coastal Engineering* 85, 30–42

force infragravity waves through spatial gradients in the radiation stress. These infragravity waves propagate with the velocity of the short-wave envelope and are known as bound infragravity waves. Furthermore, Symonds et al. (1982) showed that the time variation of the breakpoint, induced by short-wave groups, generates a shoreward and seaward directed free infragravity wave which propagate with the free wave celerity. The cross-shore propagation of infragravity waves over an uneven bottom has been studied extensively by means of field experiments, laboratory experiments and numerical models. Such studies revealed that, as waves approach the shore, bound infragravity waves grow with a rate greater than for energy conservative shoaling, due to weakly nonlinear interactions between short waves and bound infragravity waves (e.g., List, 1992; Masselink, 1995; Janssen et al., 2003; Battjes et al., 2004). In the nearshore, because infragravity waves are generally much longer than the short waves which generate them, infragravity waves can lose energy due to bottom friction (Henderson and Bowen, 2002). This is particularly important in case of an extensive flat and shallow region, such as a coral reef (Pomeroy et al., 2012), but less significant on sloping beaches (e.g., Henderson et al., 2006; Van Dongeren et al., 2007). Once infragravity waves enter the surf zone, the wave motion becomes strongly nonlinear, energy is exchanged rapidly between the short waves and the infragravity waves (Henderson et al., 2006; Thomson et al., 2006) and strong dissipation can occur due to infragravity wave breaking (Van Dongeren et al., 2007). Ruju et al. (2012) suggested that, based on a numerical study, nonlinear interactions are strongest in the outer surf zone, whereas – if it occurs – infragravity wave breaking appears to be the dominant process in the inner surf zone. For weakly dissipative conditions, infragravity waves (partially) reflect at the beach and subsequently propagate in seaward direction. Because the short-wave motion is mostly destroyed in the surf zone, such seaward directed waves are free waves, which may either propagate towards deeper water, known as leaky waves, or become trapped in the coastal region by refraction, known as edge waves. The simultaneous presence of incoming, and outgoing infragravity waves can result in a (partially) standing infragravity wave pattern near the surf zone.

The large difference in scales and the various physical phenomena (e.g., friction, wave-breaking) involved in the evolution of infragravity waves places stringent demands on numerical models. In the surf-zone, a full representation of the infragravity wave dynamics not only involves resolving the wave groups, but also the individual waves, including small scale processes due to wave breaking. Resolving all relevant scales over relatively short temporal and spatial scales is now within reach of RANS type models (e.g., Lin and Liu, 1998), as is exemplified by the successful application of such a model to simulate low-frequency motions under laboratory conditions (e.g., Torres-Freyermuth et al., 2010; Lara et al., 2011). However, models applicable for larger scale engineering and scientific applications often do not explicitly resolve the short waves. Instead, a so called phase-averaged approach is often used, in which a model that accounts for the nearshore transformation of short waves, providing the forcing on the wave group scale, is combined with a model based on the shallow-water equations, which accounts for the nearshore transformation of infragravity waves (e.g., Roelvink et al., 2009). These models have been applied to simulate infragravity waves under field conditions and obtained reasonable agreement between model results and field data (e.g., List, 1992; Van Don-

geren et al., 2003; Reniers et al., 2002, 2006, 2010; Van Dongeren et al., 2013). However, because they invariably use linear theory for the evolution of the short waves, they are less accurate under strongly nonlinear conditions. Moreover, they usually only include a one way coupling, in which wave energy can be transferred from the short waves to the infragravity waves, but not vice-versa.

Models based on a Boussinesq type formulation (e.g., Madsen et al., 1991; Nwogu, 1993; Wei et al., 1995) or based on the non-hydrostatic approach (e.g., Stelling and Zijlema, 2003; Ma et al., 2012) are an alternative to the RANS and phase-averaged approach. These models aspire to resolve both the individual waves, including all the relevant processes (e.g., shoaling, refraction, diffraction, and nonlinearity) and the bulk dissipation associated with wave breaking, but not the detailed breaking process itself (e.g., wave overturning). Compared to RANS models this allows them to efficiently compute free surface flows by considering the free surface as a single-valued function. Boussinesq type models, introduced for variable depths by Peregrine (1967), have been applied extensively to the cross-shore evolution of short-wave motions, including wave breaking (e.g. Schäffer et al., 1993; Kennedy et al., 2000; Cienfuegos et al., 2010; Tonelli and Petti, 2012; Tissier et al., 2012) and to a lesser extent to ig-motions (e.g Madsen and Sørensen, 1993; Madsen et al., 1997). Non-hydrostatic models were introduced more recently and have shown great potential for resolving the short-wave dynamics, including wave breaking (e.g., Zijlema and Stelling, 2008; Ma et al., 2012; Smit et al., 2013) and the nonlinear wave-dynamics in a surf zone (Smit et al., 2014). Similar to RANS models, non-hydrostatic models are essentially implementations of the basic conservation equations for mass and momentum, that by using a reduced vertical resolution (two to three layers) have a similar computational effort and accuracy compared with Boussinesq models, whereas their implementation is less complex thereby improving robustness and maintenance. However, thus far, at coarse vertical resolutions non-hydrostatic models have not been verified for infragravity waves.

In this study we show the capabilities of SWASH (Zijlema et al., 2011), a non hydrostatic type model, in reproducing the nearshore transformation of infragravity waves. To include the generation of incident bound infragravity waves, a wave-generating boundary condition – based on second order wave theory – has been implemented. Model results are compared with measurements of the flume experiment of Van Noorloos (2003) and Boers (1996).

The outline of this paper is as follows: §3.2 gives an overview of the governing equations of SWASH, including relevant details of its numerical implementation. In §3.3 we present the second-order boundary condition. The model validation for the Van Noorloos (2003) and Boers (1996) experiment is presented in §3.4 and §3.5, respectively. To conclude the paper, we discuss and summarise our main findings in §3.6 and §3.7.

3.2. NUMERICAL MODEL

GOVERNING EQUATIONS¹

The non-hydrostatic model SWASH (Zijlema et al., 2011) is a numerical implementation of the RANS equations for an incompressible fluid with a constant density and a free

¹Parts of this section closely follow the description of SWASH in Smit et al. (2013).

surface. In a two-dimensional framework that is bounded by the free surface $z = \zeta(x, t)$ and the bottom $z = -d(x)$, where t is time and x and z are Cartesian co-ordinates ($z = 0$ is located at the still water level), the governing equations read

$$\frac{\partial u}{\partial t} + \frac{\partial uu}{\partial x} + \frac{\partial wu}{\partial z} = -\frac{1}{\rho} \frac{\partial (p_h + p_{nh})}{\partial x} + \frac{\partial}{\partial x} \left(v^h \frac{\partial u}{\partial x} \right) + \frac{\partial}{\partial z} \left(v^v \frac{\partial u}{\partial z} \right), \quad (3.1)$$

$$\frac{\partial w}{\partial t} + \frac{\partial uw}{\partial x} + \frac{\partial ww}{\partial z} = -\frac{1}{\rho} \frac{\partial (p_h + p_{nh})}{\partial z} + \frac{\partial}{\partial x} \left(v^h \frac{\partial w}{\partial x} \right) + \frac{\partial}{\partial z} \left(v^v \frac{\partial w}{\partial z} \right) - g, \quad (3.2)$$

$$\frac{\partial u}{\partial x} + \frac{\partial w}{\partial z} = 0, \quad (3.3)$$

where $u(x, z, t)$ is the horizontal velocity, $w(x, z, t)$ is the vertical velocity, v^h and v^v are the horizontal and vertical kinematic eddy viscosity, respectively, g is the gravitational acceleration, and p_h and p_{nh} are the hydrostatic and non-hydrostatic pressure, respectively. The hydrostatic pressure is expressed in terms of the free surface as $p_h = \rho g (\zeta - z)$ such that $\partial_z p_h = -\rho g$ (where ∂_z is short for $\partial/\partial z$) and $\partial_x p_h = \rho g \partial_x \zeta$. An expression for the free surface is obtained by considering the (global) mass balance for the entire water column

$$\frac{\partial \zeta}{\partial t} + \frac{\partial}{\partial x} \int_{-d}^{\zeta} u dz = 0. \quad (3.4)$$

For waves propagating over intermediate distances (say $O(10)$ wave lengths), in the absence of strongly sheared currents, turbulence has only marginal effects on the wave motion and can – to a good approximation – be neglected. Furthermore, the above equations (excluding the turbulence terms) can be directly applied to estimate the overall characteristics of a quasi-steady breaking bore in the surf zone, without the need to resolve complex phenomena such as the wave generated turbulence. Therefore, turbulent stresses can be neglected in this study. However, to increase numerical stability and to allow the influence of bottom friction to extend over the vertical, we introduce some vertical mixing by means of the vertical exchange of momentum due to turbulent stresses with a constant $v^v (= 10^{-4} m^2/s)$.

Kinematic and dynamic boundary conditions are prescribed at the free surface and bottom, given by

$$\begin{aligned} w(x, z = \zeta, t) &= \frac{\partial \zeta}{\partial t} + u \frac{\partial \zeta}{\partial x}, \\ w(x, z = -d, t) &= -u \frac{\partial d}{\partial x}. \end{aligned} \quad (3.5)$$

These boundary conditions ensure that no particle leaves the surface and no particle penetrates the fixed bottom. At the free surface the dynamic boundary condition prescribes a constant pressure ($p_{nh} = p_h = 0$) and no surface stresses. At the bottom boundary a bottom stress term is added to the horizontal momentum equation (3.1) as bottom friction is important for the low-frequency motions, for which it is one of the mechanisms of energy dissipation. The bottom stress is based on a quadratic friction law $\tau_b = c_f \frac{U|U|}{h}$, where $h = d + \zeta$ is the total water depth, c_f is a dimensionless friction coefficient and U is the depth-averaged velocity. Feddersen et al. (2003) found that the friction

coefficient is enhanced in the surf zone due to the presence of breaking waves. In this study we compute the friction coefficient based on the Manning-Strickler formulation, which reads $c_f = 0.015 (d_r/h)^{1/3}$ where d_r is an (apparent) roughness value. Although this formulation was derived for slowly varying open-channel flows and not for rapidly varying flows such as in the surf zone, it gives increasing values of c_f for decreasing depths which makes it a suitable proxy to mimic the wave breaking enhanced roughness. The disadvantage of this formulation is that the roughness value cannot easily be estimated a priori and instead – as will be done in this study – needs to be calibrated.

Waves are generated at the wavemaker boundary (situated at $x = 0\text{m}$) by prescribing the horizontal velocity $u(x = 0, z, t)$ obtained from second-order wave theory, which will be described in detail in §3.3. At the shore we employ a moving shoreline boundary condition to accurately simulate wave run-up and flooding and drying (Stelling and Duijnmeijer, 2003).

NUMERICAL IMPLEMENTATION

The numerical implementation is based on an explicit, second-order accurate (in space and time) finite difference method that conserves both global mass and momentum at the numerical level. Local mass conservation, corresponding to a divergence-free velocity field, is obtained by means of a pressure correction technique. A structured grid is employed to discretise the physical domain. In x -direction the grid has a constant width whereas in vertical direction the physical domain is divided into a fixed number of layers (K) between the bottom and the free surface, which results in a (spatially varying) layer thickness of $\Delta z = h/K$. A more detailed overview of the numerical implementation is given in Zijlema et al. (2011) and references therein. With the numerical implementation used in the SWASH model, good wave dispersive properties are found even for low vertical resolutions (Zijlema et al., 2011; Smit et al., 2014). For instance, with two vertical layers (as used in this study) the relative error in the phase velocity (compared with the linear dispersion relation) is approximately 1% up to $kd \approx 8$, where k is the wave number. This allows SWASH to account for the relevant physics outside the surf zone (refraction, shoaling, diffraction, non-linear interactions) with a relative coarse vertical resolution.

In the surf zone, SWASH intrinsically accounts for the energy dissipation of a breaking wave. Once the wave height over depth ratio becomes $\mathcal{O}(1)$, a discontinuity develops as a wave steepens up and develops a vertical face. In such a situation, as the model conserves momentum over the discontinuity using shock-capturing dynamics, energy is dissipated at a rate analogous with that of a bore (Lamb, 1932). However, compared with the resolution outside the surf zone, this requires a high vertical resolution ($\mathcal{O}(10)$ vertical layers) to reproduce the observed locations of incipient wave breaking, whereas at low vertical resolutions wave breaking is delayed (Smit et al., 2013). At present, such high vertical resolutions are not feasible for relatively large horizontal domains (e.g., 10×10 wavelengths). To capture wave breaking with only a few vertical layers, Smit et al. (2013) proposed an approach with which the non-hydrostatic pressure is neglected in the vicinity of a breaking wave. This (locally) reduces the governing equations to the nonlinear shallow water equations and ensures that a wave develops a vertical face. This approach is initiated once the rate of change of the free surface exceeds a certain threshold ($\partial_t \zeta / \sqrt{g\bar{h}} > \alpha$, where α is the threshold). Once initiated, α is reduced to β (with

$\beta < \alpha$) in neighbouring points to allow breaker persistence. In this study we use the values for α ($= 0.6$) and β ($= 0.3$) found by Smit et al. (2013) for two vertical layers, for which good results were obtained for various flume and basin experiments.

3.3. A SECOND-ORDER BOUNDARY CONDITION TO GENERATE INCIDENT BOUND INFRAGRAVITY WAVES

At the model wavemaker the normal horizontal velocity based on second-order wave theory is prescribed to generate incident waves. In this study we only incorporate the difference interactions (i.e. bound infragravity waves) and we exclude the sum interactions (i.e. bound super harmonics) for efficiency reasons.² The incident (target) horizontal velocity u_t at the boundary is given by

$$u_t(x=0, z, t) = \sum_{n=1}^N \hat{u}_n(z) \cos(2\pi f_n t + \phi_n) + \sum_{n=1}^N \sum_{m=n+1}^N \hat{u}_{nm} \cos(2\pi f_{nm} t + \phi_{nm}), \quad (3.6)$$

where N is the number of free wave components. The first term on the right-hand-side of (3.6) represents the linear free wave contribution, where f_n is the frequency, ϕ_n is the phase and $\hat{u}_n(z)$ is the vertically varying velocity amplitude of the n th wave component which is related to the short-wave amplitude a_n by linear wave theory (e.g., Holthuijsen, 2007). The second summation is the second-order correction which represents the contribution of the incident bound infragravity waves, where $f_{nm} (= f_m - f_n)$ is the frequency, $\phi_{nm} = (\phi_n - \phi_m + \pi)$ is the phase and \hat{u}_{nm} is the vertically varying velocity amplitude of the bound infragravity wave component forced by the difference interaction between the n th and m th free wave component. In coastal waters, infragravity waves are essentially shallow-water waves for which the vertical variation of \hat{u}_{nm} is negligible. Therefore, we approximate \hat{u}_{nm} with a vertically constant velocity amplitude, which is computed based on the free wave components following Hasselmann (1962), see Appendix 3.A.

To prevent re-reflections at the wavemaker a weakly reflective boundary condition is adopted in which the total velocity signal $u(x=0, z, t)$ is a superposition of incident, or target, velocity signal (u_t) and a velocity signal of the reflected waves (u_r), i.e. $u = u_t + u_r$. To estimate the velocity of the reflected wave signal we assume that the reflected waves are shallow water waves, which implies that all short waves have dissipated inside the domain. This allows us to compute the depth averaged horizontal velocity u_r based on the surface elevation of the outgoing waves, which is detected as the difference between the target surface elevation ζ_t and the instantaneous surface elevation ζ computed by SWASH. The u_r follows from mass conservation in combination with the assumption

²The exclusion of the sum interactions at the model boundary does not imply that the bound super harmonics are absent, instead, in addition to the bound higher harmonics, spurious free waves are generated at the sum frequencies (see also Appendix 3.B). Because the energy contained in such spurious modes is comparable to the bound energy (which is small compared with the energy in the primary waves), the influence of the additional spurious energy is small, and will not adversely affect the nearshore transformation of the high frequency band.

that outgoing waves are progressive and of constant form,

$$u_r = \frac{c}{d} (\zeta - \zeta_t), \tag{3.7}$$

where c is the phase velocity, which is taken as the shallow water phase velocity $c = \sqrt{gd}$.

We have verified the accuracy of the second-order weakly-reflective boundary condition in reproducing the classical finite depth solution of Longuet-Higgins and Stewart (1960) for bound infragravity waves, induced by a bichromatic wave group which propagates over a flat bottom. With two or more vertical layers the solution of Longuet-Higgins and Stewart (1960) is reproduced well if the short waves that form the wave group are in shallow to intermediate water depths ($kd < 2.5$) (Appendix 3.B).

3.4. INFRAGRAVITY WAVES INDUCED BY BICHROMATIC WAVES OVER A PLANE SLOPE

Van Noorloos (2003) considered the evolution of bichromatic wave groups as they propagate in a 40m long flume over a 1/35 plane slope (see Fig. 3.1). An interesting feature of these experiments is that they confirmed that dissipation due to infragravity wave breaking can be one of the primary mechanisms of infragravity wave dissipation (Van Dongeren et al., 2007). In these experiments the flume was equipped with a piston-type wave board, which included second-order wave control and reflection compensation. Van Noorloos (2003) considered eight bichromatic wave conditions which varied in wave magnitude (B1-4, see Table 3.1) and in bound infragravity wave frequency (f_b) (A1-4, see Table 3.1), where the latter in particular is associated with varying infragravity wave conditions. In these experiments infragravity wave conditions ranged between strong infragravity wave dissipation (due to infragravity wave breaking) and small infragravity wave reflections near the shoreline (experiment A1) to strong infragravity wave reflections (experiment A4) (Van Dongeren et al., 2007). Measurements of the free surface were taken at 80 locations, with a spacing varying from 0.5m to 0.3m, for a duration of 10 minutes.

SWASH is employed with two vertical layers to accurately capture the wave dispersion, and the bound infragravity wave response (Appendix 3.B), for the range of kd values encountered (see Table 3.1). The grid resolution is set at $\Delta x = 0.01m$, which corre-

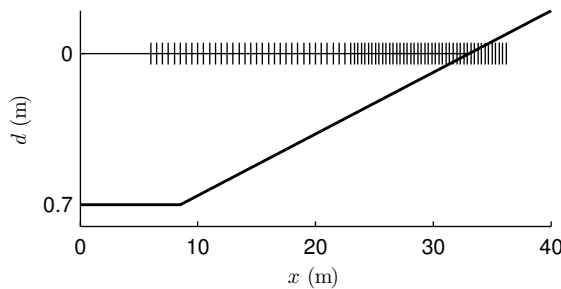


Figure 3.1: Van Noorloos (2003) experimental set-up. The still water level is located at $z = 0m$ and the vertical lines indicate the gauge locations.

Table 3.1: Wave parameters at the boundary for the bichromatic wave experiments. Listed are the primary wave frequencies f and amplitudes a ; bound wave frequency f_b and the maximum normalised water depth kd .

	f_1 (Hz)	f_2 (Hz)	f_b (Hz)	a_1 (m)	a_2 (m)	kd
A1	0.67	0.48	0.19	0.06	0.012	2.00
A2	0.65	0.50	0.15	0.06	0.012	1.94
A3	0.64	0.51	0.13	0.06	0.012	1.90
A4	0.62	0.53	0.09	0.06	0.012	1.81
B1	0.65	0.50	0.15	0.06	0.018	1.95
B2	0.65	0.50	0.15	0.06	0.024	1.95
B3	0.65	0.50	0.15	0.06	0.030	1.95
B4	0.65	0.50	0.15	0.06	0.036	1.95

sponds to at least 20 points per wave length for the super harmonic wave components, and the time step is set at $\Delta t = 0.002s$. The incoming boundary is located at the first wave gauge ($x = 6m$) and we employ a second-order accurate weakly-reflective boundary to generate incident waves (§3.3), according to the target wave conditions (Table 3.1). The roughness coefficient $d_r (= 0.0075m)$ was calibrated for the experiment which featured the strongest infragravity wave reflections (A4), where we expect a significant influence of the bottom friction on the infragravity wave dynamics. In the following, the analysis is based on the measured and computed free surface elevation records after steady state conditions were observed, five minutes after the start of the simulation (Van Dongeren et al., 2007).

RESULTS

First we compare the predicted and measured cross-shore transformation of the bulk wave parameters for experiment A1, A4, B1 and B4. Here, we compare measured and predicted root-mean-square wave heights H_{rms} , which are computed from the variance of linearly detrended surface elevation signals, $H_{rms} = \sqrt{8\langle\zeta^2\rangle}$, where $\langle\dots\rangle$ indicates time averaging. To analyse the nearshore transformation of infragravity waves, the surface elevation signals have to be filtered. The occurrence of infragravity wave breaking in some of the experiments indicates that strong nonlinear effects play a dominant role in the evolution of the infragravity waves close to the shoreline. Near the shore not only the high-frequency waves, but also the infragravity waves transition into sawtooth like-shapes, which in the spectral domain is associated with the generation of significant energy at the higher harmonics of the infragravity wave frequencies. For this reason, we filter the surface elevation signal using a band pass filter that includes the difference frequency ($\Delta f = f_1 - f_2$) and integer multiples thereof ($m\Delta f$ for $m = 2\dots f_{nyq}/\Delta f$, where f_{nyq} is the Nyquist frequency). This method is applicable as the variance at the $m\Delta f$ frequencies is attributed to infragravity wave self-self interactions and not to (interactions of) higher-frequency components (Van Dongeren et al., 2007). In the remaining of this section we use a tilde accent ($\tilde{}$) to denote variables computed from the filtered signal.

The variation of the measured wave height H_{rms} is similar in experiment A1, A4, B1 and B4 (see Fig. 3.2a-b and Fig. 3.3a-b). In all four cases H_{rms} remains nearly constant

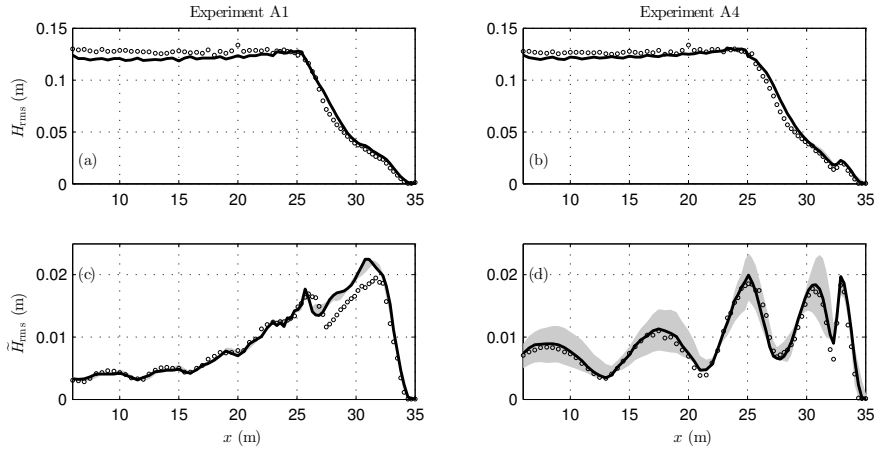


Figure 3.2: Cross-shore variation of the H_{rms} (upper panels) and the \tilde{H}_{rms} (lower panels) for experiment A1 (left panels) and A4 (right panels). Comparison between measured (circles) and computed values (lines). The grey region gives the range in wave heights found when varying the roughness coefficient.

on the flat ($x < 8.5\text{m}$) and at the start of the slope, and reduces rapidly in the surf zone once breaking is initiated ($x \approx 25\text{m}$). For all cases predicted and measured H_{rms} are in agreement, except for B4 where the predicted position of incipient short-wave breaking is located further shoreward than the observed location (Fig. 3.3b). For B4, the predicted location of wave breaking can be improved with a slightly smaller breaking threshold ($\alpha=0.5$), see Fig. 3.3b.

The aforementioned difference in infragravity wave behaviour for the different incident wave conditions, i.e. reflective or dissipative, can be seen by comparing the cross-shore variation of the measured infragravity wave height \tilde{H}_{rms} for experiment A1 and A4 (see Fig. 3.2c-d). In A1, \tilde{H}_{rms} increases in shoreward direction with a small oscillation for $x < 25\text{m}$. As the short waves start to break ($x \approx 25\text{m}$) \tilde{H}_{rms} decreases, up to $x \approx 27\text{m}$ where it increases again. For $x > 31\text{m}$, \tilde{H}_{rms} decreases significantly. In experiment A4 the cross-shore variation of \tilde{H}_{rms} has a nodal structure with an increasing magnitude towards the shore. The nodal structure is associated with the occurrence of a standing infragravity wave. For experiment B1 and B4 the nearshore transformation of the \tilde{H}_{rms} is similar to A1 (see Fig. 3.3c-d). For all cases predicted and measured \tilde{H}_{rms} are in agreement, except for a discrepancy for $26\text{m} < x < 32\text{m}$ in A1 and B1, where \tilde{H}_{rms} is over estimated due to an over prediction of the incoming infragravity wave height, and in B1 and (especially) B4, where the predicted oscillation of \tilde{H}_{rms} for $x < 25\text{m}$ is more pronounced than in the measurements due to an over prediction of the outgoing infragravity wave height.

Incoming infragravity waves are generally bound to the wave group, such that their behaviour no longer corresponds to that of a free wave. In contrast reflected infragravity waves are free waves as the high-frequency motion is almost entirely destroyed in the surf zone. The different character of the incoming and outgoing low-frequency motion makes it interesting to consider them separately. To distinguish between these two components, we decompose the infragravity wave signal with the decomposition method of

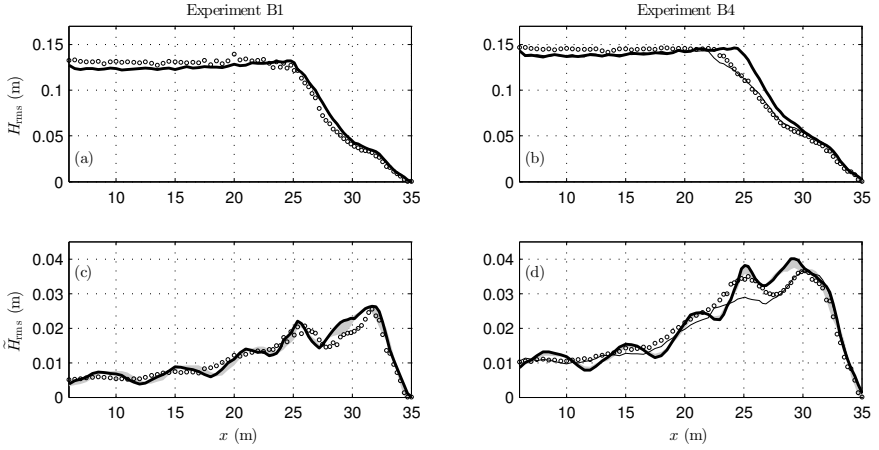


Figure 3.3: Cross-shore variation of the H_{rms} (upper panels) and the \tilde{H}_{rms} (lower panels) for experiment B1 (left panels) and B4 (right panels). Comparison between measured (circles) and computed values (lines). The grey region gives the range in wave heights found when varying the roughness coefficient. The thin black line in panel b and d is calculated with $\alpha = 0.5$.

Battjes et al. (2004), as used by Van Dongeren et al. (2007). In A1, B1 and B4 measured outgoing infragravity wave heights \tilde{H}_{rms}^- are small compared to measured incoming infragravity wave heights \tilde{H}_{rms}^+ (Fig. 3.4a,c-d), which indicates that the shoreline reflection and the contribution of breakpoint induced infragravity waves is small. In the measurements, incoming infragravity waves grow towards the shore with a growth rate which exceeds Green's law for energy conservative shoaling ($H \propto d^{-1/4}$). For $x > 25\text{m}$ measured \tilde{H}_{rms}^+ decreases, up to $x \approx 27\text{m}$ where it increases again. Close to the shore \tilde{H}_{rms}^+ starts to decrease significantly, which is associated with infragravity wave breaking (Van Dongeren et al., 2007). The cross-shore variation of \tilde{H}_{rms}^+ and \tilde{H}_{rms} are very similar which further illustrates the dominance of incoming infragravity waves. For A4 the growth of \tilde{H}_{rms}^+ is small compared to the other three experiments, whereas the magnitude of \tilde{H}_{rms}^- is larger (Fig. 3.4b). Predicted and measured incoming and outgoing wave heights are in agreement throughout the domain for all experiments, apart from an over prediction of \tilde{H}_{rms}^+ inside the surf zone ($x > 26\text{m}$) in A1 and B1, a local over prediction of \tilde{H}_{rms}^- at $x \approx 26\text{m}$ in A4, and a significant over prediction of \tilde{H}_{rms}^- throughout the domain in B1 and B4. Discrepancies between predicted and measured infragravity wave heights are most significant for experiment B4, for which we previously observed that short-wave breaking is delayed in SWASH (Fig. 3.3b). Not only does reducing the breaking threshold ($\alpha = 0.5$) improves predicted H_{rms} (Fig. 3.3b), it also improves predictions of \tilde{H}_{rms} , \tilde{H}_{rms}^+ and \tilde{H}_{rms}^- (Fig. 3.3d and 3.4d), which indicates that the over prediction of \tilde{H}_{rms}^- is related to the delayed short-wave breaking.

To investigate the influence of the roughness coefficient on the model results, additional simulations were executed with a roughness coefficient ranging $d_r = 0.001 - 0.02\text{m}$. The shaded regions in Fig. 3.2-3.4 are the regions between the maximum and minimum of H_{rms} , \tilde{H}_{rms} and $\tilde{H}_{\text{rms}}^\pm$ for the simulations with the various roughness co-

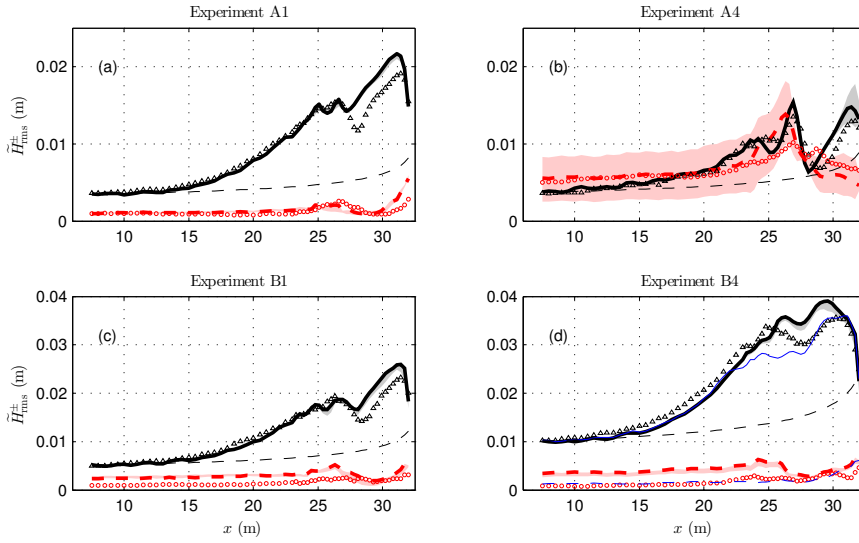


Figure 3.4: Cross-shore variation of incoming \tilde{H}_{rms}^+ and outgoing infragravity wave heights \tilde{H}_{rms}^- for experiment A1 (panel a), A4 (panel b), B1 (panel c) and B4 (panel d). Comparison between measured (incoming component: black triangles, outgoing component: red circles) and predicted values (incoming component: solid black line, outgoing component: dashed red line). The black dashed curve indicates Green's law for energy conservative shoaling ($H \propto d^{-1/4}$), initiated with the predicted incident incoming infragravity wave height. The shaded regions give the range in wave heights found when varying the roughness coefficient (incoming component: grey, outgoing component: light red). The thin blue lines panel d are calculated with $\alpha = 0.5$.

efficient. The low sensitivity of H_{rms} to variations in d_r implies that bottom friction – as anticipated – has only a marginal influence on the nearshore transformation of short waves (Fig. 3.2-3.3). Similarly, if infragravity waves are breaking, infragravity wave energy losses are dominated by infragravity wave breaking and the influence of variations in d_r is small (Fig. 3.4a,c-d). Only for a strong reflective condition (A4), variations in d_r significantly influence infragravity wave heights. Nevertheless, the nodal pattern is correctly reproduced for all values of d_r (Fig. 3.2d). In all experiments, but most significantly for A4, bottom friction predominantly influences outgoing infragravity wave heights (Fig. 3.4b), which indicates that friction is primarily of significance in the inner surf zone ($x > 30\text{m}$).

Infragravity wave breaking can be observed when inspecting the time signals of the infragravity wave surface elevation at several gauge locations near the shoreline, which is similar to an analysis in Van Dongeren et al. (2007). In experiment A1, as the infragravity waves enter progressively shallower water, the infragravity wave front develops an almost vertical face and subsequently rapidly decays in height (Fig. 3.5). This pattern is very similar to that of a breaking wave and suggests that infragravity waves are breaking. A similar analysis for experiment A4 shows no sign of infragravity wave breaking in both measured and computed surface elevation signals (Fig. 3.5). For both cases, computed wave signals are in agreement with the observations.

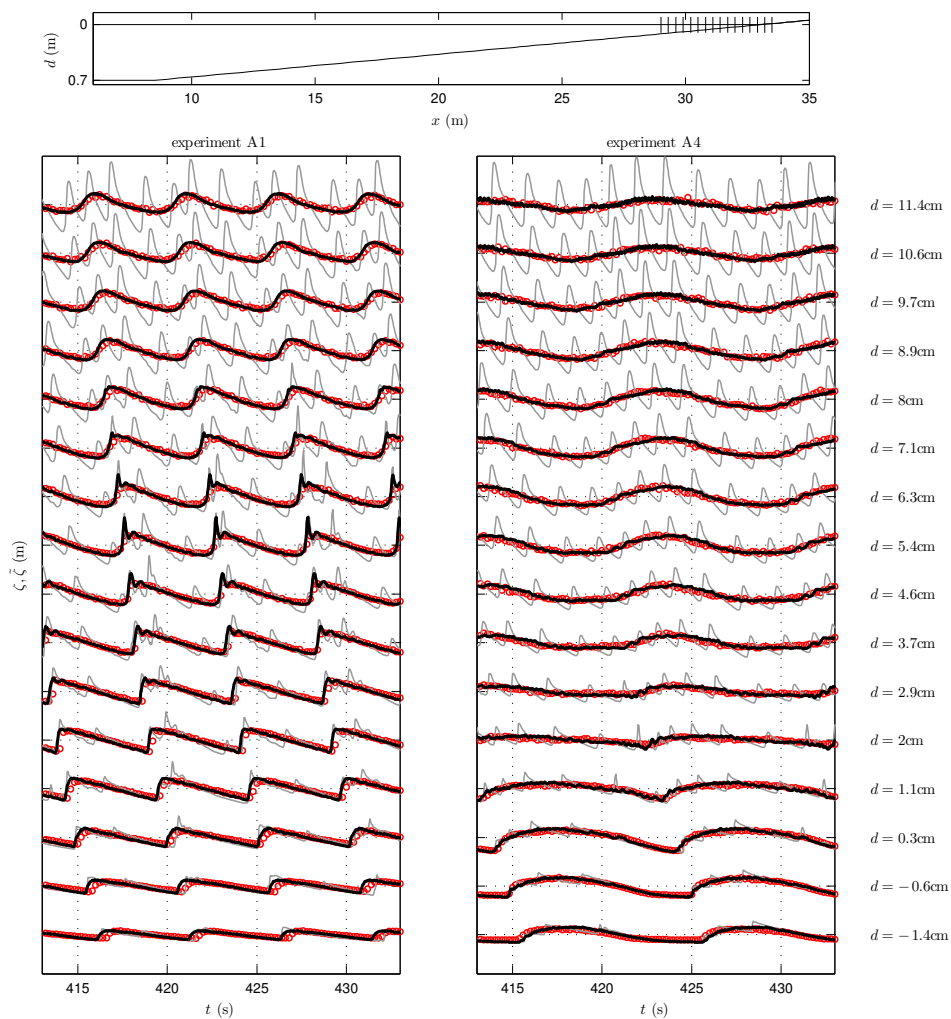


Figure 3.5: Time series of the infragravity wave signal $\tilde{\zeta}$ at several gauge locations close to the shoreline for experiment A1 (left panel) and A4 (right panel). Measurements (markers); SWASH results (solid line). The grey line is the computed surface elevation. The top panel shows the bathymetry and gauge locations.

Table 3.2: Skill factors for the van Noorloos experiments.

	H_{rms}	\tilde{H}_{rms}	\tilde{H}_{rms}^+	\tilde{H}_{rms}^-
A1-4	0.95	0.85	0.85	0.70
B1-4	0.92	0.87	0.89	-0.07
Overall	0.94	0.86	0.87	0.32

Finally, we consider the model performance for all bichromatic wave experiments. To quantify the accuracy of the model we compute the model skill as (e.g., Reniers et al., 2006),

$$\text{Skill} = 1 - \sqrt{\frac{\frac{1}{N} \sum_{n=1}^N (X_p - X_o)^2}{\frac{1}{N} \sum_{n=1}^N (X_o)^2}}, \tag{3.8}$$

where N is the total number of observations and X is the considered quantity with subscript p and subscript o denoting predicted and observed values. Predicted H_{rms} agree well with the observations, as indicated by the overall skill factor of 0.94 (Table 3.2). Similarly, predicted and observed \tilde{H}_{rms} agree for all experiments, although the scatter is larger and the overall skill is lower compared to the results for H_{rms} . Predicted and measured \tilde{H}_{rms}^+ agree well and the skill is similar to that of \tilde{H}_{rms} . In contrast, errors in predicted \tilde{H}_{rms}^- are large as indicated by the low overall skill. Errors in predicted \tilde{H}_{rms}^- are largest for the results of experiment B1-4, for which the skill factor is negative which indicates that errors in predicted \tilde{H}_{rms}^- are larger than measured \tilde{H}_{rms}^- . For these dissipative infragravity wave conditions, outgoing infragravity wave energies are very small and minor errors in the modelled dissipation can result in large errors in outgoing infragravity wave energies. To illustrate this we consider the relative difference between the incoming and outgoing infragravity energy flux D . If we assume the group velocity of the incoming and outgoing infragravity waves are approximately equal in magnitude, we can define D as

$$D = 100 \frac{|\tilde{E}^+ - \tilde{E}^-|}{\tilde{E}^+}, \tag{3.9}$$

where \tilde{E}^\pm is the energy of an incoming (+) or outgoing (-) infragravity wave component at the outer edge of the surf zone ($x = 25\text{m}$). This shows that in experiment A1, B1-4 infragravity wave energy losses are large and that errors in predicted D are small ($\approx 3\%$, see

Table 3.3: Relative infragravity wave energy losses D (%) in the surf zone for the van Noorloos experiments.

	A1	A2	A3	A4	B1	B2	B3	B4
Measurements	98.5	95.9	80.2	37.2	98.4	98.5	99.3	99.7
SWASH	98.3	92.8	76.8	45.5	95.2	95.1	96.7	96.6

Table 3.3), which indicates that SWASH captures the bulk energy dissipation of a breaking infragravity wave. Although errors in the bulk dissipation are small for experiment B1-4, the model skill for the outgoing infragravity wave heights is low, which indicates that small errors in the predicted bulk dissipation of a breaking infragravity wave can result in large errors in the predicted outgoing infragravity wave heights.

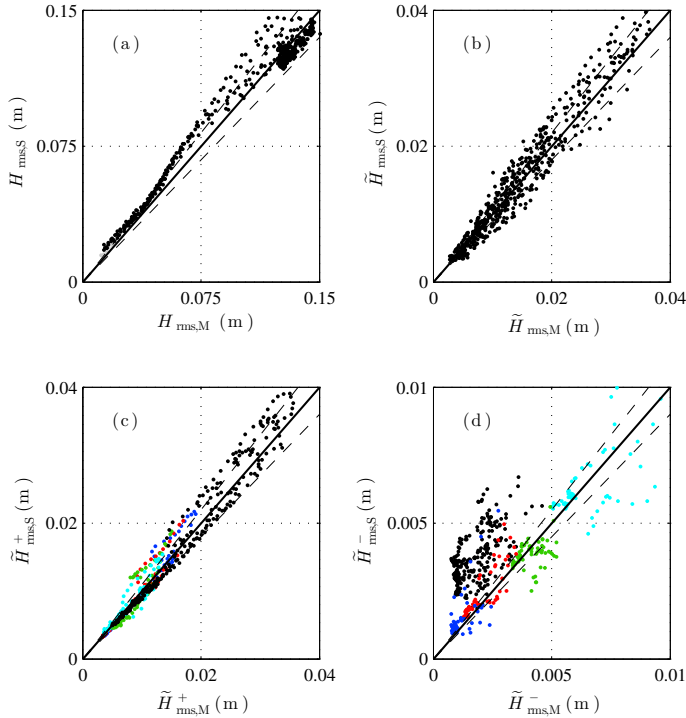


Figure 3.6: Predicted (subscript S) versus measured (subscript M) wave heights for the total wave height H_{rms} (a), infragravity wave height \tilde{H}_{rms} (b), incoming infragravity wave height \tilde{H}_{rms}^+ (c) and outgoing infragravity wave height \tilde{H}_{rms}^- (d). In panel c and d, a distinction is made between the various infragravity wave conditions, ranging from dissipative (A1) to reflective (A4), using the following colors: A1 (blue); A2 (red); A3 (green); A4 (cyan) and B1-4 (black). The solid line indicates one to one correspondence and the dashed lines are the 10 % error bands).

3.5. INFRAGRAVITY WAVES INDUCED BY RANDOM WAVES OVER A BARRED BEACH

The second flume experiment we consider in this study was performed by Boers (1996), who considered irregular waves propagating over a barred beach (see Fig. 3.7) in the same flume as Van Noorloos (2003). A variety of incident wave conditions were simulated with this set-up of which the lowest steepness wave condition (1C) has been anal-

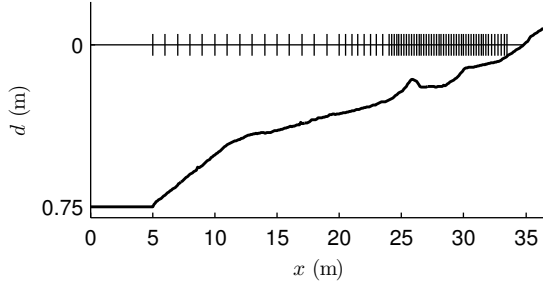


Figure 3.7: Boers (1996) experimental set-up. The still water level is located at $z = 0\text{m}$ and the vertical lines indicate the gauge locations.

used extensively in other studies (e.g., Janssen et al., 2003; Battjes et al., 2004). Here we shall also analyse this case, in which the shoaling of infragravity waves was most distinct, as it is the most relevant wave condition for studying the infragravity wave dynamics. In experiment 1C waves were generated at the wavemaker based on a target JONSWAP spectrum with a significant wave height of 0.103m and a peak period of 3.33s. Measurement of the free surface were taken at 70 locations, with intervals varying from 1m to 0.18m, for a duration of 28 minutes.

SWASH is employed with two vertical layers to capture the bound infragravity wave response (Appendix 3.B) and the propagation of short waves with frequencies up to three times the peak frequency f_p (with $kd = 2.5$). The grid resolution is set at $\Delta x = 0.02\text{m}$, which corresponds to at least 20 points per wave length for waves up to $3f_p$, and the time step is set at $\Delta t = 0.002\text{s}$. The incoming boundary is located at the first wave gauge and we employ a second-order accurate weakly reflective boundary condition (§3.3) based on the free wave components. The target free wave components with which the wavemaker in the flume is forced are not available and no velocities were measured near the wavemaker. Therefore, the incident free wave components can only be obtained based on measurements of the free surface at the first wave gauge. We estimate these components using the Fourier transform and a high-pass filter of $f > f_p/2$ to remove most bound infragravity wave components, since their contribution is accounted for by including the theoretical second-order response. The roughness coefficient is set at the same value as in the previous laboratory case ($d_r = 0.0075\text{m}$). Model and measured signals are analysed excluding a spin-up time of 60s ($> 4L_s/c_g$), where L_s is the length of the flume and c_g is the group velocity according to the peak frequency at the wavemaker.

RESULTS

First we compare measured and predicted significant wave heights H_{m0} ($= 4\sqrt{m_0}$) and wave periods T_{m01} ($= \sqrt{m_0/m_1}$) of short- and infragravity waves. In these definitions, the moments m_n ($= \int f^n E(f) df$) are computed from the variance density spectra $E(f)$ of the free surface elevation. The variance density spectra are computed with smoothing in the frequency domain and have 30 degrees of freedom. To distinct between short and infragravity waves, we compute their bulk parameters from the band-passed filtered

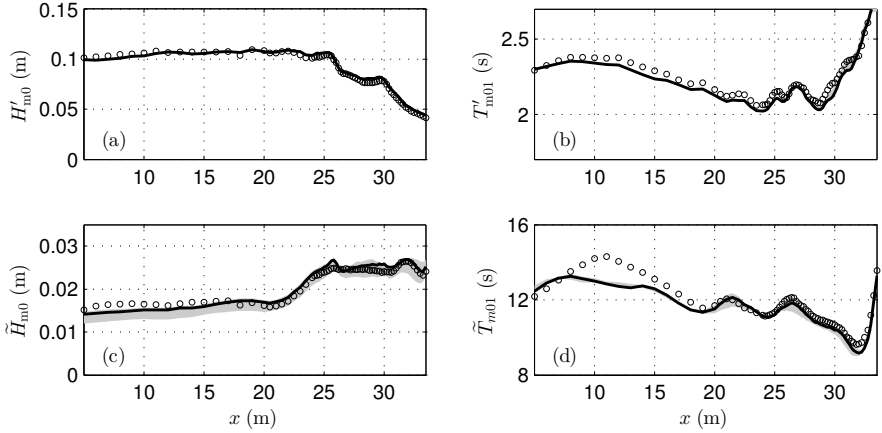


Figure 3.8: Cross-shore variation of the significant wave heights H_{m0} (a,c) and mean wave periods T_{m01} (b,d) of short waves (panel a and b) and infragravity waves (panel c and d). Comparison between measured (markers) and predicted values (line). The grey region gives the range in wave heights found when varying the roughness coefficient.

variance density with a band pass of $0.5f_p < f \leq 4f_p$ and $0.1f_p < f \leq 0.5f_p$, respectively. We take the peak frequency as the peak frequency at the wavemaker ($f_p = 0.3\text{Hz}$). In the remainder of this section parameters calculated from the high-frequency band are denoted with a prime accent ($'$), and parameters computed from the low-frequency band with a tilde accent ($\tilde{}$).

Predicted bulk wave parameters (significant wave height and mean wave period) of both short and infragravity waves are in agreement with the measurements throughout the domain (Fig. 3.8), despite of an under prediction of \tilde{T}_{m01} for $8\text{m} < x < 20\text{m}$.

To quantify the magnitude of incoming and outgoing infragravity wave components, we employ the improved signal decomposition method (Van Dongeren et al., 2003) of Battjes et al. (2004) with nine sensors for lower frequencies ($f \leq 0.11\text{Hz}$) and five for the remaining higher frequencies ($f \leq f_p/2$). This is the same number of sensors as Battjes et al. (2004) used in their analysis of the same data set. The measured \tilde{H}_{m0}^+ increases in shoreward direction with a rate which exceeds Green's law for energy conservative shoaling (Fig. 3.9a). As the short waves break ($x > 25\text{m}$), the growth rate of incoming infragravity waves reduces but remains positive throughout most of the surf zone ($x > 25\text{m}$). Outgoing infragravity waves decrease in height as they propagate in off-shore direction, in accordance with Green's law. Throughout the domain measured \tilde{H}_{m0}^+ are larger than measured \tilde{H}_{m0}^- , especially for $x > 25\text{m}$ where the difference is largest. Computed \tilde{H}_{m0}^+ are in agreement with observation for $x > 22\text{m}$, whereas they are under predicted for $x < 22\text{m}$. The \tilde{H}_{m0}^- is over predicted throughout the domain, but the overall pattern and magnitude is in reasonable agreement with the measurements. To identify the cause of the under prediction of \tilde{H}_{m0}^- for $x < 22\text{m}$, we compare the results with the target bound wave height, which is computed as the integral of the theoretical bound wave energies over the ig-frequency range, based on the incident free-wave components. To compare

the target bound wave height with the most seaward located prediction of \tilde{H}_{m0}^+ , we assume that for $x < 10\text{m}$ the amplitude increase of the incoming infragravity waves is in the order of Green's law (which is in agreement with the mild amplitude increase observed for $x < 20\text{m}$). The resulting target bound wave height at $x = 9\text{m}$ is of similar magnitude as the predicted \tilde{H}_{m0}^+ , whereas it is smaller than the measured \tilde{H}_{m0}^+ at this position. This is in accordance with Battjes et al. (2004), who observed that the measured incident \tilde{H}_{m0}^+ is larger than the equilibrium bound wave height. Discrepancies between model results and the measurements are therefore related to differences between the wave forcing in the flume and in the numerical model. A possible explanation is that, in the flume, the wavemaker generated some (spurious) free-wave energy at infragravity wave frequencies, for example, due to re-reflections of outgoing infragravity waves.

The previous analysis was restricted to the total infragravity band ($f_c/10 < f < f_c/2$). Now, we consider the incoming and outgoing infragravity wave heights for two separate frequency bands, which range between the ig-frequency limits with a fixed width of

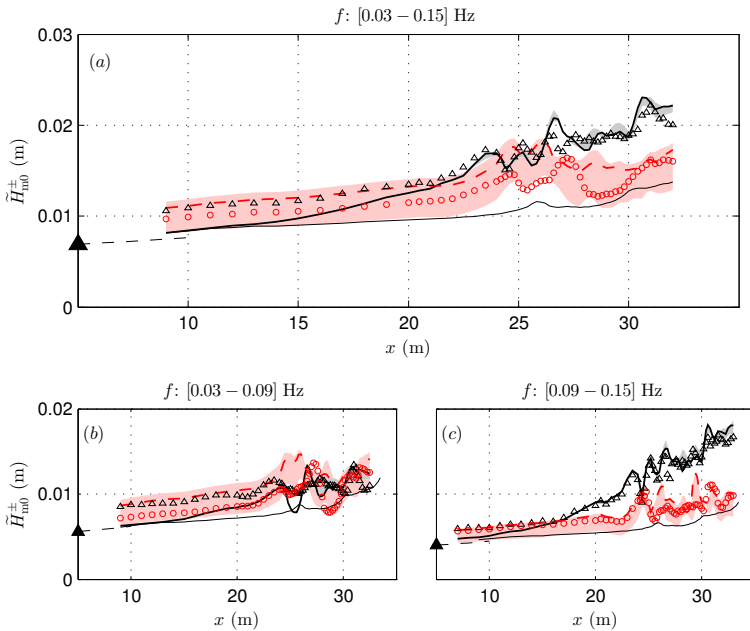


Figure 3.9: Cross-shore variation of incident \tilde{H}_{m0}^+ and outgoing infragravity wave heights \tilde{H}_{m0}^- , computed by integration over different frequency bands. Comparison between measured (incoming component: black triangles, outgoing component: red circles) and predicted values (incoming component: black line, outgoing component: dashed red line). The shaded regions indicate the maximal and minimal wave heights encountered in the simulations with a variation in the roughness coefficient (incoming component: grey, outgoing component: light red). The shaded triangle is the target bound infragravity wave height and the thin black curves indicates Green's law for energy conservative shoaling ($H \propto d^{-1/4}$), initiated with either the predicted incoming infragravity wave height at $x = 9\text{m}$ (full line), or the target bound infragravity wave height (dashed line).

6Hz. For the higher frequencies (Fig. 3.9c), the growth of incoming infragravity waves is relatively strong and they are more energetic than the outgoing infragravity waves. In contrast, for lower frequencies the incoming infragravity waves are less energetic (Fig. 3.9b), compared to the outgoing infragravity waves, and have a smaller growth rate compared to their counterparts at higher frequencies. Predicted wave heights are in agreement with the measurements for both frequency bands, although \tilde{H}_{m0}^+ is under and \tilde{H}_{m0}^- is over predicted for the lower frequency band.

Similar to the previous laboratory case we investigate the influence of the roughness coefficient for a coefficient ranging $d_r = 0.001 - 0.02m$. Again, the roughness coefficient has a small influence on the magnitude of short waves (Fig. 3.8) and incoming infragravity waves, whereas it has a significant influence on the outgoing infragravity wave height (Fig. 3.9a). The influence of the roughness coefficient is most pronounced for infragravity waves with relatively low frequencies (Fig. 3.9b).

It is well established that in waters of constant depth the wave envelope and bound infragravity waves are in equilibrium and out of phase with one-another (e.g., Longuet-Higgins and Stewart, 1960). However, as waves propagate over regions with varying depths, a phase shift away from the 180° equilibrium difference develops as the bound waves lag behind the wave envelope (e.g., Janssen et al., 2003, and references therein). This can be illustrated using a cross-correlation analysis, which determines the relation between short-wave envelope and infragravity waves. This technique has been applied to the Boers data set by several authors (e.g Janssen et al., 2003; Torres-Freyermuth et al., 2010) to analyse the propagation and reflection of infragravity waves.

The normalised cross-correlation function between two real signals $V(t)$ and $Y(t)$ is defined as

$$R_{VY}(\tau) = \frac{\langle V(t)Y(t+\tau) \rangle}{\sigma_V \sigma_Y}, \quad (3.10)$$

where τ is a time shift and σ_V and σ_Y are standard deviations of $V(t)$ and $Y(t)$, respectively. We define the short-wave envelope as the absolute value of (Janssen et al., 2003)

$$A(t) = |\zeta'(t) + i\mathcal{H}\{\zeta'(t)\}|_{lp}, \quad (3.11)$$

where $\mathcal{H}\{\dots\}$ is the Hilbert transform operator and $|\dots|_{lp}$ denotes a low pass filter operation ($f < 0.5f_p$).

Here, we evaluate the cross-correlation between the squared wave envelope and infragravity wave surface elevation signal for the measurements and the model predictions. Fig. 3.10 shows the measured (panel a) and computed (panel b) cross-correlation function. In the measurements, a clear trough of negative correlation is present around zero time lags for $x < 30m$, consistent with the theory of Longuet-Higgins and Stewart (1962), which predicts a bound infragravity wave which is out of phase with the wave groups. For $x > 25m$ the correlation increases as the short waves are breaking and further shoreward ($x > 30m$) the correlation is eventually reversed. This positive correlation is associated with the fact that infragravity waves modulate the total water depth (Janssen et al., 2003), as the presence of an infragravity wave crest increases the water depth whereas an infragravity wave trough decreases the water depth. This allows depth-limited short waves to enter shallow water on the crest of an infragravity wave, which results in a positive correlation. A second trough of negative correlation is present

at greater time lags, which is linked to the reflected infragravity wave (e.g., Janssen et al., 2003). Close to the wavemaker ($x = 5\text{m}$) the minimum value of correlation that is associated with an incoming bound infragravity wave is located at $\tau = 0\text{s}$, whereas closer to the shore the minimum value is located at increased time lags. This is further illustrated in Fig. 3.10c, which shows the time lag, normalised with a representative bound wave period $T_b (= 1/0.3f_p)$, of the minimum correlation value between $-5\text{s} < \tau < 5\text{s}$ (which corresponds to the incoming bound infragravity wave) up to the location of the second breaker bar ($x \approx 30\text{m}$). The measured normalised phase lag increases significantly for $x > 20\text{m}$ and reaches a value of ≈ 0.4 for $x > 27\text{m}$, which corresponds to a phase difference of 36° between the wave envelope and a representative bound wave. Model predictions agree with the measurements, both in a qualitative manner (Fig. 3.10a and b) and a quantitative manner (Fig. 3.10c).

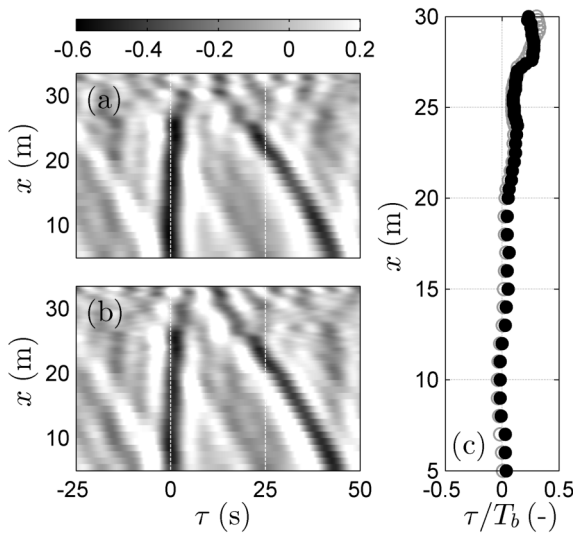


Figure 3.10: Cross-correlation between the squared wave envelope and the infragravity wave surface elevation signal for the measurements (panel a), and computations (panel b). Panel c shows the measured (grey circles) and computed (filled black circles) time lags, normalised with a representative bound period, between the wave envelope and bound infragravity waves.

3.6. DISCUSSION

The overall good correspondence between model results and measurements found in this study demonstrates that SWASH – which is essentially an intermediate approach between RANS and phase-averaged models – is able to resolve the cross-shore evolution of infragravity waves. SWASH accounts for the dominant processes that affect the energy balance at the ig-frequencies: the nonlinear energy exchange with the high-frequency waves, the loss of energy due to friction and infragravity wave breaking. The energy exchange with the hf-waves outside the surf zone is best represented in the model, as it is

an intrinsic property of the governing equations. However, the accuracy of the modelled nonlinear interactions depends on the spatial resolution that is used (see e.g., Fig. 3.B1). On the other hand, bottom friction and (infragravity wave) breaking are parametrized and with that model performance depends on how sensitive predictions are to (small) errors in the modelled dissipation related to these processes.

In this study predictions of the incoming wave field proved to be insensitive to variations in the bottom friction (by means of the roughness coefficient). In contrast, under (mildly) reflective wave conditions the outgoing infragravity wave heights are sensitive to the bottom friction. In such cases, an accurate prediction of the outgoing infragravity wave field requires calibration of the roughness coefficient. Although a different friction formulation might reduce model sensitivity, it is unlikely that the need to calibrate the friction coefficient can be avoided without taking the effect of enhanced turbulence due to wave breaking into account (Feddersen et al., 2003).

Depth-induced wave breaking of the short waves is well resolved within SWASH as the relatively simple model used (bore dissipation with an enforced hydrostatic pressure distribution) is able to resolve the evolution of bulk wave parameters and wave spectra, including nonlinear wave-interactions, in high-detail throughout the surf zone (e.g., Smit et al., 2014). This gives confidence that SWASH accounts for the energy exchange between ig- and hf-waves in the surf zone. Moreover, the present study shows that SWASH captures the bulk energy dissipation of a breaking infragravity wave. However, for such dissipative infragravity wave conditions errors in predicted outgoing infragravity wave heights are large, because the relatively small outgoing energies are sensitive to minor errors in the predicted bulk energy dissipation. Nonetheless, the model has good skill in predicting the total infragravity wave heights demonstrating that the low skill regarding the outgoing infragravity waves does not inhibit the use of SWASH for the prediction of infragravity waves.

The primary advantage of SWASH compared to RANS models is that the accuracy of predicted bulk wave parameters (including sea, swell and ig-contributions) is comparable, whereas the computational effort is much smaller. For example, the agreement with observed (ig-) wave heights for the Boers experiment (§3.5) is similar to the results of Torres-Freyermuth et al. (2010), who used a RANS model with 82 cells in the vertical, as opposed to two vertical layers used here, to reproduce this experiment. Naturally, if more detail with regard to the vertical structure is required, for instance to capture the wave-induced cross-shore circulation, SWASH may be employed with a finer vertical resolution (at larger computational costs). However, if only bulk parameters are of interest, the present approach forms an attractive alternative. Moreover, the non-hydrostatic approach is more flexible compared to Boussinesq-type models, which operate on a similar intermediate scale, as it can flexibly adapt itself to allow for an optimum balance between accuracy and computational effort.

Nevertheless, the prediction of infragravity wave conditions in a two-dimensional surf zone, for routine applications, will likely remain in the class of models that combine a wave driver with the nonlinear shallow water equations. Such models, although more approximate, remain an order of magnitude faster as they do not resolve individual waves, but calculate on the wave-group scale. On the other hand, the use of linear wave theory for the evolution of the short waves and the absence of phase informa-

tion implies that in regions where the waves are strongly nonlinear, or where reflection and/or diffraction (e.g., a harbour) are important, the present approach is preferable to the phase-averaged approach. We stress that there are no fundamental barriers to apply SWASH to two-dimensional infragravity wave propagation cases. For instance, when the calculations are performed on present-day large-scale multi-processor machines (with $O(100)$ processors), the application of the present model to study infragravity wave conditions in, for example, a large harbour, for select engineering (e.g., calculating extreme conditions) or scientific purposes, is viable.

3.7. CONCLUSIONS

In the present study we considered the modelling of infragravity wave dynamics using the non-hydrostatic model SWASH. Hereto we extended SWASH with a second-order weakly-reflective wavemaker, based on weakly nonlinear wave theory, in order to include the incident (bound) infragravity wave contributions. Model results were compared with flume observations of the nearshore transformation of infragravity waves. Our results demonstrate that SWASH is able to reproduce the phenomena commonly associated with the evolution of infragravity waves in the nearshore, including the shoaling of bound infragravity waves, shoreline reflections, the phase lag between the wave envelope and the incoming infragravity waves, nonlinear (self-self) interactions and the occurrence of infragravity wave breaking. In particular, our analysis shows that the total and incoming infragravity wave heights are well predicted. Errors in predicted outgoing infragravity wave heights are larger compared to the total and incoming infragravity wave height, and are found to be sensitive to the roughness coefficient (which controls the dissipation due to bottom friction) and to the location of incipient short-wave breaking (which is controlled by the breaking threshold). Model results further indicate that bottom friction has a marginal influence on the incoming wave field and only affects the magnitude of outgoing infragravity waves in case of (mildly) reflective infragravity wave conditions. This study suggests that SWASH can be a valuable tool, for engineering and scientific purposes, to study the evolution of cross-shore propagating infragravity waves.

APPENDICES

3.A. SECOND-ORDER BOUNDARY CONDITION

To include the ig-response into our boundary signal, we make use of weakly nonlinear, second-order, finite-depth theory (e.g., Longuet-Higgins and Stewart, 1960; Hasselmann, 1962). Herein the wave field is composed of first-order, or primary waves that corresponds to the free wave response (single summation in Eq. (3.6)), and a small second order correction that is associated with the bound waves (double summation in Eq. (3.6)). Here, we estimate the amplitude of the second order response, due to the primary waves at f_m and f_n , following Hasselmann (1962)

$$a_{nm} = D_{nm} a_m a_n, \quad (3.A1)$$

where a_{nm} is the amplitude of a bound wave component, a_n and a_m denote the amplitudes of the associated primary waves, and D_{nm} is the interaction coefficient. In this study we are primarily interested in the difference interactions, with difference frequency $f_{nm} = f_m - f_n$ and difference wave number $k_{nm} = k_m - k_n$, for which the interaction coefficient can be expressed as

$$D_{nm} = -\frac{gk_n k_m}{2\omega_n \omega_m} + \frac{\omega_n^2 - \omega_n \omega_m + \omega_m^2}{2g} - C \frac{g(\omega_n - \omega_m)}{\omega_n \omega_m [gk_{nm} \tanh(k_{nm}d) - (\omega_n - \omega_m)^2]}, \quad (3.A2)$$

where $\omega (= 2\pi f)$ is the radial frequency and coefficient C is defined as

$$C = (\omega_n - \omega_m) \left(\frac{(\omega_n \omega_m)^2}{g^2} + k_n k_m \right) - \frac{1}{2} \left(\frac{\omega_n k_m^2}{\cosh^2(k_m d)} - \frac{\omega_m k_n^2}{\cosh^2(k_n d)} \right). \quad (3.A3)$$

Because SWASH is forced by means of the horizontal particle velocity, the free surface amplitudes need to be related to the horizontal velocity amplitudes. In principle, this can be done using second-order theory. However, because in this study the long wave response is generally in shallow water ($k_{nm}d \ll 1$), a good approximation of the depth averaged second-order velocity amplitude \hat{u}_{nm} follows from mass conservation in combination with the assumption that bound infragravity waves are progressive and of constant form,

$$\hat{u}_{nm} = \frac{c_g}{d} a_{nm}, \quad (3.A4)$$

where c_g is the group velocity which is expressed as $c_g = 2\pi f_b / k_{nm}$. This form is easier to implement and more efficient to compute compared to the full second-order theory. The above boundary condition, valid for unidirectional waves perpendicular to the boundary, can be extended to short-crested waves (directional seas) as the original interaction coefficient of Hasselmann (1962) puts no restriction on wave directions.

The interaction coefficient is derived with the assumption of weak nonlinearity, therefore, the above boundary condition is only valid for small wave amplitudes $a/d \ll 1$. Furthermore, the assumption of a depth averaged second-order velocity amplitude requires $k_{nm}d \ll 1$. These considerations imply that the proposed boundary condition cannot be used in the surf zone ($a/d < 1$) and in deep water ($k_{nm}d > 1$). Nevertheless, for most practical applications, including the simulations considered in this study, the boundary will be located in intermediate water depths where these limitations are not met. Furthermore, in deep water the second-order response is small can – to a good approximation – be neglected. In such case, a boundary condition based on linear wave theory is likely sufficient.

3.B. SWASH SECOND-ORDER RESPONSE

To verify the second-order boundary condition, and to investigate the sensitivity with regard to the vertical resolution, we compare the model response with the classical finite depth solution of Longuet-Higgins and Stewart (1960). Here we consider a situation where a bound infragravity wave is forced by, and in equilibrium with, two free waves which propagate over a flat bottom. The accuracy with which the bound-solution is reproduced by SWASH is likely related to the number of vertical layers, as the dispersive and nonlinear properties of SWASH improve with an increased number of layers. Furthermore, at low resolutions a spurious free wave with the same frequency as the bound infragravity wave might be generated. Such a spurious free wave is most pronounced when the second order response is not incorporated. In this case a spurious free wave is generated, out of phase with but of equal amplitude as the bound wave, which exactly cancels the bound wave at the wavemaker. Hence, inclusion of the second-order response is vital to avoid generating artificial free-energy at the ig-frequencies. However, because SWASH will not exactly reproduce second-order theory some spurious free-energy is still generated, even when the infragravity waves are included at the boundary.

To properly estimate the bound energy which is generated, and to investigate the magnitude of the spurious free wave, we need to decompose the energy associated with the low-frequency motion into bound and free energy. Given that the free and bound wave have identical frequencies, this decomposition cannot be done in the frequency domain. Instead, we will perform the decomposition in the wave number domain as a bound wave and its spurious counterpart have different wave numbers (the bound wave number is equal to the difference wave number and the free wave number follows from the difference frequency and the linear dispersion relationship). We estimate their respective energies using a spatial Fourier transform, which results in the complex wave amplitude a_k at wave numbers k . In this manner we can estimate the energy associated with the free or bound wave components (\tilde{E}_f and \tilde{E}_b , respectively) with

$$\tilde{E}_f = \sum_{\delta k_f} \frac{1}{2} a_k a_k^*, \quad \tilde{E}_b = \sum_{\delta k_b} \frac{1}{2} a_k a_k^*, \quad (3.B1)$$

where $*$ denotes the complex conjugate and $\delta k_{b/f}$ denote the wave number range around the free (subscript f) or bound (subscript b) wave numbers.

Model results and analytical solutions are analysed for fixed free-wave amplitudes ($a_1 = a_2 = 0.01\text{m}$), fixed free-wave frequencies ($f_1 = 0.10\text{Hz}$ and $f_2 = 0.11\text{Hz}$) and varying still water depths which range from 7.5 to 65m. This range of still water depths results in a minimum and maximum kd value of 0.5 and 2.5, respectively. Numerical simulations are performed with one to four vertical layers and a grid resolution of $\Delta x < \lambda/100$, where λ is the wave length of the second free wave component (which corresponds to the shortest wave length). A radiation condition, in combination with a sponge layer, was employed to minimise wave reflections at the outlet of the domain. The roughness coefficient and vertical viscosity are equal to zero to prevent wave damping. Numerical and analytical surface elevations were outputted for a domain length of L , such that the signals contain at least 75 bound waves, with a resolution of Δx . A visual inspection of the computed complex amplitudes showed that with a wave number range of $\delta k_{b/f} = k_{b/f} \pm 5\Delta k$, where $\Delta k = 1/L$, most bound and spurious wave energies were included in the estimation of $\tilde{E}_{f/b}$.

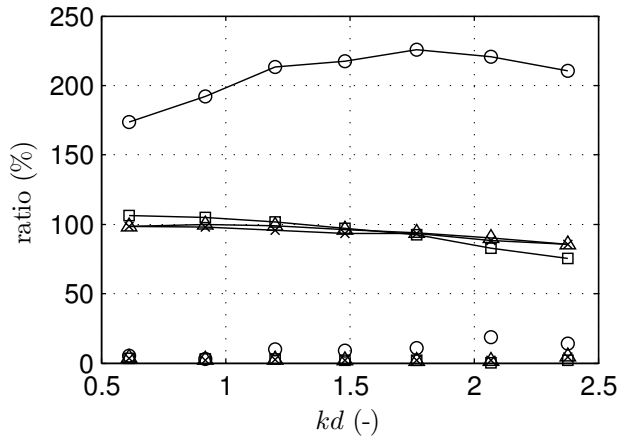


Figure 3.B1: The ratio of the numerical spurious free and the analytical bound energy (markers) and ratio of the numerical and analytical bound energy (marked lines), for a simulation with 1 (circles), 2 (squares), 3 (triangles) and 4 (crosses) vertical layers.

The second-order boundary condition successfully suppresses the generation of spurious free infragravity waves, although some spurious energy is present for simulations with one vertical layer (Fig. 3.B1). Predicted and analytical bound infragravity wave energies are in good agreement for two to four vertical layers, whereas it is over predicted by the one layer model. This indicates that the response of the depth-averaged model is different than the response of a multi-layer model. A multi-layer model under predicts the bound wave height for greater kd values, which is largest in case of two vertical layers. Furthermore, with two vertical layers the bound energies are overestimated for lower kd values. Nevertheless, numerical results are in agreement with the analytical solutions. These results indicate that at least two vertical layers are required to predict a bound infragravity wave response which is in accordance with the classical finite depth theory of Longuet-Higgins and Stewart (1960).

4

INFRAGRAVITY-WAVE DYNAMICS IN A BARRED COASTAL REGION, A NUMERICAL STUDY*

ABSTRACT

This paper presents a comprehensive numerical study into the infragravity-wave dynamics at a field site, characterised by a gently-sloping barred beach. The non hydrostatic wave-flow model SWASH was used to simulate the local wave field for a range of wave conditions (including mild and storm conditions). The extensive spatial coverage of the model allowed us to analyse the infragravity-wave dynamics at spatial scales not often covered before. Overall, the model predicted a wave field that was representative of the natural conditions, supporting the model application to analyse the wave dynamics. The infragravity-wave field was typically dominated by leaky waves, except near the outer bar where bar-trapped edge waves were observed. Relative contributions of bar-trapped waves peaked during mild conditions, when they explained up to 50% of the infragravity variance. Near the outer bar, the infragravity wave growth was partly explained by nonlinear energy transfers from short-waves. This growth was strongest for mild conditions, and decreased for more energetic conditions when short-waves were breaking at the outer bar. Further shoreward, infragravity waves lost most of their energy, due to a combination of nonlinear transfers, bottom friction, and infragravity-wave breaking. Nonlinear transfers were only effective near the inner bar, whereas near the shoreline (where losses were strongest) the dissipation was caused by the combined effect of bottom friction and breaking. This study demonstrated the model's potential to study wave dynamics at field scales not easily covered by in-situ observations.

*This chapter has been published as Rijnsdorp, D. P., Ruessink, G., and Zijlema, M. (2015a): Infragravity-wave dynamics in a barred coastal region, a numerical study. *Journal of Geophysical Research: Oceans*, 120 (6), 4068–4089

4.1. INTRODUCTION

In coastal regions, the wave field is a composite of short waves, with periods ranging 2–20s, and infragravity waves, with periods ranging 20–200s (e.g., Munk, 1949; Tucker, 1950). Infragravity waves have small heights ($< 1\text{cm}$) in deep water (e.g., Webb et al., 1991), but their magnitude increases with decreasing water depth. Close to the shore, their height can increase to the order of 1m, especially during storm conditions (e.g., Guza and Thornton, 1982). Numerous studies have shown the relevance of infragravity waves in nearshore regions. For example, infragravity waves are important in the process of beach (e.g., Russell, 1993) and dune erosion (e.g., Van Thiel de Vries et al., 2008), may cause harbour resonance (e.g., Bowers, 1977), and can have a significant impact on moored ships (e.g., Naciri et al., 2004; Van der Molen et al., 2006).

The dynamics of infragravity waves have been extensively investigated by means of theoretical, field, laboratory and numerical studies. Theoretical studies have shown that infragravity waves are generated by nonlinear interactions between pairs of short-waves (e.g., Longuet-Higgins and Stewart, 1960; Hasselmann, 1962; Symonds et al., 1982). When shoreward-propagating infragravity waves do not fully dissipate, infragravity waves reflect at the shoreline, resulting in a standing infragravity wave pattern in the nearshore (e.g., Guza and Thornton, 1985). Recent studies have shown that infragravity-waves can dissipate a significant amount of their energy close to the shore (e.g., Van Dongeren et al., 2007; Pomeroy et al., 2012; De Bakker et al., 2014). Three mechanisms have been proposed in the literature that can cause energy losses at the infragravity frequencies. First, studies have indicated that energy can be transferred from the infragravity waves to the short waves (Thomson et al., 2006; Henderson et al., 2006; Ruju et al., 2012; Guedes et al., 2013). Second, infragravity waves can break and lose most of their energy in a region close to the shore (Van Dongeren et al., 2007; De Bakker et al., 2014, 2015). Third, infragravity waves can lose energy due to bottom friction, although this mechanism is mainly significant in the case of extensive shallow regions such as coral reefs (Pomeroy et al., 2012; Van Dongeren et al., 2013).

Seaward directed infragravity waves can propagate to deep water (i.e., leaky waves) or can be trapped in the nearshore by refraction (i.e., edge waves). Several field studies have indicated that most seaward directed infragravity waves are trapped nearshore (e.g., Okihiro et al., 1992; Herbers et al., 1995). At beaches with relative monotonic depth variations, field observations of edge waves were in agreement with analytical solutions of edge waves on a plane beach (e.g., Oltman-Shay and Guza, 1987; Huntley et al., 1981). These edge wave solutions are characterised by a maximum amplitude at the shoreline, and an exponential decay in seaward direction. However, edge wave solutions are significantly altered on beaches with bars (Kirby et al., 1981; Schönfeldt, 1994; Bryan and Bowen, 1996; Bryan et al., 1998), and in the presence of strong longshore currents (Kenyon, 1972; Howd et al., 1992; Bryan and Bowen, 1998). In the case of a barred beach, edge waves can be trapped at the location of a bar. Such bar-trapped edge waves have a cross-shore structure that is characterised by a maximum amplitude near the crest of the bar, and an exponential decay away from this location. Bryan et al. (1998) found that bar-trapped edge waves dominated the edge-wave motion near the bar. Strong longshore currents can have a similar effect on the edge wave solution, and their effect is analogous to a modification of the actual bottom profile (Howd et al., 1992; Bryan and

Bowen, 1998). However, in the case of a pronounced bar, Bryan and Bowen (1998) found that the effect of the longshore current was generally not strong enough to significantly alter edge-wave trapping.

Numerous observational studies have been conducted at natural beaches using relatively short and sparse – but expensive – alongshore arrays of current and/or pressure sensors, combined with sophisticated estimation techniques to facilitate an analyses at infragravity-wave scales (e.g., Oltman-Shay and Guza, 1987). Although laboratory studies are easier instrumented, the scales over which infragravity-waves occur, and their sensitivity to bathymetric features and alongshore currents complicates a realistic replication of their nearshore dynamics in a laboratory setting. As an alternative, we use a wave resolving model to study the complex nearshore infragravity-wave evolution that occurs in a natural environment. The extensive spatial coverage of the model output supplemented spatially sparse in-situ observations, allowing us to study the variability of the infragravity-wave dynamics on a scale that was not often covered before. Amongst others, this allowed us to differentiate between the contribution of trapping and dissipation to the nearshore infragravity energy balance.

In this study, we used the recently developed SWASH model (Zijlema et al., 2011) to simulate a range of wave conditions that were measured at a field site near Egmond aan Zee (The Netherlands) as part of the Coast3D field campaign (e.g., Ruessink et al., 2001). The simulated wave conditions were varied from relatively mild to severe conditions, to gain insight in the spatial variability of the infragravity-wave dynamics for various wave conditions. Section 4.2 presents a description of the experimental data set, followed by a description of the numerical model. As a prerequisite to analyse the wave dynamics based on the model results, §4.3 compares predicted and observed wave parameters (e.g., wave heights), to assess if the predicted wave field represented the observed wave conditions. Section 4.4 presents a comprehensive analysis of the infragravity-wave dynamics. This includes an analysis of the spatial structure of the infragravity-wave field (e.g., identifying the presence of leaky and edge waves); and an analysis of the nearshore infragravity energy balance, to quantify energy exchanges between the short and infragravity-waves, and to determine which dissipation mechanisms were significant. The results of this study are discussed in §4.5 and summarised in §4.6.

4.2. METHODOLOGY

FIELD EXPERIMENT

Measurements of the wave field were obtained from October to November 1998 at a sandy beach near Egmond aan Zee, The Netherlands (Ruessink et al., 2001). Four bidirectional current meters and ten pressure sensors were positioned at the experimental site, which is characterised by a double bar system and a gentle slope (see Fig. 4.1). The instruments acquired data for approximately 34min every hour, at a sampling rate of 2 or 4Hz. A directional wave rider buoy, located 5km offshore at a depth of 16m, measured offshore wave conditions (the significant wave height $H_{m0,d}$, peak period $T_{p,d}$, and energy-weighted mean direction $\hat{\theta}_d$ (Kuik et al., 1988), which we refer to as the deep-water wave parameters). Wind speeds and directions were measured at position 7a, 10m above mean sea level. Surveys of the local bathymetry were conducted every few days,

see Ruessink et al. (2000) for more details.

A wide range of conditions was encountered during the two month experiment. The significant wave height ranged 0.2 – 5.2m, the peak period ranged 2.1 – 11.1s, and the mean wave direction varied between $\pm 45^0$ (relative to the shore normal). The neap and spring tidal range was approximately 1.4m and 2.1m, respectively. Alongshore variations in the bathymetry were relatively small for most of October. However, on 29 October a broad cross-shore channel developed near the location of the measurement transect (Ruessink et al., 2001) (Fig. 4.1b).

In this study, we analysed measurements and predictions for relatively mild ($H_{m0,d} \leq 1.5\text{m}$), moderate ($1.5\text{m} < H_{m0,d} \leq 3\text{m}$), and severe wave conditions ($H_{m0,d} > 3\text{m}$), belonging to two consecutive storm events. The first event (E1) corresponds to the most severe storm encountered during the experiment (25–29 October), and the second event (E2) corresponds to a storm that occurred after the development of the cross-shore channel (5–7 November). In the tables of this paper, we distinguish between the six cases using a code (e.g., E1a), which indicates the event (E1, or E2), and the wave condition (mild, a; moderate, b; or severe, c).

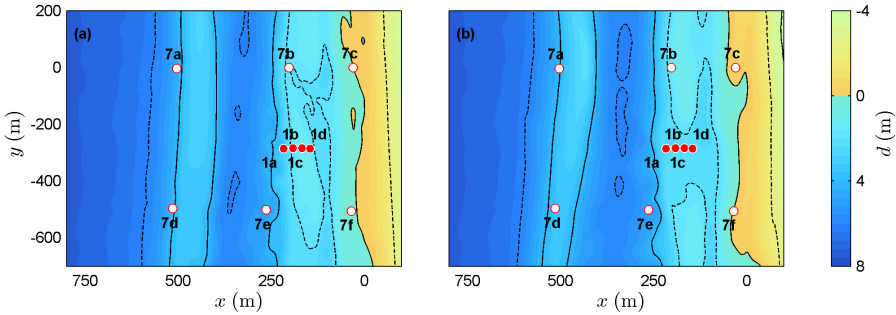


Figure 4.1: Plan view of the local bathymetry, relative to the Mean Sea Level and in local coordinates, at the Egmond field site for (a) October 24, 1998, and (b) November 12, 1998. A red circle with white filling indicates a pressure sensor (gauge 7a-f) and a white circle with red filling indicates a collocated bidirectional current meter and pressure sensor (gauge 1a-d). The black lines (solid and dashed) are depth contours.

NUMERICAL MODEL

Over the past years, non-hydrostatic models have become an increasingly popular tool to simulate wave-flow dynamics on a variety of scales. Applications range from the evolution of waves at coastal scales (e.g., Zijlema and Stelling, 2008; Yamazaki et al., 2009; Ma et al., 2012; Ai and Jin, 2012; Cui et al., 2012; Wei and Jia, 2014), to the evolution of tsunami waves at oceanic scales (e.g., Walters, 2005; Yamazaki et al., 2011). Furthermore, several authors have improved the efficiency of the non-hydrostatic approach (e.g., Bai and Cheung, 2012, 2013; Cui et al., 2014). In this study, we use the open-source non-hydrostatic wave-flow model SWASH to simulate the nearshore wave dynamics at the field site. SWASH has been successfully used to study various nearshore processes under laboratory conditions. This includes the nearshore evolution of short waves (Zijlema et al., 2011), the nearshore evolution of infragravity waves (Rijnnsdorp et al., 2014), the

depth-induced breaking of short waves (Smit et al., 2013), the nonlinear wave dynamics in the surf zone (Smit et al., 2014), and run-up oscillations (Ruju et al., 2014). Here, a brief description of the numerical model is given. A comprehensive description of the model can be found in Zijlema et al. (2011) and Smit et al. (2013).

GOVERNING EQUATIONS AND NUMERICAL IMPLEMENTATION

SWASH is based on the RANS equations for an incompressible flow with constant density. We consider a three-dimensional domain that is vertically bounded by a free surface $z = \zeta(x, y, t)$ and a bottom $z = -d(x, y)$, where t is time, and x, y and z are the Cartesian coordinates ($z = 0$ is still water level). In this framework, using the Einstein summation convention for the horizontal coordinates, the governing equations are,

$$\frac{\partial u_j}{\partial x_j} + \frac{\partial w}{\partial z} = 0, \quad (4.1)$$

$$\frac{\partial u_i}{\partial t} + \frac{\partial u_i u_j}{\partial x_j} + \frac{\partial u_i w}{\partial z} = -\frac{1}{\rho} \frac{\partial (p_h + p_{nh})}{\partial x_i} + \frac{\partial \tau_{ij}}{\partial x_j} + \frac{\partial \tau_{iz}}{\partial z}, \quad (4.2)$$

$$\frac{\partial w}{\partial t} + \frac{\partial w u_j}{\partial x_j} + \frac{\partial w^2}{\partial z} = -\frac{1}{\rho} \frac{\partial (p_h + p_{nh})}{\partial z} + \frac{\partial \tau_{zj}}{\partial x_j} + \frac{\partial \tau_{zz}}{\partial z} - g, \quad (4.3)$$

where subscript i and j refer to the two horizontal coordinates, u_i is the velocity component of \vec{u} in the i -direction, w is the vertical velocity component, g is the gravitational acceleration, ρ is the density, τ are the turbulent stresses, p_h is the hydrostatic pressure, and p_{nh} is the non-hydrostatic pressure. An expression for the free surface is derived by considering the mass balance over the entire water column,

$$\frac{\partial \zeta}{\partial t} + \frac{\partial}{\partial x_j} \int_{-d}^{\zeta} u_j dz = \frac{\partial \zeta}{\partial t} + \frac{\partial h_j U_j}{\partial x_j} = 0, \quad (4.4)$$

where $h (= d + \zeta)$ is the total water depth.

At the bottom boundary, turbulence is assumed to be generated by bottom friction,

$$\tau_{iz}|_{z=-d} = c_f \frac{U_i |\vec{U}|}{h}, \quad (4.5)$$

where c_f is a dimensionless friction coefficient. Feddersen et al. (1998) found that c_f is enhanced inside the surf zone due to breaking waves. We computed c_f using the Manning-Strickler formulation, $c_f = gn^2/h^{1/3}$, where n is the Manning roughness coefficient. This formulation gives increasing c_f values for decreasing depth, which makes it a suitable proxy to mimic the wave breaking enhanced c_f . In this study, n was set at $0.019 \text{ s/m}^{1/3}$, which results in c_f values of similar order of magnitude as found on a sandy beach (e.g., Feddersen et al., 1998, 2003; Ruessink, 2010). The turbulent stresses are based on a turbulent viscosity approximation. For example, the horizontal stresses are given by $\tau_{ij} = \nu_j \partial_{x_j} u_i$, where ν_j is the eddy viscosity. In this study, the horizontal viscosities were estimated using a Smagorinsky-type formulation (e.g., Smit et al., 2013). To include vertical mixing, the vertical viscosity was set at a constant value ($10^{-4} \text{ m}^2/\text{s}$).

This spreads the effect of the bottom stress term over the vertical and may improve the numerical stability.

The governing equations intrinsically account for the processes governing the near-shore (infragravity) wave evolution. However, the numerical methods used to discretise these equations, and the spatial and temporal resolution used in a simulation determine the accuracy with which these processes are resolved. In contrast with traditional non hydrostatic models (e.g., Casulli and Stelling, 1998), the numerical schemes used in the model to approximate the non hydrostatic pressure terms allow SWASH to resolve the nearshore wave evolution with a relatively coarse vertical resolution (Stelling and Zijlema, 2003) (1 – 3 layers versus 10 – 20 layers for the traditional approach). This allows model applications at relatively large horizontal scales. Consequently, SWASH captures the relevant physics in the nearshore (e.g., refraction, diffraction, shoaling, and nonlinear interactions) with only a few vertical layers. In this study, two vertical layers were employed.

The model also captures the bulk dissipation of a breaking wave, without the need to resolve detailed phenomena such as wave overturning (Smit et al., 2013). However, a fine vertical resolution (10 to 20 layers) is usually required to capture the initiation of wave breaking, which is not feasible for the horizontal scales considered in this study. Instead we used the hydrostatic front approximation that was implemented by Smit et al. (2013) to capture the onset of breaking with two layers. With this approximation, the non-hydrostatic pressure is neglected in the vicinity of a breaking wave, which ensures that the wave develops a vertical face (see Smit et al., 2013, for more details). This breaking formulation requires a breaking threshold (controlling the onset of wave breaking) and a breaking persistence parameter, which were set to the values found by Smit et al. (2013) for two vertical layers.

MODEL SETUP

The horizontal coordinates correspond to a local coordinate system, with the x axis positioned perpendicular to the shore and the y axis positioned parallel to the shore. A schematic view of the numerical domain is presented in Fig. 4.2. At the offshore boundary (the western boundary in Fig. 4.2), incident waves were generated using weakly nonlinear wave theory, based on a target wave spectrum. The target spectrum represents a directional random wave field, which is formed by a superposition of a large number of free wave components. Each wave component represents a linear (long-crested) harmonic wave, with a certain amplitude, period, direction and phase. The target spectrum was obtained with the spectral wave model SWAN (Booij et al., 1999), based on wave data measured by a buoy located 5km offshore (see Fig. 4.2). A description of the numerical wavemaker and the computation of the target wave spectrum is given in Appendices 4.A to 4.C. At the shore (the eastern boundary in Fig. 4.2), a moving-shoreline boundary condition was employed to accurately simulate wave run-up and flooding and drying (Stelling and Zijlema, 2003). At the lateral boundaries (the northern and southern boundaries), a cyclic boundary condition was prescribed to simulate the fluid motion on an unbounded beach.

A bathymetry was constructed for the first storm event, based on local survey data obtained on October 24, and for the second storm event, based on local survey data

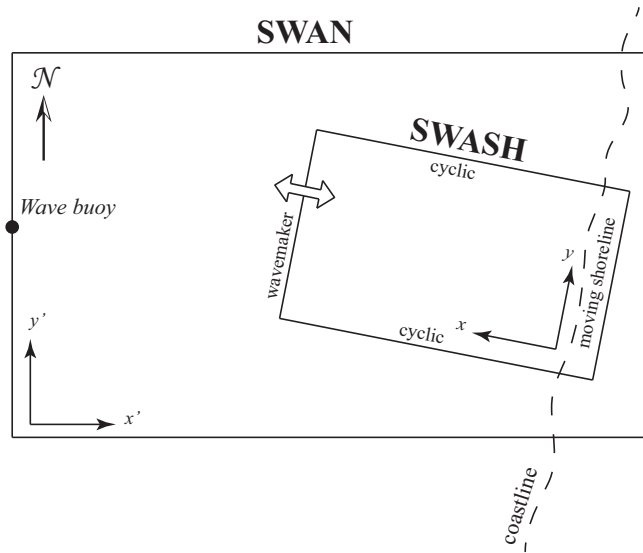


Figure 4.2: Sketch of the SWASH model domain and the SWAN model domain (not to scale).

obtained on November 12. Fig. 4.1 shows a plan view of the constructed bathymetry for both storm events. To construct a cyclic bathymetry in y direction, the bathymetry was extended from $y = -700\text{m}$ to $y = -1100\text{m}$, with a linear transition between the cross-shore profile at the northern boundary ($x = 200\text{m}$) and at $y = -700\text{m}$. The resulting numerical domain spanned $1400 \times 1300\text{m}$ ($x \times y$) for mild to moderate wave-conditions, and $2150 \times 1300\text{m}$ for severe conditions. This includes a region of constant depth at the western boundary, with a maximum depth of 15m for the severe conditions, and 10m for the mild and moderate conditions.

Table 4.1 shows an overview of the SWAN predicted bulk wave parameters, with which SWASH was forced. To accurately capture the characteristics of the dominant wave field, a grid resolution was chosen that ensured at least 15 points per wave length for waves up to $3f_p$, where f_p is the peak frequency of the target spectrum. This resulted in horizontal grid resolutions that varied between $\Delta x = 0.5 - 1\text{m}$, and $\Delta y = 0.8 - 1.4\text{m}$, depending upon the simulation. To resolve the dispersion of waves up to $3f_p$, two vertical layers were used. The time step ranged $\Delta t = 0.02 - 0.03\text{s}$. At the numerical wavemaker, the nonlinearity of the wave field should be small, as the wavemaker is based on weakly nonlinear wave theory. We quantified the nonlinearity using the Ursell number, based on the target bulk parameters (Table 4.1) and the depth at the wavemaker. The Ursell number ranged $3 - 16$, which is acceptable for the application of the numerical wavemaker (e.g., Holthuijsen, 2007).

For each simulation, the model was run for one hour and twenty minutes, including twenty minutes of spin-up time. Model variables (ζ , u , and v) were output with a sampling rate of 4Hz , at the measurement devices and at 66 cross-shore transects. These transects spanned the whole model domain with a resolution of 5m in x direction, and 20m in y direction.

Table 4.1: Target bulk wave parameters at the numerical wave maker, computed with SWAN. Listed are the wave height $H_{m_0} (= 4\sqrt{\int E(f)df}$, where $E(f)$ is the SWAN predicted variance density spectrum), the peak period T_p , the energy-weighted mean-wave direction $\bar{\theta}$, and the energy-weighted directional spreading $\bar{\sigma}_\theta$. Wave directions are related to the local coordinate system, where $\bar{\theta} = 90^\circ$ corresponds to northerly waves and $\bar{\theta} = -90^\circ$ corresponds to southerly waves.

	H_{m_0} (m)	T_p (s)	$\bar{\theta}$ ($^\circ$)	$\bar{\sigma}_\theta$ ($^\circ$)
E1a	1.2	6.1	35	21
E1b	2.2	7.8	29	21
E1c	4.7	10	-1	27
E2a	1.5	6.5	-15	22
E2b	1.9	7.4	3	24
E2c	3.7	8.7	-3	27

4

DATA ANALYSIS

We distinguished between wind-generated waves and infragravity waves by defining two frequency bands, one representing the infragravity waves ($0.005\text{Hz} < f \leq f_p/2$), and one representing the short waves ($f_p/2 < f \leq 3f_p$). These two adjacent bands are separated by a split frequency of $f_p/2$, which is similar to several previous studies (e.g., Janssen et al., 2003; Pomeroy et al., 2012). These frequency bands were used to decompose the surface elevation and velocity signals into an infragravity and short-wave component. In the following analyses, an infragravity wave signal is indicated by a tilde ($\tilde{\cdot}$), and a short-wave signal is indicated by a prime (\prime)

MODEL-DATA COMPARISON

To facilitate a model-data comparison, several parameters were computed for the model predictions and observations, using the same techniques and based on signals of equal length (34 minutes, the length of the observed signals). All (co)spectra in this section were computed with thirty degrees of freedom, based on ensemble averaged Fourier transforms of detrended and windowed time signals.

Significant wave heights were computed as $H_{m_0} = 4\sqrt{m_0}$, where $m_0 (= \int E(f)df)$ is the zeroth-order moment of the energy density spectrum $E(f)$ of the surface elevation. Infragravity and short-wave heights were computed by integrating spectra over their respective frequency bands. Directional properties, the mean wave direction $\theta(f)$ and directional spreading $\sigma_\theta(f)$, were computed following Kuik et al. (1988), based on second-order Fourier directional moments. Bulk short-wave directional properties were computed using an energy weighted integration over the short-wave frequencies (e.g. Feddersen et al., 2011).

To compare the predicted and observed nearshore energy losses of infragravity waves, bulk-infragravity reflection coefficients were computed based on cross-shore directed linear energy fluxes of shoreward and seaward propagating infragravity waves (superscript \pm , respectively), using the technique of Sheremet et al. (2002). Linear energy fluxes follow from collocated surface elevation and cross-shore directed velocity signals, as-

suming that the infragravity waves are shore-normal propagating shallow-water waves,

$$F_L^\pm(f) = \frac{1}{4} \sqrt{gd} \left(C_f(\zeta, \zeta) + \frac{d}{g} C_f(u, u) \pm 2 \sqrt{\frac{d}{g}} C_f(\zeta, u) \right), \quad (4.6)$$

where $C_f(X, Y)$ represents the co-spectrum between the real signals $X(t)$ and $Y(t)$. The frequency dependent reflection coefficient is defined as the ratio of the seaward to the shoreward flux. Integrating fluxes over the infragravity frequencies yielded estimates of the bulk-infragravity reflection coefficient, $R^2 = F_L^- / F_L^+$, where F_L^\pm is the linear flux integrated over the infragravity frequencies. Sheremet et al. (2002) estimated that errors in F_L^\pm and R^2 , because of the normal incidence assumption, were smaller than 20%.

INFRAGRAVITY-WAVE DYNAMICS

Analyses of the infragravity-wave dynamics were based on one-hour long model results – which is longer than the 34 minute measured signals. All the (wavenumber) frequency (co)spectra in this section were computed with thirty degrees of freedom.

In the nearshore, the wave-flow field at the infragravity frequencies is composed of irrotational (e.g., leaky and edge waves) and rotational motions (e.g., eddies generated by wave-group forcing (e.g., MacMahan et al., 2004; Reniers et al., 2007), eddies generated by individual wave crests (Clark et al., 2012; Feddersen, 2014), and instabilities of the longshore current (e.g., Özkan-Haller and Kirby, 1999)). The simultaneous occurrence of these phenomena makes it impossible to identify the presence of leaky and edge waves without alongshore information. However, leaky and edge waves can be identified using the alongshore-wavenumber frequency spectra, based on their alongshore wavenumber (κ [m^{-1}]) and frequency combination. In this study, alongshore-wavenumber frequency spectra $E(\kappa, f)$ were computed for surface elevation and velocity signals, which covered the whole numerical domain in y -direction.

To quantify the contribution of leaky and edge waves to the local infragravity-wave field, we partitioned the energy in the $E(\kappa, f)$ into two bands: a leaky-wave band and an edge-wave band. A free infragravity-wave was considered leaky if its $\kappa - f$ combination can exist at the numerical wavemaker, that is, if $\kappa_1 < \pm f / \sqrt{gd_0}$, where d_0 represents the still water depth at the wavemaker. If the κ is larger than this limit, the free wave cannot exist at the offshore boundary and is trapped shoreward of the wavemaker. At relatively large κ , gravity waves do not exist and only rotational motions occur. To exclude these rotational motions from this analysis, the lower limit of the edge-wave band corresponded to a zero-mode edge wave on a plane beach (e.g., Howd et al., 1991), $\kappa_0 = \pm f^2 / (g\beta)$, where $\beta (= 1/100)$ is the local beach slope. Although this analysis does not differentiate between (incoming) bound and free infragravity-waves, it does indicate the relative importance of leaky versus trapped motions, because the alongshore wavenumber of a shoreward-directed bound infragravity-wave dictates whether its reflection will be trapped nearshore (assuming an alongshore uniform beach). The contributions of both bands were quantified at each cross-shore location by integrating the energies over their

respective bands,

$$E_{\text{ig,leaky}}(x) = \int_{f_{\text{lo}}}^{f_{\text{hi}}} \int_{-\kappa_1 - \Delta\kappa_1}^{\kappa_1 + \Delta\kappa_1} E(\kappa, f, x) d\kappa df, \quad (4.7)$$

$$E_{\text{ig,edge}}(x) = \int_{f_{\text{lo}}}^{f_{\text{hi}}} \int_{-\kappa_0 - \Delta\kappa_0}^{\kappa_0 + \Delta\kappa_0} E(\kappa, f, x) d\kappa df - E_{\text{ig,leaky}}(x), \quad (4.8)$$

in which the frequency limits follow from the infragravity frequency band ($f_{\text{lo}} = 0.005\text{Hz}$, and $f_{\text{hi}} = f_p/2$). The constant wavenumber offsets, $\Delta\kappa_1$, and $\Delta\kappa_0$, account for the variation of κ in a frequency bin. Following Oltman-Shay and Guza (1987), these offsets were estimated as the derivative of their respective dispersion relationship, $\Delta\kappa_1 = \Delta f / \sqrt{gd_0}$, and $\Delta\kappa_0 = 2f\Delta f / (g\beta)$, respectively.

Besides estimating the energies in the leaky and edge wave band, we estimated the contribution of bar-trapped edge waves to the local infragravity-wave field. Theoretically, edge waves are trapped at a bar if $f\sqrt{gd_{\text{trough}}^*} \leq \kappa \leq f\sqrt{gd_{\text{bar}}^*}$ (e.g., Bryan et al., 1998), where d_{bar}^* and d_{trough}^* indicate the effective depth at the bar and in the trough, respectively, which includes the effect of the alongshore current (Howd et al., 1992). Furthermore, they are characterised by a relatively large amplitude near a local minima in the depth profile (e.g., bars), and an exponentially decreasing amplitude away from this location. Based on these characteristics, the contribution of bar-trapped edge waves to the local infragravity-wave field was estimated by integrating the energies over the $\kappa - f$ combinations that satisfy the theoretical limits (including wavenumber offsets), but only if its energy is amplified relative to the shore. The amplification was computed as,

$$A(\kappa, f, x) = \frac{E(\kappa, f, x)}{E^{\text{ref}}(\kappa, f)}, \quad (4.9)$$

where $E^{\text{ref}}(\kappa, f)$ is a reference spectrum, which was taken at an alongshore transect near the shoreline ($d \approx 1\text{m}$). Energies were considered to represent bar-trapped edge waves if $A(\kappa, f, x) \geq 5$, to exclude relative small amplifications from the estimation.

The wavenumber frequency spectra of the surface elevation signal were decomposed in shoreward directed and seaward directed contributions using the technique proposed by Sheremet et al. (2005). This technique, based on WKB theory (which assumes small depth variations), yields estimates of the linear energy fluxes in a $\kappa - f$ region that is bounded by the shallow-water phase velocity ($\kappa = f / \sqrt{gd}$). These fluxes are defined as,

$$F_L^\pm(\kappa, f) = \frac{d}{4} \left(\frac{|c_x|}{d} C_{\kappa, f}(\zeta, \zeta) \pm 2C_{\kappa, f}(\zeta, u) + \frac{d}{|c_x|} C_{\kappa, f}(u, u) \right), \quad (4.10)$$

where c_x is the cross-shore component of the shallow-water phase velocity, and $C_{\kappa, f}(X, Y)$ is the co-spectrum in $\kappa - f$ space between the real signals $X(y, t)$ and $Y(y, t)$.

To analyse the relationship between the wave groups and the infragravity waves, we evaluated the steady, weakly nonlinear infragravity energy balance, following Henderson

et al. (2006). Here, we used an extension of the original method, removing the assumptions of (near) shore-normal short-wave propagation and alongshore uniformity,

$$\frac{\partial F_x(f)}{\partial x} + \frac{\partial F_y(f)}{\partial y} = W(f) - D_b(f), \quad (4.11)$$

where $F_x(f)$ and $F_y(f)$ are the cross-shore and alongshore directed energy flux, $D_b(f)$ is a dissipation term representing bottom friction, and $W(f)$ represents a nonlinear energy transfer at infragravity frequency f . The energy fluxes are a combination of a linear $F_L(f)$ and a nonlinear contribution $F_{NL}(f)$,

$$F_x(f) = g d C_f (\tilde{\zeta}, \tilde{u}) + g C_f (\tilde{\zeta}, M) \equiv F_{L,x}(f) + F_{NL,x}(f), \quad (4.12)$$

$$F_y(f) = g d C_f (\tilde{\zeta}, \tilde{v}) + g C_f (\tilde{\zeta}, N) \equiv F_{L,y}(f) + F_{NL,y}(f), \quad (4.13)$$

where $M (= \zeta' u')$, and $N (= \zeta' v')$ represent mass fluxes in x and y direction, respectively.

The nonlinear transfer term is defined as,

$$W(f) = -C_f \left(\tilde{u}, \frac{\partial S_{xx}}{\partial x} \right) - C_f \left(\tilde{u}, \frac{\partial S_{xy}}{\partial y} \right) - C_f \left(\tilde{v}, \frac{\partial S_{xy}}{\partial x} \right) - C_f \left(\tilde{v}, \frac{\partial S_{yy}}{\partial y} \right), \quad (4.14)$$

where $S_{xx} (= du'u' + \frac{1}{2} g \zeta' \zeta')$, $S_{xy} (= du'v')$, and $S_{yy} (= dv'v' + \frac{1}{2} g \zeta' \zeta')$ are the radiation stress terms. An alternative, but mathematically equivalent, expression for the nonlinear energy transfer term can be derived by rewriting the gradient terms (e.g., $\tilde{u} \frac{\partial S_{xx}}{\partial x} = \frac{\partial \tilde{u} S_{xx}}{\partial x} - \frac{\partial \tilde{u}}{\partial x} S_{xx}$). Although these terms are mathematically equivalent, differences may arise when evaluating the derivatives if the spacing between two discrete points is too large (e.g., Péquignot et al., 2014). A sensitivity study indicated that a 5m output spacing in x direction, and a 20m output spacing in y direction yielded similar results for both expressions, which was therefore chosen to be the output resolution (see §4.2). The gradients were evaluated using central differences.

Bulk flux and transfer terms were computed by integrating the terms over the infragravity frequency band. In this study, we only considered the bulk effect of the dissipation due to bottom friction, which was computed following (Henderson and Bowen, 2002),

$$D_b = c_f \left(\overline{u^2 + v^2} \right)^{\frac{1}{2}} \overline{\tilde{u}^2 + \tilde{v}^2}, \quad (4.15)$$

where the overbar denotes an averaging operation. This expression results from a bottom stress parametrisation that is equivalent to the bottom stress formulation used in the SWASH model. To evaluate this term consistent with the simulations, the dimensional friction coefficient c_f was computed following the Manning-Strickler formulation used in the simulations (see §4.2).

In this work, we present the infragravity energy balance throughout the nearshore in terms of alongshore-averaged bulk parameters, and frequency varying parameters. These terms were first computed along each cross-shore transect, excluding the extended part of the numerical domain, after which they were averaged in alongshore direction. For all conditions considered in this study, contributions of rotational motions to the energies at the infragravity frequencies (computed following Lippmann et al., 1999) did not exceed 55%.

4.3. RESULTS: MODEL DATA COMPARISON

Before analysing the infragravity wave dynamics based on the model results, we assessed the ability of SWASH to produce a wave field that is representative for the natural conditions at the field site. For this purpose, we compared predictions and observations of six bulk parameters, and three frequency-dependent wave parameters.

BULK PARAMETERS

First, we discuss comparisons between predictions and observations of six bulk parameters: the significant short-wave height ($H_{m_0,s}$), the significant infragravity-wave height ($H_{m_0,ig}$), the energy weighted mean short-wave angle ($\bar{\theta}$), the energy weighted short-wave directional spread ($\bar{\sigma}_\theta$), the alongshore current (V), and the bulk infragravity reflection coefficient (R^2).

Model predicted $H_{m_0,s}$ agreed with the observations, which is illustrated by the results of the four wave conditions shown in Fig. 4.3a-d. The results of these wave conditions were representative for all conditions, as illustrated by the error and skill measures (Table 4.2). Predicted $H_{m_0,ig}$ were of similar order of magnitude as the observations (Table 4.2), although $H_{m_0,ig}$ was generally over predicted at the gauge locations (Fig. 4.3e-h). For the four wave conditions shown in Fig. 4.3e-h, the predicted $H_{m_0,ig}$ had a striking cross-shore evolution: a local maximum occurred near the crest of the outer bar ($x \approx 450\text{m}$), and near the crest of the inner bar ($x \approx 200\text{m}$). Such patterns were also observed for the moderate to severe wave conditions of the second storm event (not shown). These maxima were most pronounced for the low energetic wave conditions (Fig. 4.3g-h). We will return to these features in §4.4.

Table 4.2: Root Mean Square Error (RMSE) and Skill factor of the significant short-wave height ($H_{m_0,s}$) and infragravity wave height ($H_{m_0,ig}$), computed for all gauges with available surface-elevation measurements, and the bulk-infragravity reflection coefficient (R^2), computed for all gauges with available surface-elevation and velocity measurements. Results are listed for each wave condition, and averaged over all conditions. For quantity Q , the RMSE was computed as, $\text{RMSE} = \sqrt{\langle(Q_p - Q_o)^2\rangle}$, and the skill factor was computed as, $\text{Skill} = 1 - \sqrt{\langle(Q_p - Q_o)^2\rangle/\langle Q_o^2\rangle}$, where $\langle \dots \rangle$ indicates averaging over the available gauges, and subscript o and p indicate observed and predicted values, respectively.

	E1a	E1b	E1c	E2a	E2b	E2c	Average
RMSE $H_{m_0,s}$	0.04	0.13	0.27	0.14	0.21	0.08	0.14
RMSE $H_{m_0,ig}$	0.06	0.10	0.09	0.05	0.07	0.09	0.08
RMSE $\bar{\theta}$	2.49	1.22	4.98	0.78	2.88	2.67	2.50
RMSE $\bar{\sigma}_\theta$	2.82	3.73	4.66	5.27	2.40	5.56	4.07
RMSE V	0.17	0.11	0.03	0.05	0.04	0.07	0.08
RMSE R^2	0.03	0.06	0.20	0.12	0.06	0.08	0.09
Skill $H_{m_0,s}$	0.95	0.91	0.82	0.86	0.81	0.96	0.88
Skill $H_{m_0,ig}$	0.60	0.61	0.81	0.72	0.69	0.77	0.70
Skill $\bar{\theta}$	0.56	0.68	-0.40	0.72	0.13	0.23	0.32
Skill $\bar{\sigma}_\theta$	0.72	0.80	0.72	0.95	0.92	0.84	0.83
Skill V	0.37	0.83	0.91	0.71	0.72	0.52	0.68
Skill R^2	0.91	0.87	0.46	0.61	0.73	0.83	0.74

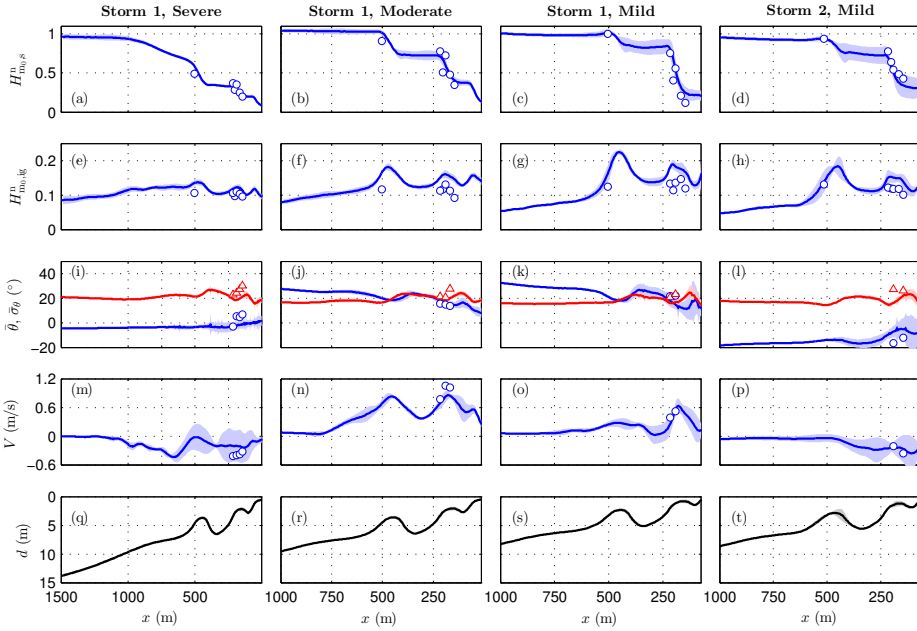


Figure 4.3: Measured (symbols) and predicted (alongshore mean, lines; alongshore standard deviation, shade) normalised significant short wave height $H_{m0,s}^n$ (panel a-d); normalised significant infragravity-wave height $H_{m0,ig}^n$ (panel e-h); mean short-wave direction $\bar{\theta}$ (blue line and blue circles), and short-wave directional spread $\bar{\sigma}_\theta$ (red line and red triangles) (panel i-l); and longshore current V (panel m-p) for four wave conditions. The wave heights were normalised with the target wave height (see Table 4.1). Panel q-t shows the depth (alongshore mean, lines; alongshore standard deviation, grey shade).

Differences between the observed and measured bulk short-wave direction ($\bar{\theta}$) were on average 2.5 degrees (Fig. 4.3i-l and Table 4.2). Although the absolute error was only a few degrees, predicted $\bar{\theta}$ had a relatively low skill. The skill was even negative for the severe condition of the first storm, for which predicted and observed $\bar{\theta}$ were of different sign at some sensors (see Fig. 4.3i). Errors were partly due to inaccuracies in $\bar{\theta}$ observations, which were of $\mathcal{O}(1^\circ)$, resulting in relatively large measurement inaccuracies in case of near-shore normal mean-wave angles (e.g., Fig 4.3i). Measurements of the directional spreading $\bar{\sigma}_\theta$ were more reliable than $\bar{\theta}$. For all conditions, predicted $\bar{\sigma}_\theta$ were smaller than the observations, with an average error of 4 degrees, which corresponds to an average skill of 0.83 (Table 4.2). These over predictions of $\bar{\sigma}_\theta$ likely contributed to the over predictions of $H_{m0,ig}$, as the directional spreading of a short-wave field significantly reduces the bound wave response (e.g., Okihiro et al., 1992).

The direction of the predicted alongshore current V was always consistent with the observations, although errors in magnitude were significant (on average 0.08m/s, corresponding to a skill of 0.68). Discrepancies were partly caused by the absence of tidal and wind driven currents in the simulations, because their combined contribution to the alongshore momentum balance in the bar-trough region was equal to approximately 40% of the wave forcing (Ruessink et al., 2001). Furthermore, the coarse spatial reso-

Table 4.3: Measured and predicted bulk-infragravity reflection coefficients (R^2) at gauge 1b.

	E1a	E1b	E1c	E2a	E2b	E2c
Measured	0.37	0.37	0.33	0.33	0.25	0.41
Predicted	0.33	0.40	0.14	0.25	0.17	0.39

lution of the velocity sensors complicates a comparison of the spatial structure of V , although the model appears to capture the location of significant alongshore currents near the inner bar for conditions with relatively large incident wave angles (Fig. 4.3n-o).

The observed bulk-infragravity reflection coefficients (R^2) indicate that the shoreward directed linear flux component was larger than the seaward directed component at gauge 1b (Table 4.3), which was the most shoreward located gauge where velocity measurements were available for all wave conditions. At this nearshore location, the nonlinear flux contribution was typically small, and the linear flux dominated the total flux, as exemplified by the model results (see Fig. 4.6). The small R^2 values therefore suggest that a significant part of the infragravity wave energy was dissipated and/or trapped shoreward of gauge 1b. SWASH reproduced the relatively low R^2 observations with an average skill of 0.74, but typically predicted lower R^2 values compared to the measurements (Table 4.2-4.3). This indicates that the model over estimated the nearshore infragravity dissipation and/or trapping.

SPECTRAL PARAMETERS

Next, we discuss comparisons of predictions and observations of the frequency variation of the reflection coefficient $R^2(f)$, and the frequency spectra of the surface elevation, u -velocity component and v -velocity component. At the inner bar, the observed $R^2(f)$ showed a distinct frequency dependent behaviour, consistent with a previous study at this field site (De Bakker et al., 2014). For all conditions, $R^2(f)$ was near zero for relatively high frequencies, whereas at lower frequencies $R^2(f)$ indicated near perfect reflections (Fig. 4.5). The predicted $R^2(f)$ show a similar frequency dependency, although predicted values were typically smaller than the observations, consistent with the bulk R^2 (Table 4.3). At the most offshore located gauge (7a or 7d), the predicted spectral shape approximately represented the measurements at the dominant short-wave frequencies (Fig. 4.4a, c, e, and g). Near the inner bar, short-wave energies were lower due to wave breaking, and the model qualitatively reproduced the spectral shape for most conditions (Fig. 4.4d, f, h), except for the severe condition of the first storm (Fig. 4.4b). At the infragravity frequencies, spectra were relatively broad due to the limited length of the signals (34 min), which complicates a detailed comparison. Infragravity energies were typically over predicted, as previously observed for $H_{m0,ig}$. For some conditions, the predicted spectral shape at the infragravity frequencies was broader compared to the measurements (e.g., Fig. 4.4a-b), whereas for other conditions the predicted spectral shape resembled the measured shape (e.g., Fig. 4.4c-d). Differences at the infragravity frequencies were typically larger if the prediction of the short-wave spectral shape was relatively poor (e.g., Fig. 4.4a-b). The spectral shape of the observed u and v -velocity spectra is similar to the surface elevation spectra at most frequencies, except at relatively low infragravity frequencies. At these lower frequencies, energies are relatively large compared to the

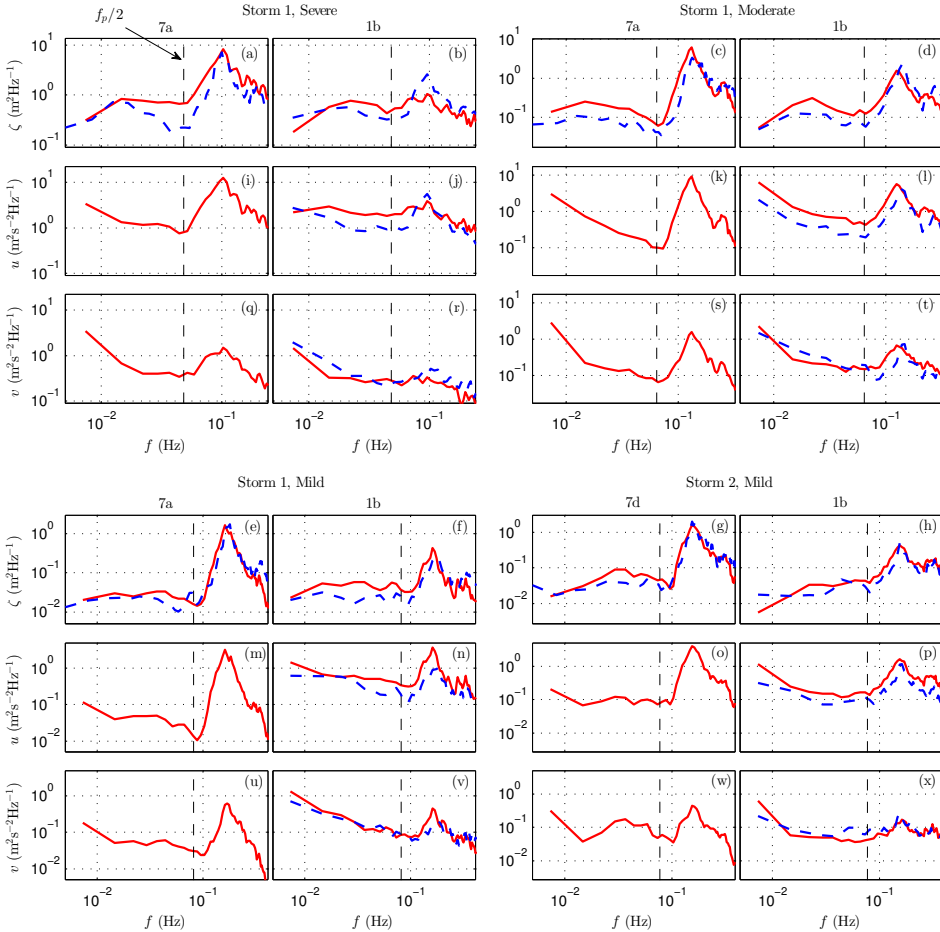


Figure 4.4: Measured (dashed blue line) and predicted (full red line) frequency spectra of the surface elevation, u -velocity component, and v -velocity component at the most offshore located operating gauge (Storm 1, 7a; Storm 2, 7d) and at gauge 1b (located at the inner bar), for four wave conditions.

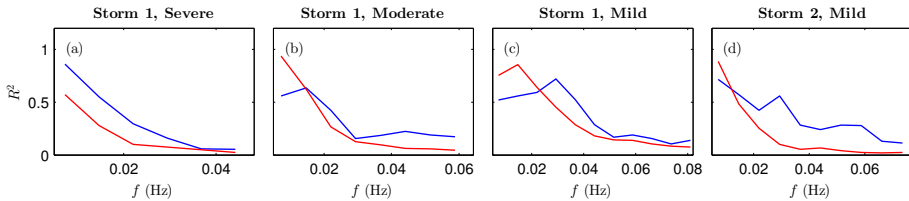


Figure 4.5: Measured (blue line) and predicted (red line) infragravity reflection coefficient $R^2(f)$ at gauge 1b (located at the inner bar), for four wave conditions.

higher frequencies, which is not reflected in the surface elevation spectra. This is likely due to the presence of rotational motions (e.g., eddies), which have a small contribution to the surface elevation spectra (e.g., Lippmann et al., 1999). The predicted spectral shape of both velocity components is similar to the observations, although energies are generally over predicted (e.g., Fig. 4.4l and n).

The above mode-data comparison showed that the predicted directional short-wave field reasonably resembled the measured short-wave field, especially given that SWASH was forced based on bulk wave parameters measured by an offshore wave buoy (see §4.2 and Appendix 4.C). The reasonable skill of the predicted infragravity parameters suggests that the predicted infragravity wave field was representative for the measured infragravity-wave field. We conclude that the predicted wave field was representative for the wave conditions that were measured during the field experiment. This suggests that SWASH can be used to study the processes governing the nearshore infragravity-wave evolution.

4

4.4. RESULTS: INFRAGRAVITY WAVE DYNAMICS

In this section, we examine the variation of the infragravity energy in the nearshore, and identify the contributions of (bar-trapped) edge-waves and leaky waves (§4.4). Next, we evaluate the terms that influence the nearshore infragravity energy balance (§4.4), including the energy exchange between the short and infragravity waves, and the nearshore dissipation of infragravity waves.

INFRAGRAVITY ENERGY IN THE NEARSHORE

The cross-shore component of the energy flux (F_x) varied significantly throughout the nearshore for all conditions (Fig. 4.6). Seaward of the outer bar, F_x abruptly increased for mild wave conditions, whereas the increase was more gradual for more energetic conditions. For all conditions, the linear flux $F_{L,x}$ was positive throughout the domain, had a larger magnitude than the nonlinear flux $F_{NL,x}$, and had a similar cross-shore pattern as F_x . In contrast to the positive linear flux, $F_{NL,x}$ was negative and generally significant seaward of the surf zone, consistent with the presence of bound infragravity waves (e.g., Péquignet et al., 2014). For all but the severe condition of the first storm, $F_{NL,x}$ peaked near the outer and inner bar, and decreased shoreward of both bars. For the severe condition of the first storm, $F_{NL,x}$ peaked at $x \approx 1000\text{m}$ (the approximate location of initial wave breaking, see Fig. 4.3a), and became approximately zero shoreward of the outer bar. For all conditions, the patterns suggest that bound wave contributions decreased when short waves were breaking, which typically occurred near the crest of the outer and inner bar (except for the severe condition of the first storm).

For the mild condition of the first storm event (Fig. 4.6a), the total flux $F (= F_x + F_y)$ was approximately twice as large as F_x up to the outer bar, indicating that the along-shore flux component F_y was of similar magnitude as F_x . Shoreward of the outer bar, the relative contribution of F_y decreased, and near the shoreline F_x dominated the total energy flux. During the first storm event, the overall contribution of F_y decreased for more energetic conditions, and F_x explained most of the total flux. This is consistent with decreasing incident mean-wave angles for increasingly energetic conditions (Table

4.1). For the mild condition of the second storm event and the severe conditions of both storm events, the total flux was smaller than F_x , which indicates that the F_y was negative (Fig. 4.6c, d and f). We associate these negative F_y values with the dominance of southward over northward propagating infragravity motions, consistent with the mean angle of wave propagation (Table 4.1).

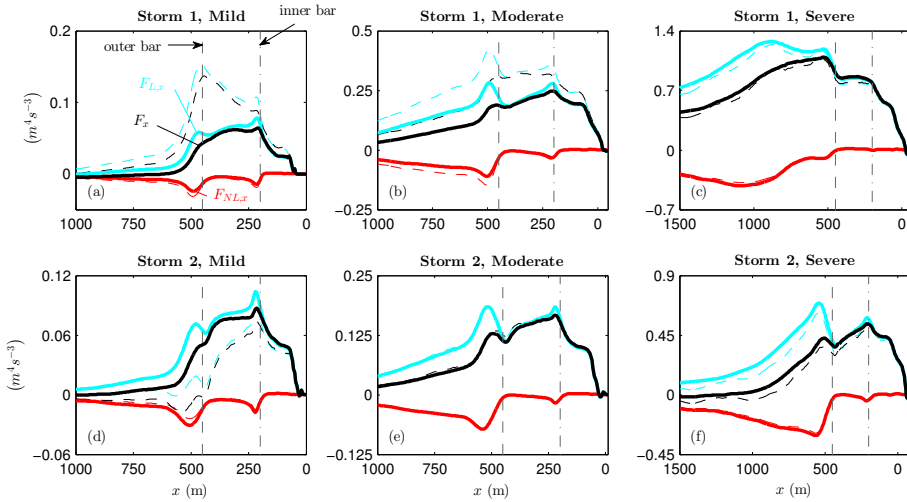


Figure 4.6: Cross-shore variation of the cross-shore component of the energy flux $F_x (= F_{L,x} + F_{NL,x})$ (black line), linear energy flux $F_{L,x}$ (blue line), and nonlinear energy flux $F_{NL,x}$ (red line), integrated over the infragravity band, for the mild (panel a and d), moderate (panel b and e), and severe (panel c and f) wave condition of the first (panel a-c) and second (panel d-f) storm event. The thin dashed lines represent the total energy flux contributions, for example, $F (= F_{L,x} + F_{NL,x} + F_{L,y} + F_{NL,y})$. In all panels, the thin vertical lines indicate the approximate location of the outer (dashed line) and inner bar (dash dotted line).

The occasional occurrence of significant alongshore directed fluxes near the outer bar suggests that a significant part of the infragravity-wave motion was orientated in alongshore direction, possibly explained by the presence of edge waves. To identify if edge-waves indeed contributed to the nearshore infragravity wave field, we computed alongshore-wavenumber frequency spectra at various cross-shore locations. Furthermore, edge-wave dispersion curves were computed numerically following the model of Howd et al. (1992), based on the (alongshore averaged) bathymetry profile, accounting for the tidal level, and including the influence of the alongshore current. At the outer bar, for the mild wave condition of the first storm event, the surface-elevation spectrum shows a distinct streak of energy at positive κ values, extending from the lower to the higher infragravity frequencies (Fig. 4.7a). The energies at these $\kappa - f$ combinations were significantly larger compared to their values near the shoreline (i.e., $A(\kappa, f) \gg 1$, see Fig. 4.7d). The $\kappa - f$ combinations of these significant amplifications qualitatively agree with numerical predictions of bar-trapped edge wave modes. These results suggest that edge waves were trapped at the outer bar for this particular wave condition. Most energies were located at positive κ values, which indicates that northward directed

waves dominated over southward directed waves, which is consistent with the incident mean-wave direction (Table 4.1).

The alongshore length of the domain restricts the possible wave modes, as the alongshore domain length is an integer multiple of the alongshore wave length (see Appendix 4.A). This can be observed in Fig. 4.7, as the resolution in κ space is equal to the inverse of the alongshore domain length. Although this restricted the possible infragravity wave modes, we expect that this did not significantly affect the results as the κ resolution was small ($\Delta\kappa = 1/1300\text{m}^{-1}$), likely resulting in a sufficient number of possible wave modes for the majority of the infragravity frequencies.

Similar to the mild wave condition, the spectra of the moderate and severe wave condition of the first storm event show a distinct energy streak at both positive and negative κ values (Fig. 4.7b and c). Again, these streaks were amplified relative to the shore, and their $\kappa - f$ combinations agree with theoretical bar-trapped modes (Fig. 4.7e and f). However, compared to the mild wave condition, energies were more spread in $\kappa - f$ space (especially for the severe condition).

For all wave conditions of the first storm event, surface elevation spectra computed at the inner bar showed no sign of significant (bar-trapped) edge waves (not shown). This indicates that the motions near the inner bar and near the shoreline were dominated by leaky waves. Results of the second storm event were qualitatively similar to the results of the first storm event. For all three conditions of the second storm event, edge waves were observed at the outer bar, whereas edge waves were not observed at the inner bar and near the shoreline.

To quantify the contributions of the edge wave and the leaky-wave motions, Fig. 4.8 shows the cross-shore variation of the relative contribution (in %) of the edge-wave band and the leaky-wave band to the total energy of the surface elevation spectra at the infragravity frequencies (which add up to approximately 100%). For all conditions, relative contributions of the leaky and edge-wave band were roughly constant throughout the domain, except near the outer bar where the contribution of the edge-wave band generally increased significantly (except for the severe condition of the first storm event). This local increase in the edge-wave contribution was most significant for the moderate wave conditions (especially for the first storm event), whereas it was smaller for the more energetic wave conditions. For increasingly energetic conditions, the overall contribution of the edge-wave band decreased, and the contribution of the leaky-wave band increased. This is likely related to the mean-wave angle, which decreased for increasingly energetic conditions (Table 4.1). Although the partitioning of the wavenumber spectra did not distinguish between bound and free waves, these results suggest that leaky waves dominated over edge waves throughout most of the nearshore, except near the outer bar.

The local increase of the edge-wave contribution at the outer bar coincides with significant contributions of bar-trapped edge waves. Bar-trapped motions were only energetic near the outer bar, and decreased significantly away from the bar. Their relative contribution was largest for the mild wave conditions, and was smaller for more energetic conditions (especially for the first storm event, Fig. 4.8c). These results suggest that bar-trapped edge waves were responsible for the increased contribution of the edge-wave band near the outer bar, and (partially) explain the local maximum of $H_{m0,ig}$ near the outer bar (as previously observed in §4.3, Fig. 4.3f-h). Although the relative contri-

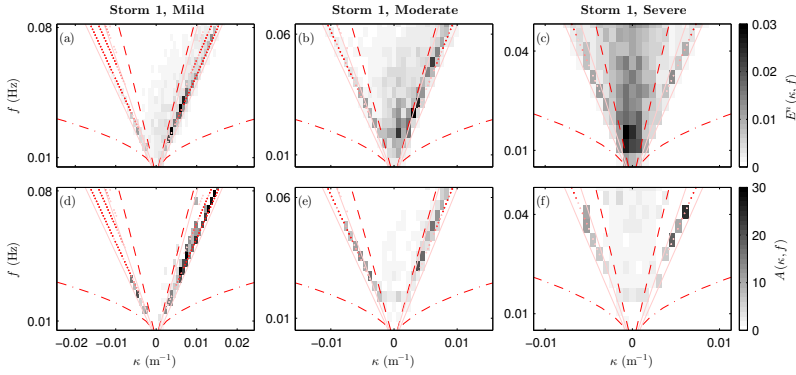


Figure 4.7: Normalised alongshore-wavenumber frequency spectra of the surface elevation signal $E^n(\kappa, f)$ at the outer bar ($x = 440\text{m}$) (panel a-c), and ratio $A(\kappa, f)$ of $E(\kappa, f)$ at $x = 440\text{m}$ to $E(\kappa, f)$ near the shoreline ($d \approx 1\text{m}$) (panel d-e) for the first storm event. The spectra in panel a-c are normalised with the energy integrated over the infragravity band. In panel d-f amplifications with values smaller than one are white. The dashed lines indicates the leaky wave cut-off, and the dash-dotted line indicates the lowest mode edge wave dispersion relationship (for a plane beach). The red markers represent numerical predictions of edge-wave modes trapped at the outer bar (following Howd et al., 1992), where the color intensity illustrates the magnitude of the amplification at the outer bar (where the minimum intensity corresponds to an amplification larger than one, and the maximum intensity represents an amplification equal to or larger than ten). The light red lines bound the theoretical region of edge waves that are trapped at the outer bar ($c = \sqrt{gd_{\text{bar}}^*}$, and $c = \sqrt{gd_{\text{trough}}^*}$, where d_{bar}^* and d_{trough}^* indicate the effective depth at the outer bar and in the trough, respectively).

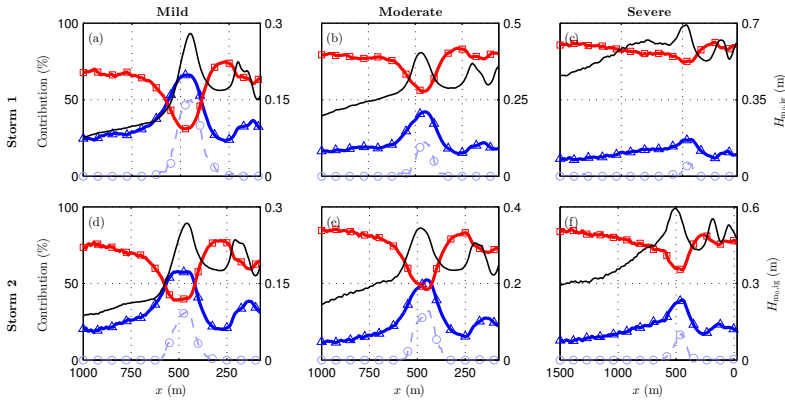


Figure 4.8: Cross-shore variation of the relative contribution to the surface elevation spectra (in %) of the leaky-wave band (thick red line with square markers), edge-wave band (thick blue line with triangular markers), and bar-trapped edge waves (dashed light-blue line with circle markers). For reference, the black line shows the significant infragravity wave-height (corresponding to the right vertical axis). The top three panels correspond to the mild (a), moderate (b), and severe (c) wave condition of the first storm event; and the bottom three panels correspond to the mild (d), moderate (e), and severe (f) of the second storm event.

bution of bar-trapped edge waves reduced for both events, the bar-trapped wave height ($H_{m_0,ig}^{bt}$) remained approximately constant for increasingly energetic conditions of the first storm event, and gradually increased during the second storm event (Table 4.4).

Table 4.4: Bar-trapped edge wave heights ($H_{m_0,ig}^{bt}$), and (for reference) infragravity-wave heights ($H_{m_0,ig}$) at the outer bar.

	E1a	E1b	E1c	E2a	E2b	E2c
$H_{m_0,ig}$	0.28	0.39	0.67	0.27	0.34	0.57
$H_{m_0,ig}^{bt}$	0.19	0.18	0.19	0.15	0.18	0.23

4

INFRAGRAVITY ENERGY BALANCE: FLUX GRADIENTS, NONLINEAR ENERGY TRANSFERS, AND DISSIPATION

To gain insight in the infragravity energy balance throughout the nearshore, Fig. 4.9a-f shows the cross-shore variation of the frequency integrated energy flux gradients ∂F ($= \partial F_x / \partial x + \partial F_y / \partial y$), nonlinear energy transfer term W , and the dissipation due to bottom friction D_b . For all conditions, $\partial F_y / \partial y$ was typically small compared to ∂F , indicating that $\partial F_x / \partial x$ dominated ∂F .

For both mild conditions, the significant flux gain near the outer bar was partially balanced by the nonlinear transfer term W (Fig. 4.9a and d). Further shoreward, the positive ∂F just seaward of the inner bar was not balanced by W , whereas W did explain part of the negative ∂F just shoreward of this location. Near the shoreline ($x < 150\text{m}$), the flux decreased significantly, which was not explained by W . However, the bottom dissipation term D_b did partially balance the negative ∂F near the shoreline. Qualitatively similar patterns were observed for the moderate conditions (Fig. 4.9a and e), and the severe condition of the second storm. The main difference between the more energetic and mild conditions occurred near the outer bar, where ∂F was locally negative, which was partially reflected in W . For the severe condition of the first storm, the flux increase seaward of the outer bar was more gradual and spread over the cross-shore, which was only partially explained by W (Fig. 4.9c). For all conditions, the S_{xy} contributions to W were insignificant. The S_{yy} contributions were only significant seaward of the inner bar, at locations where waves were breaking. This dominance of the S_{xx} contribution to the W term is similar to the findings of a previous numerical study at a gently sloping, single barred beach (Van Dongeren et al., 2003).

Next, we study how flux gradients and nonlinear transfer terms vary with frequency over the nearshore. Here, we focus on the results of the second storm event (Fig 4.9g-i), which were qualitatively representative for the first storm. Overall, the frequency dependent flux gradient $\partial F(f)$ mirrored the bulk term ∂F as patterns were relatively spread over the frequencies. However, variations in frequency were observed near the outer and inner bar. Near the outer bar, for all three conditions, flux gains were concentrated at higher frequencies, whereas flux losses were larger at lower frequencies (e.g., Fig 4.9h). Near the inner bar, both flux gains and losses were typically concentrated at higher frequencies (e.g., Fig 4.9g). At first sight, patterns of $W(f)$ appear to be qualitatively similar to $\partial F(f)$ patterns. However, similar to the bulk terms, $W(f)$ did not fully balance signifi-

cant flux gains near the outer bar, and did not explain the energy gains near the inner bar and the energy losses near the shoreline. Furthermore, $W(f)$ estimates suggest greater flux losses than $\partial F(f)$ near the outer bar.

Close to the shoreline ($x \leq 150\text{m}$), strong negative flux gradients occurred, whereas the nonlinear transfer term was near zero. The bottom friction term only balanced part of these significant flux losses, which suggests that another process contributed to these flux losses. These significant flux losses were supported by the low R^2 values, which also indicated significant nearshore energy losses (Table 4.3). However, the bulk reflection coefficients and the nearshore energy balance did not discriminate between the effect of wave trapping and actual dissipation. To study if topographic trapping affected the nearshore energy balance, Fig. 4.10a-c shows the shoreward and seaward directed x -component of the linear energy flux, in $\kappa - f$ space, near the shoreline ($d \approx 1\text{m}$), for

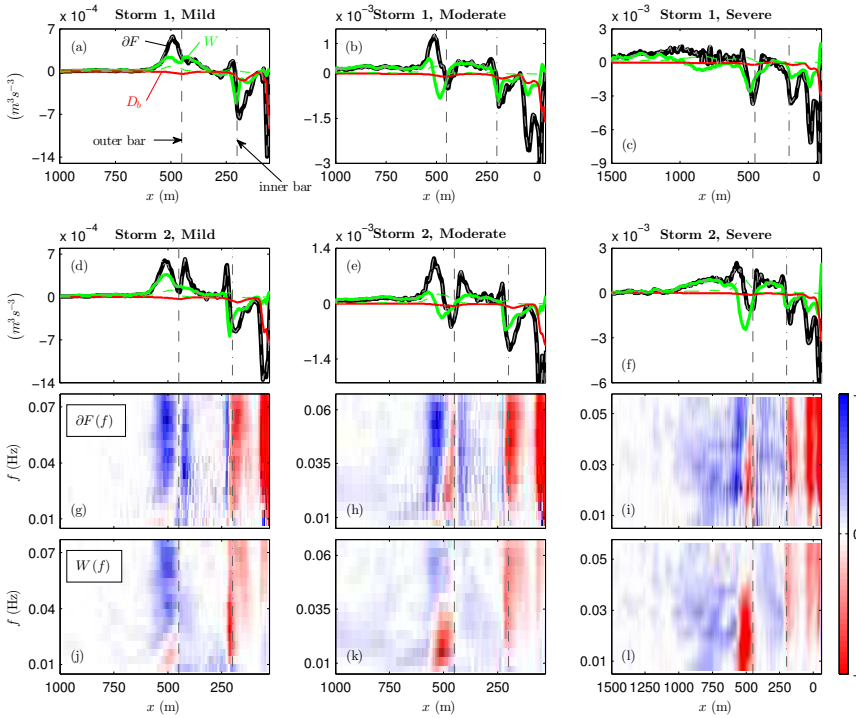


Figure 4.9: (Panel a-f) Cross-shore variation of the frequency integrated energy flux gradient $\partial F (= \partial F_x / \partial x + \partial F_y / \partial y)$ (black line); nonlinear transfer term W (green line); and bulk dissipation by bottom friction D_b (red line); for the mild (left panels), moderate (middle panels), and severe (right panels) condition of the first (panel a-c) and second (panel d-f) storm event. Panel g-l shows the corresponding cross-shore variation of $\partial F(f)$, and $W(f)$ for the second storm event. All frequency dependent terms in panel g-l are normalised by the maximum value of $\partial F(f)$, therefore, colors indicate the relative magnitude of these terms. In panel a-f, the thin gray dashed lines represents $\partial F_x / \partial x$ and the dashed green line represents the S_{yy} contribution to W . In all panels, the thin vertical lines indicate the approximate location of the outer (dashed line) and inner bar (dash dotted line).

the three conditions of the first storm event. This analysis excluded the nonlinear flux contribution, which was small near the shoreline (Fig. 4.6). For all three conditions, regions of significant seaward fluxes mirrored regions of significant shoreward fluxes. The seaward fluxes were smaller than the shoreward fluxes over the whole range of $\kappa-f$ combinations. Shoreward and seaward fluxes showed no sign of significant edge wave motions, which confirms that the wave motion near the shoreline was dominated by leaky-waves. This suggests that the small seaward fluxes were due to significant dissipation of shoreward propagating energy, rather than due to trapping shoreward of $d \approx 1\text{m}$. Similar results were observed for the three cases of the second storm event (not shown). This leaves infragravity wave breaking as possible dissipation mechanism that contributed to the significant infragravity energy losses. The magnitude of the predicted R^2 and its frequency dependence is similar to the findings of De Bakker et al. (2014), who conducted an observational study at the same field site. They linked these small shoreline reflections to the occurrence of infragravity-wave breaking, which they hypothesised to be the dominant dissipation mechanism. The consistency between this study and the results of De Bakker et al. (2014), and our observations that bottom friction only partially balanced

4

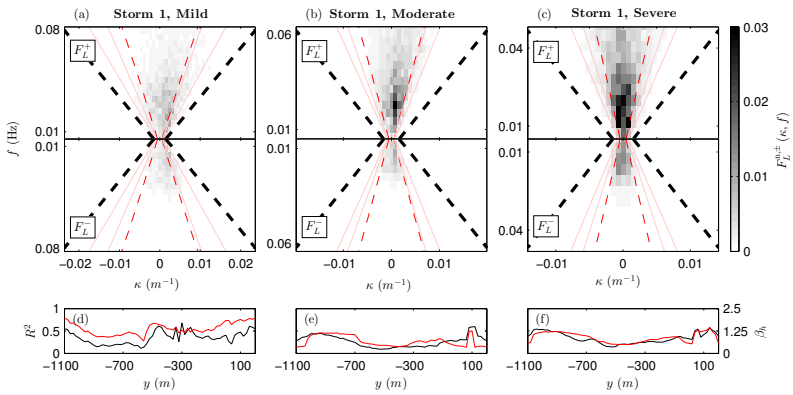


Figure 4.10: (Panel a-c) Incoming and outgoing cross-shore linear energy flux $F_L^\pm(\kappa, f)$ at $d \approx 1\text{m}$, normalised by the total incoming linear energy flux, for the mild (panel a), moderate (panel b), and severe wave condition (panel c) of the first storm event. The thick dashed line indicates the shallow-water phase velocity, which is the lower limit of validity of the WKB approximation. The dashed red lines indicate the leaky wave cut-off, and the light red lines bound the theoretical region of edge waves that are trapped at the outer bar ($c = \sqrt{gd_{\text{bar}}^*}$ and $c = \sqrt{gd_{\text{trough}}^*}$, where d_{bar}^* and d_{trough}^* indicate the effective depth at the outer bar and in the trough, respectively). (Panel d-f) Alongshore variation of the bulk reflection coefficient R^2 at the approximate location of the 0.5m depth contour (black line, left axis) and the normalised bed slope β_h (red line, right axis), for the mild (panel d), moderate (panel e), and severe condition (panel f) of the first storm event. The normalised bed slope is defined as $\beta_h = \left(\frac{\beta T}{2\pi \sqrt{\frac{g}{H^+}}} \right)$ (Van Dongeren et al., 2007), where H^+ is the height of an incoming infragravity wave, T is its period, and β is the bed slope. Here, the representative infragravity wave height and period were computed from the incoming linear energy flux ($H^+ = 4\sqrt{m_0^+}$, and $T = \left(\frac{m_1^+}{m_0^+} \right)^{-1}$, where m_0^+ and m_1^+ are the zeroth and first order moment of the incoming linear energy flux), and the bed slope was taken as the slope between the mean waterline and 0.5m depth.

the negative flux gradients near the shoreline, indicates that infragravity wave breaking likely contributed to the energy flux losses at the higher infragravity frequencies.

To study if the nearshore dissipation varied in alongshore direction, Fig. 4.10d-f shows the alongshore variation of the bulk infragravity reflection coefficient $R^2(y)$ for the conditions of the first storm event. $R^2(y)$ varied with a maximal factor of two along the coast. Largest reflections typically occurred near relative steep normalised bed slopes β_h , and alongshore variations of R^2 mirrored variations in β_h . These results of the first storm event are representative for the results of the second storm event. The typical qualitative agreement between R^2 and β_h patterns illustrates the strong relation between the infragravity reflections and the normalised bed slope (e.g., Van Dongeren et al., 2007; De Bakker et al., 2014).

4.5. DISCUSSION

This study highlighted that, seaward of the inner bar, nonlinear interactions between short and infragravity waves caused an infragravity energy growth. This growth is consistent with the findings of Henderson et al. (2006) near a bar at a gently sloping sandy beach. The nonlinear transfers reduced when waves were breaking, and even caused losses at lower infragravity frequencies. This negative work by short-waves was stronger and spread to higher frequencies for more intense breaking conditions. Near the inner bar, where short-waves were always breaking for the conditions considered in this study, short-waves caused negative work at most infragravity frequencies. Similar losses under breaking conditions were previously found based on numerical modelling at a plane beach (Ruju et al., 2012); and based on field observations at a dissipative beach (Guedes et al., 2013), and near the crest of a coral reef (Péquignet et al., 2014).

Near the shoreline, the significant infragravity energy losses were likely due to a combination of bottom friction and infragravity wave breaking. This adds to the findings of De Bakker et al. (2014) at the same field site, who suggested that bottom friction was at best a secondary dissipation mechanism, based on idealised numerical modelling of a low-sloping (1:80) plane beach for which infragravity reflections were small. For more reflective conditions, the numerical study of Rijnsdorp et al. (2014) showed that variations in the bottom friction coefficient significantly affected the nearshore dissipation of infragravity waves. This suggest that the effect of bottom friction is more important for reflective conditions, in line with the findings of this study.

Previous field studies at a barred beach, located near Duck (North Carolina, United States of America), found that bar-trapped edge waves existed at both infragravity and short-wave frequencies (Bryan and Bowen, 1996; Bryan et al., 1998; Bryan and Bowen, 1998). Bryan et al. (1998) further found that the bar-trapped waves were energetic for a range of wave conditions. Although these studies qualitatively showed that bar-trapped waves can be energetic, they did not quantify the contributions of the bar-trapped waves. Van Dongeren et al. (2003) did quantify the bar-trapped contributions at this field site, based on numerical predictions of the local infragravity-wave field. However, they only considered one wave condition, for which they found that bar-trapped edge waves accounted for 12% of the infragravity energy at the location of the bar. Compared to the Duck field site, the bar system at the Egmond field site was more pronounced (in terms of trough width, bar width, and bar height). A pronounced bar system is a favourable

condition for bar trapping (e.g., Bryan and Bowen, 1996). Indeed, we found that bar-trapped edge waves were energetic at the outer bar, where their contribution to the total infragravity energy ranged 10 – 50%.

4.6. CONCLUSIONS

This paper has presented the results of a comprehensive numerical study into the infragravity wave dynamics at a gently sloping, barred beach. To study the temporal and spatial variability of the infragravity-wave dynamics, the non-hydrostatic wave-flow model SWASH has been used to simulate three wave conditions (ranging from relatively mild to severe conditions) of two consecutive storm events. We found that the model produced a wave field that is representative of the natural conditions, given the reasonable model-data agreement for bulk and frequency dependent wave parameters (see Figures 4.3 to 4.4 and Table 4.2). This supports the model application to analyse the infragravity wave dynamics in more detail.

For all conditions, the infragravity wave field was dominated by leaky-wave motions throughout the nearshore, except near the outer bar. Here, bar-trapped edge waves were generally observed at the infragravity frequencies. The relative contribution of bar-trapped waves was most significant for the mild wave conditions, during which they explained up to 50% of the infragravity energy at the outer bar. For more energetic conditions, their relative contribution reduced, although it remained significant (ranging 10% – 40%). In contrast, their absolute contribution remained relatively constant during the first storm event, and gradually increased during the second storm event.

The significant growth of infragravity energy flux near the outer bar (especially for milder conditions) was partly explained by nonlinear energy transfers from short-waves. For increasingly energetic conditions, when short-wave breaking intensified at the outer bar, the nonlinear transfers reduced significantly and changed sign at lower infragravity frequencies, causing energy losses at these frequencies. Shoreward of the inner bar, infragravity waves primarily lost energy, which was due to a combination of nonlinear transfers, bottom friction, and infragravity-wave breaking. Nonlinear transfers caused some energy losses near the inner bar, where waves were breaking for all conditions. The strongest infragravity losses occurred near the shoreline, where nonlinear transfers ceased. These significant losses were likely caused by the combined effect of bottom friction and infragravity-wave breaking.

This study has exemplified the application of the SWASH model to study wave dynamics at field scales. The successful application of the model to analyse the infragravity wave dynamics has illustrated that the model can be a valuable tool to improve our understanding of complex nearshore wave dynamics, at scales not easily covered by in-situ observations.

APPENDICES

4.A. NUMERICAL WAVEMAKER¹

At the numerical wavemaker, the horizontal velocities normal to the boundary were prescribed based on a target variance density spectrum $E(f)$. The spectrum was sampled with N discrete frequencies from $f_p/2 < f \leq 3f_p$ with intervals of Δf . To avoid repetition of the wave signal, the frequency interval was set at $\Delta f = 1/T_s$, where T_s is the duration of the simulation (excluding spin up). Each frequency corresponds to a free long-crested wave with frequency f_n , wave number k_n , amplitude $a_n (= \sqrt{2\Delta f E_n})$, random phase ϕ_n , and direction θ_n . For each frequency, the wave direction was randomly drawn using a $\cos^m \theta$ distribution as a probability density function, which was centred at a mean wave angle $\bar{\theta}(f)$ that varied over the frequencies. At each frequency, the power m was computed from the directional spreading $\sigma_\theta(f)$. To ensure that waves are periodic in alongshore direction, θ_n was adjusted such that the alongshore wave number is an integer multiple of $2\pi/L_y$ (e.g., Van Dongeren et al., 2003), where L_y is the length of the domain in y direction. This approach prevents the standing wave issues of Johnson and Pattiaratchi (2006), because the resulting wave field is homogeneous (Miles and Funke, 1989), but requires a large number of wave components to generate a realistic directional wave field.

The (target) horizontal velocity signal u_t , including a second-order correction to account for incident bound infragravity waves (based on weakly non-linear wave theory), is given by

$$u_t(x, y, z, t) = \sum_{n=1}^N \hat{u}_n(z) \cos\left(2\pi f_n t + \phi_n + k_n (\cos(\theta_n)x + \sin(\theta_n)y)\right) + \sum_{n=1}^N \sum_{m=n+1}^N \hat{u}_{nm}(z) \cos\left(2\pi f_{nm} t + \phi_{nm} + k_{nm} (\cos(\theta_{nm})x + \sin(\theta_{nm})y)\right), \quad (4.A1)$$

where N is the number of free wave components. The first term on the right-hand side represents the linear free wave contributions, where $\hat{u}_n(z)$ is the vertically varying velocity amplitude of the n th wave component, which is related to the wave amplitude (a_n) by linear wave theory (e.g. Holthuijsen, 2007). The second term on the right-hand side of (4.A1) represents the bound infragravity-wave components, where $f_{nm} (= f_m - f_n)$ is the frequency, $\phi_{nm} = (\phi_n - \phi_m + \pi)$ is the phase, k_{nm} is the wave number, θ_{nm} is the direction, and $\hat{u}_{nm}(z)$ is the vertically varying velocity amplitude of a bound infragravity-wave component forced by the difference interaction between the n th and m th free wave component. The bound wave number is defined as

$$k_{nm} = \sqrt{k_n^2 + k_m^2 + 2k_n k_m \cos(\theta_n - \theta_m + \pi)}, \quad (4.A2)$$

¹Parts of this section are based on the description in Rijnsdorp et al. (2014) (see also §3.3).

and the bound wave angle as

$$\theta_{nm} = \arctan\left(\frac{k_m \sin\theta_m - k_n \sin\theta_n}{k_m \cos\theta_m - k_n \cos\theta_n}\right). \quad (4.A3)$$

In coastal waters, infragravity waves are essentially shallow-water waves for which the vertical variation of \hat{u}_{nm} is negligible. Therefore, $\hat{u}_{nm}(z)$ is approximated with a vertically constant velocity amplitude, which is computed based on the free wave components following Hasselmann (1962), see Appendix 4.B.

To absorb outgoing waves and to prevent re-reflections at the wave maker, the total velocity signal was defined as a superposition of the target (or incident) velocity signal and the velocity signal of reflected waves (u_r), $u = u_t + u_r$. To estimate u_r , outgoing waves were assumed to be shallow water waves propagating perpendicular to the boundary. In this manner u_r was computed as, following mass conservation in combination with the assumption that outgoing waves are progressive and of constant form,

$$u_r = \frac{c}{d} \zeta_r, \quad (4.A4)$$

where $c (= \sqrt{gd})$ is the phase velocity of a shallow water wave, and ζ_r is surface elevation of the outgoing waves, which was detected as the difference between the target surface elevation and the instantaneous surface elevation computed by SWASH.

In this wavemaker implementation, velocities are directly imposed at the offshore boundary, in contrast with the approach typically used in Boussinesq models, which combines a source function to generate waves, and a sponge layer to absorb outgoing waves (e.g., Wei et al., 1999; Chen et al., 2003; Feddersen et al., 2011). The advantage of the approach used here is that higher order wave theories can be implemented relatively straightforward to accurately generate nonlinear waves, and a domain extension to accommodate the sponge layer and source region is not required (reducing computational costs). On the other hand, the approach to absorb outgoing waves (4.A4) is primarily effective for (nearly) shore normal propagating shallow water waves, whereas it is (weakly) reflective for directional, dispersive waves. In contrast, the sponge layer approach is very effective to damp outgoing waves. However, at low sloping beaches studied in this paper, the reflection of short-waves is typically small. Furthermore, the predicted infragravity reflections were typically small (see §4.3 and 4.4). Although the wavemaker possibly reflected some outgoing wave energy, we did not notice adverse effects of re-reflections at the wavemaker.

4.B. SECOND-ORDER BOUNDARY CONDITION

The second-order boundary condition implemented in SWASH is based on weakly nonlinear second-order finite depth wave theory (Hasselmann, 1962). Herein, the wave field is composed of first-order waves, the free wave response, and a second-order correction, which represents the bound sub and super harmonics. In this study, super harmonics are excluded and the second-order correction only accounts for the sub harmonics (i.e., bound infragravity-waves). The amplitude of a bound infragravity-wave, forced by two free wave components with frequency f_n and f_m , is given by (Hasselmann, 1962)

$$a_{nm} = D_{nm} a_n a_m, \quad (4.B1)$$

where a_n and a_m are the amplitudes of the respective free wave components and D_{nm} is the interaction coefficient. For directionally spread waves, the interaction coefficient is given by

$$D_{nm} = \frac{gk_n k_m}{2\omega_n \omega_m} \cos(\theta_n - \theta_m + \pi) + \frac{\omega_n^2 - \omega_n \omega_m + \omega_m^2}{2g} - C \frac{g(\omega_n - \omega_m)}{\omega_n \omega_m [gk_{nm} \tanh(k_{nm}d) - (\omega_n - \omega_m)^2]}, \quad (4.B2)$$

where $\omega (= 2\pi f)$ is the radial frequency, and coefficient C is defined as

$$C = (\omega_n - \omega_m) \left(\frac{(\omega_n \omega_m)^2}{g^2} - k_n k_m \cos(\theta_n - \theta_m + \pi) \right) - \frac{1}{2} \left(\frac{\omega_n k_m^2}{\cosh^2(k_m d)} - \frac{\omega_m k_n^2}{\cosh^2(k_n d)} \right). \quad (4.B3)$$

The vertically constant velocity amplitude \hat{u}_{nm} follows from mass conservation in combination with the assumption that bound infragravity-waves are progressive and of constant form, $\hat{u}_{nm} = a_{nm} c_g / d$, where $c_g (= 2\pi f_{nm} / k_{nm})$ is the group velocity.

4.C. TARGET WAVE CONDITIONS

The target wave conditions at the numerical wave maker ($E(f)$, $\bar{\theta}$, and σ_θ) were computed using SWAN (version 40.91A), including all deep and shallow wave physics (in default settings). The western boundary in SWAN was taken as a straight line from south to north through the buoy (see Fig. 4.2). At this boundary the incident wave conditions were considered to be uniform and were given by a JONSWAP shape spectrum, based on the deep-water wave parameters ($H_{m0,d}$, $T_{p,d}$ and $\bar{\theta}_d$), with a $\cos^m \theta$ directional distribution. Unfortunately, no measurements of the directional spreading were available, therefore, we assumed $\sigma_{\theta,d} = 30^\circ$ for all frequencies. No wave information was available at the northern and southern SWAN boundaries, therefore, no incident waves were forced at these boundaries. Although this introduced errors in the region near these boundaries, these local errors did not affect the predicted target wave conditions, because the lateral boundaries were located sufficiently far away from the region of interest. A spatially constant wind field was forced based on the wind measurements at gauge 7a. The frequency range in the SWAN simulations was $0.6f_p - 3f_p$ with a resolution of $\Delta f \approx 0.1f$ and the spectral range was $0 - 360^\circ$ with a resolution of $\Delta\theta = 10^\circ$. The SWAN predicted target wave conditions ($E(f)$, $\theta(f)$, and $\sigma_\theta(f)$) were output in the center of the SWASH wavemaker (see Fig. 4.2), see Table 4.1 for an overview of the target bulk wave parameters.

5

SIMULATING WAVES AND THEIR INTERACTIONS WITH A RESTRAINED SHIP USING A NON-HYDROSTATIC WAVE-FLOW MODEL^{*}

ABSTRACT

This paper presents a numerical model to simulate the evolution of waves and their interactions with a restrained ship that is moored in coastal waters. The model aims to be applicable at the scale of a harbour or coastal region, while accounting for the key physical processes that determine the hydrodynamic loads on the ship. Its methodology is based on the non-hydrostatic wave-flow model SWASH, which provides an efficient tool to simulate the nonlinear dynamics that govern the nearshore wave field. In this work, we propose a new numerical algorithm that accounts for the presence of a non-moving floating body, to resolve the wave impact on a restrained ship. The model is validated through comparisons with an analytic solution, a numerical solution, and two laboratory campaigns. The results of the model-data comparison demonstrate that the model captures the scattering of waves by a restrained body. Furthermore, it gives a reasonable prediction of the hydrodynamic loads that act on a restrained container ship for a range of wave conditions. Importantly, the model captures these dynamics efficiently, which demonstrates that it retains this favourable property of the non-hydrostatic approach when a floating body is included. The findings of this study suggest that the model provides a promising new alternative to simulate the nonlinear evolution of waves and their impact on a restrained ship at the scale of a realistic harbour or coastal region.

^{*}This chapter has been published as Rijnsdorp, D. P., and Zijlema, M. (2016): Simulating waves and their interactions with a restrained ship using a non-hydrostatic wave-flow model. *Coastal Engineering*, 114, 119–136

5.1. INTRODUCTION

A ship that is moored in a harbour or coastal region is subject to the local wave field, which may cause the moored ship to move. When the motions of the ship become too large, ship operations may need to be terminated, resulting in undesired economic losses. Therefore, an accurate prediction of the local wave field, the hydrodynamic loads acting on the ship (the forces and moments), and the resulting ship motions are of vital importance to ensure safe and continuous operations of a moored ship.

Numerical models provide a valuable tool to predict the wave-induced response of a moored ship. Such a model should account for the interactions between the local wave field and the ship, such as the scattering of the waves by the ship, and the radiation of waves due to the ship motions (e.g., Newman, 1977). Furthermore, the model should account for the complex nearshore evolution of the waves as they propagate from relatively deep water to shallower water depths. This includes processes like shoaling, refraction, diffraction, wave breaking, and nonlinear interactions. The latter is especially relevant in the nearshore, as nonlinear wave effects like infragravity waves can cause significant ship motions (e.g., González-Marco et al., 2008; Sakakibara and Kubo, 2008; López and Iglesias, 2014). This highlights that an accurate description of the local nonlinear wave field is required when predicting the wave-induced response of a ship that is moored in coastal waters.

A variety of model techniques have been developed to simulate the interactions between waves and ships (see Bertram, 2012, for a concise overview). The first efforts to solve these interactions were based on potential flow theory (e.g., Korvin-Kroukovsky and Jacobs, 1957; Hess and Smith, 1962), in which the flow is assumed to be irrotational and inviscid. In this context, the BEM has been a popular method to solve the wave-ship interactions. Such models, which are also known as panel models, are applied in both offshore (e.g., Huijsmans et al., 2001; Newman, 2005; Zhao et al., 2011) and coastal waters (e.g., Van Oortmerssen, 1976; You and Faltinsen, 2015; Xiong et al., 2015) to predict the wave impact on floating bodies. More recently, potential flow models based on the FEM have been developed to simulate similar interactions (e.g., Yan and Ma, 2007; Ma and Yan, 2009). Potential flow models based on the BEM and FEM share that they are not designed to simulate the evolution of waves at the scales of a coastal or harbour region. Consequently, they require information concerning the local wave field to predict the ship response based on an offshore wave climate

Furthermore, the assumption of potential flow is violated in the case of large wave impacts and significant ship motions (e.g., ship capsizing). In such extreme conditions, an alternative approach is desired to adequately simulate the ship response. With the increase of computational powers, various detailed Computational Fluid Dynamics (CFD) models have been developed that can resolve the turbulent flow field in the vicinity of a floating body. Examples include models that are based on the RANS equations (e.g., Hadžić et al., 2005; Lin, 2007; Stern et al., 2013), and models based on the SPH method (e.g., Bouscasse et al., 2013; Ren et al., 2015). For instance, RANS models have been used to simulate the seakeeping of ships, including the turbulent wake of the ship and rotating propellers (e.g., Wilson et al., 2006; Mofidi and Carrica, 2014). However, computational limitations restrict the application of such highly detailed models to relatively small scales, spanning only a few wave lengths and wave periods.

To simulate both the evolution of waves and their interactions with ships, several authors combined a wave model with a model that accounts for the wave-ship interactions (e.g., Bingham, 2000; Jiang et al., 2002; Van der Molen et al., 2006; Van der Molen and Wenneker, 2008; Dobrochinski, 2014). To our knowledge, the most advanced methodology that can solve this complex problem combined a phase resolving wave model (i.e., a Boussinesq or a non-hydrostatic wave model) with a panel model (Bingham, 2000; Van der Molen and Wenneker, 2008; Dobrochinski, 2014). In this approach, the wave model is first used to simulate the evolution of the waves as they propagate in coastal waters. The wave model does not account for the presence of the ship, and the computed wave field represents the waves that are not disturbed by the ship. Next, a panel model based on linear potential theory is used to compute the interactions between this undisturbed wave field and the ship. The advantage of such a coupled wave-panel model is that it combines a wave model that can resolve the nonlinear wave evolution from deep to shallow water at the scale of a harbour or coastal region, with a panel model that includes a detailed schematisation of the ship's hull to determine the wave-induced response. However, the assumption of linear potential flow restricts this approach to relatively mild wave conditions, when the wave non-linearity is small (i.e., $a/d \ll 1$ in shallow water, where a is the wave amplitude and d is the still water depth, Bingham, 2000). Moreover, the coupling of two models complicates the usage and maintenance of this methodology.

In this work, we pursue an alternative approach to simulate the evolution of waves and their impact on a ship that is moored in coastal waters. Our ultimate goal is to develop a single model to simulate the wave-induced response of a moored ship based on an offshore wave climate. The model aims to be applicable at the scales of a harbour or coastal region, while accounting for the relevant processes on both relatively large scale (the nonlinear wave transformation over a complex bathymetry) and on small scale (the wave-ship interactions). Our approach is based on the non-hydrostatic wave-flow model SWASH. Recent studies have shown that non-hydrostatic wave-flow models like SWASH are capable of resolving the complex evolution of waves over sloping bottoms (e.g., Yamazaki et al., 2009; Ma et al., 2012; Cui et al., 2012). This includes the nonlinear wave dynamics in the surf zone (Smit et al., 2013, 2014), and the nearshore evolution of infragravity waves (e.g., Ma et al., 2014b; Rijnsdorp et al., 2014, 2015a; De Bakker et al., 2016), which play a key role in the wave-induced response of a ship that is moored in shallow water. This paper presents the first crucial step towards the development of such a single model tool. To predict the wave-induced response of a moored ship, an accurate description of the local wave field and the hydrodynamic loads are of vital importance. In this work, we advance the capabilities of the SWASH model to resolve the interactions between the waves and a non-moving floating body. This allows the model to resolve the wave impact on a restrained ship, providing the basis for future developments to simulate the wave-induced motions of a moored ship.

In non-hydrostatic models like SWASH, a fractional step method is used to solve the RANS equations. In this approach, the pressure is decomposed into a hydrostatic and a non-hydrostatic part. First, a discrete free-surface equation is solved for the hydrostatic pressure (which determines the position of the free surface) to compute a provisional velocity field. In the subsequent step, the velocities are corrected after solving a Poisson

equation for the non-hydrostatic pressure. One of the key properties of such models is their efficiency in simulating the nearshore wave dynamics due to the use of the Keller-Box scheme to discretise the non-hydrostatic pressure (e.g., Stelling and Zijlema, 2003).

In this work, we present a new numerical algorithm to account for the presence of a non-moving floating body in such a model (see §5.2). The inclusion of a floating body complicates the problem as the model has to account for the simultaneous occurrence of free-surface flow and the pressurised flow underneath the body. Following the approach of Casulli and Stelling (2013), we derived a free-surface equation that correctly describes the global continuity equation in both the free surface and the pressurised region. To ensure that the method is unconditionally stable with respect to the wave celerity (which is infinite in the pressurised region), our algorithm is based on the semi-implicit version of the SWASH model (e.g., Zijlema and Stelling, 2005). Furthermore, we used the first-order pressure projection method (e.g., Chorin, 1968), instead of the second-order pressure correction method (e.g., Van Kan, 1986) that is used in SWASH, to deal with the pressurised flow underneath the ship. However, to retain the second-order accuracy when simulating free-surface flows, the second-order projection method is used in regions where the flow is bounded by a free surface (e.g., Vitousek and Fringer, 2013).

To assess the capabilities of this approach, we validated the model for the interactions between waves and a restrained ship using a total of four test cases. The first two tests consider the scattering of waves by a rectangular pontoon in a two-dimensional vertical (2DV) domain. First, we validate the model using an analytic solution for the scattering of linear monochromatic waves (§5.3). The second test case is based on a numerical solution of the scattering of a solitary wave (§5.4). Following these 2DV tests, we consider two laboratory experiments that were conducted in a wave basin, to assess the model capabilities in a three-dimensional (3D) physical domain. The third test case focusses on the scattering of regular waves by a rectangular pontoon (§5.5). To gain insight in the model capabilities for a more realistic environment, the final test considers an experimental campaign in which a realistic ship model (a Panamax container ship) was subject to a range of wave conditions, including short-crested sea states (§5.6). Finally, we summarise and discuss our findings in §5.7.

5.2. NUMERICAL METHODOLOGY

The numerical methodology of the model that was developed in this work is based on the non-hydrostatic wave-flow model SWASH (Zijlema et al., 2011). The governing equations of the model are the RANS equations for an incompressible fluid with a constant density. The model solves the layer-averaged RANS equations using a curvilinear coordinate framework for the two horizontal dimensions, and a terrain following coordinate framework for the vertical dimension.

In the following, we present the numerical methodology that was adopted to account for the presence of a non-moving floating body. For the sake of clarity, we present our approach in its simplest form, without loss of generality. We present the numerical approach in a Cartesian framework and for one horizontal dimension. This relatively simple presentation of the modelling framework includes the numerical details that are relevant for including a floating body in the numerical domain. Although porous structures are included in the simulations of one of the test cases, we do not discuss their numeri-

cal discretisation as this is not the focus of this study (see 5.A for a brief description of its implementation).

GOVERNING EQUATIONS

We consider a two-dimensional domain that is bounded in the vertical by an interface at the top and at the bottom (see Fig. 5.1). At the top interface, the domain is bounded by either a free surface $z = \zeta(x, t)$, or a rigid non-moving floating body $z = -S(x)$, where t is time, x and z are the Cartesian coordinates, and $z = 0$ is the still water level. At the bottom, the domain is bounded by a fixed bed, $z = -d(x)$. In this domain, we can distinguish between two subdomains: an outer domain where the flow is bounded by a free surface, and an inner domain where the flow is pressurised.

In this framework, the governing equations read,

$$\frac{\partial u}{\partial x} + \frac{\partial w}{\partial z} = 0, \quad (5.1)$$

$$\frac{\partial u}{\partial t} + \frac{\partial uu}{\partial x} + \frac{\partial wu}{\partial z} = -g \frac{\partial \zeta}{\partial x} - \frac{\partial p}{\partial x} + \frac{\partial \tau_{xx}}{\partial x} + \frac{\partial \tau_{xz}}{\partial z}, \quad (5.2)$$

$$\frac{\partial w}{\partial t} + \frac{\partial uw}{\partial x} + \frac{\partial ww}{\partial z} = -\frac{\partial p}{\partial z} + \frac{\partial \tau_{zx}}{\partial x} + \frac{\partial \tau_{zz}}{\partial z}, \quad (5.3)$$

where $u(x, z, t)$ is the velocity in x direction, $w(x, z, t)$ is the velocity in z direction, g is the gravitational acceleration, $\tau(x, z, t)$ represents the turbulent stresses, $p(x, z, t)$ is the non-hydrostatic pressure (normalised by a reference density), and $\zeta(x, t)$ is the piezometric head (which is equivalent to the free surface in the outer domain, see Fig. 5.1). At the top and bottom interfaces, the following kinematic boundary conditions apply,

$$w|_{z=\zeta} = \frac{\partial \zeta}{\partial t} + u \frac{\partial \zeta}{\partial x}, \quad (5.4)$$

$$w|_{z=-S} = -u \frac{\partial S}{\partial x}, \quad (5.5)$$

$$w|_{z=-d} = -u \frac{\partial d}{\partial x}. \quad (5.6)$$

At the bottom, we approximate the effect of bottom friction using a quadratic friction law,

$$\tau_{xz}|_{z=-d} = c_f \frac{U|U|}{H}, \quad (5.7)$$

where c_f is a dimensionless friction coefficient, H is the total water depth, and U is the depth-averaged velocity ($U = \frac{1}{H} \int u dz$). In this study, we computed c_f using the Manning-Strickler formulation ($c_f = gn^2/H^{1/3}$, where n is the Manning roughness coefficient). The turbulent stresses are evaluated using a turbulent viscosity approximation (e.g., $\tau_{xx} = \nu_h \frac{\partial u}{\partial x}$ in which ν_h is the horizontal eddy viscosity, and $\tau_{xz} = \nu_v \frac{\partial u}{\partial z}$ in which ν_v is the vertical eddy viscosity). In a 3D framework, the horizontal viscosities are estimated using a Smagorinsky-type formulation (Smagorinsky, 1963). In this work, the model is applied with a coarse vertical resolution (2 layers) which implies that it does not fully resolve the vertical flow profile. To account for some vertical mixing nonetheless, and to

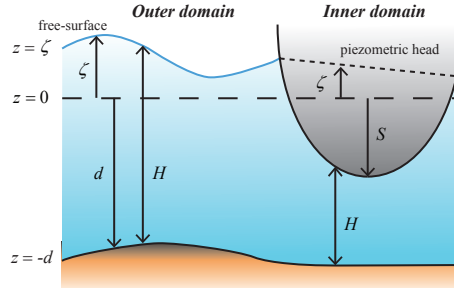


Figure 5.1: Sketch of the two-dimensional domain, including a free surface, a floating body, and a fixed bed.

spread the effect of bottom friction over the vertical, the vertical viscosity ν_v was set at a constant value of $10^{-4} \text{ m}^2 \text{ s}^{-1}$.

To close the set of equations, we derive an extra equation to determine the piezometric head. Integrating the continuity equation (5.1) from the bottom to the free surface and applying the relevant kinematic boundary conditions (5.4 and 5.6) yields the following global-continuity equation in the outer domain,

$$\frac{\partial \zeta}{\partial t} + \frac{\partial}{\partial x} \int_{-d}^{\zeta} u dz = \frac{\partial \zeta}{\partial t} + \frac{\partial HU}{\partial x} = 0,$$

where $H = d + \zeta$ is the water depth in the outer domain. This equation governs the position of the free surface in the outer domain, where the waves are dispersive. However, when a floating body is included in the domain, a different equation applies in the pressurised region. Integrating Eq. (5.1) with the relevant kinematic boundary conditions (5.5,5.6) yields the following equation,

$$\frac{\partial}{\partial x} \int_{-d}^{-S} u dz = \frac{\partial HU}{\partial x} = 0,$$

where $H = d - S$ is the water depth in the inner domain. This steady-state equation determines the piezometric head in the pressured region. With the present assumptions of

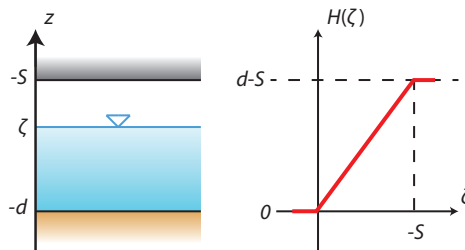


Figure 5.2: Piecewise linear function of the total water depth H , that is bounded by a fixed bottom ($z = -d$) and a floating body ($z = -S$).

an incompressible fluid and a rigid floating body, this equation implies that the celerity is infinite underneath the ship. Consequently, perturbations in the flow and pressure field are spread instantly over the entire inner domain.

Following the approach of Casulli and Stelling (2013), these two global continuity equations are recast into a single equation by defining the total water depth as a piecewise linear function of the piezometric head, $H(\zeta) = \max(0, d + \min(-S, \zeta))$. With this formulation, the water depth has a minimal value of zero, and increases linearly as a function of ζ , with an upper bound equal to the level of the floating body (illustrated in Fig. 5.2). With this definition of the water depth, the two global continuity equations are combined into,

$$\frac{\partial \max(-d, \min(-S, \zeta))}{\partial t} + \frac{\partial HU}{\partial x} = 0. \quad (5.8)$$

This single equation captures the nature of the flow in the outer and inner domain. This implies that the resulting model accounts for the finite celerity in the outer domain (where waves are dispersive), and the infinite celerity in the inner domain where the flow is pressurised. Furthermore, a pressurised cell can become a free surface cell, and vice versa. This allows the model to account for the wetting and drying of the ship as the water moves up and down the hull.

SPATIAL AND TEMPORAL DISCRETISATION

The governing equations are discretised on a structured grid with a fixed number of layers K between the top and bottom interface, where $k = 1$ is the bottom layer, and $k = K$ is the top layer. The resulting grid has a spatially varying layer thickness of $h_k = H/K$, and a constant width Δx . A staggered grid is used to arrange the variables: the piezometric head is located at a cell centre, the u velocities are located at the centre the horizontal cell faces and the w velocities are located at the centre of the vertical cell faces (see Fig. 5.3). In the outer domain, the non-hydrostatic pressure variables are located at a vertical cell face following the Keller-Box scheme (Lam and Simpson, 1976). Compared to the traditional cell centred arrangement (e.g., Stansby and Zhou, 1998; Casulli and Stelling, 1998), this cell face arrangement significantly improves the dispersive properties of the model (e.g., Stelling and Zijlema, 2003; Smit et al., 2014). For typical coastal and harbour applications, two layers are generally sufficient to resolve the dispersion of the wave field. In the simulations of this paper, two vertical layers were used as well.

In the inner domain, the piezometric head and velocity variables are arranged in a similar fashion. However, the non-hydrostatic pressure variables are arranged using the cell centred arrangement instead of the Keller-Box scheme. We adopt this arrangement as the application of the Keller-Box scheme is not advantageous in the inner domain where the celerity is infinite. In addition, the centred arrangement allows for an easier implementation, and results in a smaller stencil of the Poisson equation, which will become apparent in the following (e.g., Eq. (5.14)).

A variable which is required at a location where it is not known is interpolated or extrapolated from its surrounding variables. In both domains, these techniques follow the methodology of SWASH. Details regarding the various types of interpolation used in SWASH (e.g., linear interpolation, upwind approximations, and flux limiters) can be found in Zijlema and Stelling (2005, 2008), and Zijlema et al. (2011). In the following,

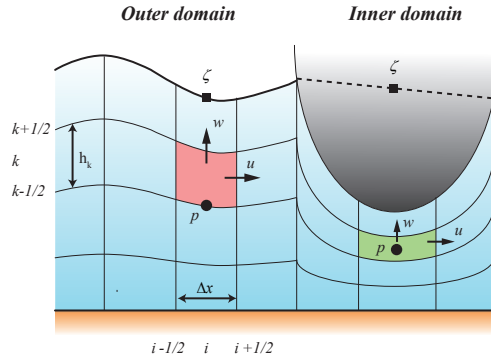


Figure 5.3: Horizontal and vertical grid definition, and the staggered variable arrangement on grid. A cell with its centre at i, k is bounded by a top ($k+1/2$) and bottom interface ($k-1/2$), and the left ($i-1/2$) and right ($i+1/2$) grid interfaces. The variable arrangement is depicted for the outer domain (illustrated in the red control volume) and the inner domain (illustrated in the green control volume).

5

variables that are computed using (bi)linear interpolation or extrapolation are denoted with an overline, including the direction in which it takes place. For example, a layer thickness at the cell face $i+1/2$ that is computed using linear interpolation in x direction is written as $\overline{h_{i+1/2,k}}^x$. Variables that are interpolated using upwind approximations, or flux limiters are denoted with a hat (e.g., $\hat{H}_{i+1/2}$). To achieve second-order accuracy in space, and to avoid undesired oscillations near sharp gradients, we use the MUSCL limiter (Van Leer, 1979) to determine the water depth and layer thickness at a horizontal cell face (e.g., Zijlema et al., 2011). Note that the water depth follows from $H = d - S$ if a cell is located in the inner domain. Here, the water depth and the layer thickness at a cell face can be directly computed from the position of the bottom and the ship, and do not require interpolation.

To simulate the simultaneous occurrence of free surface and pressurised flows, the numerical method must be unconditionally stable with respect to the celerity, which is infinite in the pressurised region (e.g., Casulli and Stelling, 2013). For this purpose, we use an (semi) implicit method to discretise the velocities in the global continuity equation (5.8) and the piezometric head and the non-hydrostatic pressure in the momentum equations (5.2-5.3). The advective and turbulent stress terms in the momentum equations (5.2-5.3) are discretised using the same methods as in SWASH. As such, the vertical advective and turbulent stress terms are discretised using the semi-implicit θ -scheme (with $\theta = 1/2$), to prevent a time step restriction when the water depth becomes small (e.g., in the case of flooding and drying at a beach). Explicit schemes are used to discretise the horizontal advective (the second-order accurate MacCormack scheme) and the turbulent stress terms (the first-order accurate explicit Euler scheme). In space, the turbulent terms are discretised using (second-order) central differences. For the spatial discretisation of the advective terms, various numerical techniques can be used in SWASH (e.g., first-order upwind, flux limiters, and central differences). In this work, the advective terms in the u -momentum equation are discretised using the MUSCL limiter. In the w -momentum equation, the horizontal advective terms are discretised using the

second-order BDF scheme, and the vertical term is discretised using the first-order up-wind scheme.

In the following, we present the discretised versions of the layer-averaged equations, and the solution algorithm that we adopted to include a floating body. To improve the readability of the paper, we focus on the aspects that are affected by including a floating body in the domain. As the inclusion of the body does not affect the integration of the equations over a layer, we omit their details as they have been extensively treated before (Stelling and Zijlema, 2003; Zijlema and Stelling, 2005). For the same reason, we do not present the discretisation of the advective and turbulent stress terms. Details regarding their discretisation can be found in Zijlema and Stelling (2005, 2008) and Zijlema et al. (2011).

CONTINUITY EQUATIONS

The global continuity equation (5.8) is discretised in time using the θ -method. For brevity, we will write the semi-implicit terms that arise due to this method for some variable ϕ as $\phi^{n+\theta} = \theta\phi^{n+1} + (1-\theta)\phi^n$, in which n indicates the time level ($t^n = n\Delta t$, where Δt is a fixed time step) and θ is an implicitness factor (with an allowable range of $1/2 \leq \theta \leq 1$). With $\theta = 1$ the θ -method is equivalent to the first-order accurate implicit Euler method, and with $\theta = 1/2$ it is equivalent to the second-order Crank Nicholson method. A global mass conserving discretisation of Eq. (5.8) is given by,

$$\frac{\max(-d_i, \min(-S_i, \zeta_i^{n+1})) - \max(-d_i, \min(-S_i, \zeta_i^n))}{\Delta t} + \frac{\hat{H}_{i+1/2}^n U_{i+1/2}^{n+\theta_{i+1/2}} - \hat{H}_{i-1/2}^n U_{i-1/2}^{n+\theta_{i-1/2}}}{\Delta x} = 0, \quad (5.9)$$

in which U is the approximated depth-averaged velocity ($U = 1/H \sum_{k=1}^K h_k u_k$, where u_k is the layer-averaged u -velocity). In this work, a spatially varying $\theta_{i\pm 1/2}$ parameter is adopted to account for the different flow regimes in the outer and inner domain. To compute the steady-state solution of Eq. (5.9) when the flow is pressurised, the value of $\theta_{i\pm 1/2}$ is set at 1 when a horizontal grid interface $i \pm 1/2$ is located in the inner domain. If an interface is located in the outer domain, $\theta_{i\pm 1/2} = 1/2$ to prevent numerical wave damping.

A local mass conserving discretisation of the local continuity equation (5.1) is given by,

$$\frac{\overline{h_{i+1/2,k}^n}^x u_{i+1/2,k}^{n+1} - \overline{h_{i-1/2,k}^n}^x u_{i-1/2,k}^{n+1}}{\Delta x} + w_{i,k+1/2}^{n+1} - w_{i,k-1/2}^{n+1} - u_{i,k+1/2}^{n+1} \frac{z_{i+1/2,k+1/2}^n - z_{i-1/2,k+1/2}^n}{\Delta x} + u_{i,k-1/2}^{n+1} \frac{z_{i+1/2,k-1/2}^n - z_{i-1/2,k-1/2}^n}{\Delta x} = 0, \quad (5.10)$$

in which $z_{k\pm 1/2}$ represent the vertical position of the interfaces at the top ($z_{k+1/2}$) and bottom ($z_{k-1/2}$) of a layer.

MOMENTUM EQUATIONS

The layer-averaged version of the u -momentum equation (5.2) is discretised as,

$$\frac{u_{i+1/2,k}^{n+1} - u_{i+1/2,k}^n}{\Delta t} = -g \frac{\zeta_{i+1}^{n+\theta_{i+1/2}} - \zeta_i^{n+\theta_{i+1/2}}}{\Delta x} - P u_{i+1/2,k}^{n+1}, \quad (5.11)$$

where $Pu_{i\pm 1/2,k}^{n+1}$ represents the discretisation of the non-hydrostatic pressure term. For brevity, we omit details regarding the discretisation of the advective and turbulent terms in this momentum equation. For the time integration of the piezometric head gradient, the θ -method is used with a spatially varying $\theta_{i\pm 1/2}$ parameter. Similar to the global continuity equation, the value of this parameter is set depending on the location of the grid interface $i \pm 1/2$, that is, $\theta_{i\pm 1/2} = 1/2$ in the outer domain and $\theta_{\pm 1/2} = 1$ in the inner domain.

The layer-averaged non-hydrostatic pressure term is evaluated as,

$$Pu_k = \frac{1}{h_k} \int_{z_{k-1/2}}^{z_{k+1/2}} \frac{\partial p}{\partial x} dz = \frac{1}{h_k} \left(\frac{\partial p_k h_k}{\partial x} - p_{k+1/2} \frac{\partial z_{k+1/2}}{\partial x} + p_{k-1/2} \frac{\partial z_{k-1/2}}{\partial x} \right).$$

Discretising this term yields different expressions in the outer and inner domain due to the differences in the arrangement of the non-hydrostatic pressure variable (Fig. 5.3). In discretised form, $Pu_{i\pm 1/2,k}^{n+1}$ reads,

$$Pu_{i\pm 1/2,k}^{n+1} = \begin{cases} \frac{1}{\overline{h_{i\pm 1/2,k}^n}} \left[\frac{\overline{p_{i+1,k}^{n+1}} h_{i+1,k}^n - \overline{p_{i,k}^{n+1}} h_{i,k}^n}{\Delta x} \right. \\ \quad - \overline{p_{i+1/2,k+1/2}^{n+1}} \frac{z_{i+1,k+1/2}^n - z_{i,k+1/2}^n}{\Delta x} \\ \quad \left. + \overline{p_{i+1/2,k-1/2}^{n+1}} \frac{z_{i+1,k-1/2}^n - z_{i,k-1/2}^n}{\Delta x} \right] & \text{(Outer domain),} \\ \frac{1}{\overline{h_{i\pm 1/2,k}^n}} \left[\frac{\overline{p_{i+1,k}^{n+1}} h_{i+1,k}^n - \overline{p_{i,k}^{n+1}} h_{i,k}^n}{\Delta x} \right. \\ \quad - \overline{p_{i+1/2,k+1/2}^{n+1}} \frac{xz_{i+1,k+1/2}^n - z_{i,k+1/2}^n}{\Delta x} \\ \quad \left. + \overline{p_{i+1/2,k-1/2}^{n+1}} \frac{xz_{i+1,k-1/2}^n - z_{i,k-1/2}^n}{\Delta x} \right] & \text{(Inner domain).} \end{cases} \quad (5.12)$$

This discretisation introduces virtual points in both the outer and inner domain. For example, virtual points are located at the vertical cell faces in the inner domain, which are interpolated or extrapolated from the surrounding pressure variables (e.g., $\overline{p_{i+1/2,k+1/2}^{n+1}}$). Note that we take advantage of the pressure boundary condition at the free surface in the outer domain (i.e., $p|_{z=\zeta} = 0$), to prescribe the pressure variables at the free surface.

The layer-averaged version of the w -momentum equation (5.3) is discretised as,

$$\frac{w_{i,k+1/2}^{n+1} - w_{i,k+1/2}^n}{\Delta t} = -Pw_{i,k+1/2}^{n+1}, \quad (5.13)$$

$Pw_{i,k+1/2}^{n+1}$ represents the discretisation of the non-hydrostatic pressure term. In this equation, we omit details regarding the advective and turbulent terms for brevity. In the outer domain, Eq. (5.13) applies at all interfaces except for the bottom, where the kinematic

boundary condition (5.6) applies. In the inner domain, Eq. (5.13) only applies at the internal interfaces, and the kinematic boundary conditions apply at the top (5.5) and bottom interface (5.6).

Similar to the u -momentum equation, the discretised form of the non-hydrostatic pressure term is different in the outer and inner domain. In the outer domain, the non-hydrostatic pressure term, $Pw_{k+1/2} = \int_{z_k}^{z_{k+1}} \frac{\partial p}{\partial z} dz$, is evaluated using the Keller-Box scheme (Lam and Simpson, 1976). In this method, the non-hydrostatic pressure gradient is evaluated as the arithmetic average of the gradients at the vertical cell faces,

$$\frac{\partial p_k}{\partial z} = \frac{1}{2} \frac{\partial p_{k+1/2}}{\partial z} + \frac{1}{2} \frac{\partial p_{k-1/2}}{\partial z}.$$

With this expression, and following a straightforward evaluation of the $\frac{\partial p_k}{\partial z}$ term, we derive an expression for the gradient at the top cell interface $\frac{\partial p_{k+1/2}}{\partial z}$,

$$\frac{1}{2} \frac{\partial p_{k+1/2}}{\partial z} + \frac{1}{2} \frac{\partial p_{k-1/2}}{\partial z} = \frac{\partial p_k}{\partial z} \approx \frac{p_{k+1/2} - p_{k-1/2}}{h_k} \rightarrow \frac{\partial p_{k+1/2}}{\partial z} = 2 \frac{p_{k+1/2} - p_{k-1/2}}{h_k} - \frac{\partial p_{k-1/2}}{\partial z}.$$

The gradient at one interface lower, $\frac{\partial p_{k-1/2}}{\partial z}$, is evaluated similarly. A subsequent substitution of these gradient terms into $Pw_{k+1/2}$ results in the following expression,

$$Pw_{k+1/2} = \sum_{m=0}^{k-1} \left[(-1)^m 2 \frac{p_{k+1/2-m} - p_{k-1/2-m}}{h_{k-m}} \right] + (-1)^k \frac{\partial p_{1/2}}{\partial z}.$$

To close this expression, the vertical gradient of the non-hydrostatic pressure needs to be evaluated at the bottom (i.e., $\frac{\partial p_{1/2}}{\partial z}$). This term is neglected in this work as its contribution is zero when the bottom is flat, which is the case in the simulations of this study.

In the inner domain, we approximate the non-hydrostatic pressure term in a different manner,

$$Pw_{k+1/2} = \int_{z_k}^{z_{k+1}} \frac{\partial p}{\partial z} dz = \frac{p_{k+1} - p_k}{h_{k+1/2}}.$$

In conclusion, the discretised form of $Pw_{i,k+1/2}^{n+1}$ reads,

$$Pw_{i,k+1/2}^{n+1} = \begin{cases} \sum_{m=0}^{k-1} \left[(-1)^m 2 \frac{p_{i,k+1/2-m}^{n+1} - p_{i,k-1/2-m}^{n+1}}{h_{i,k-m}^n} \right] & \text{(Outer domain),} \\ \frac{p_{i,k+1}^{n+1} - p_{i,k}^{n+1}}{h_{i,k+1/2}^z} & \text{(Inner domain).} \end{cases} \quad (5.14)$$

In the outer domain, this equation implies that Eq. (5.13) depends on all pressure variables that are located at, and below the interface of interest. In contrast, this equation only depends on the two surrounding pressure variables when a face is located in the inner domain.

SOLUTION PROCEDURE

We employ a fractional step method that is known as the pressure projection method (e.g., Chorin, 1968) to solve the system of discretised equations. With this method, the time integration from n to $n + 1$ is split into two steps. In the first step (or hydrostatic step), a provisional velocity field (u^*) and the piezometric head ζ^{n+1} are computed using a reduced number of terms in the momentum equations (5.11,5.13). In the second step (or non-hydrostatic step), the non-hydrostatic pressure p^{n+1} and the velocity field u^{n+1} and w^{n+1} are computed. Within the present framework, this fractional step procedure implies that the horizontal momentum equation (5.11) is solved in two steps. First, a provisional u -velocity is computed in the hydrostatic step,

$$u_{i+1/2,k}^* = u_{i+1/2,k}^n - g \frac{\Delta t}{\Delta x} \left(\zeta_{i+1}^{n+\theta_{i+1/2}} - \zeta_i^{n+\theta_{i+1/2}} \right). \quad (5.15)$$

Subsequently, the u velocity at $n + 1$ is computed in the non-hydrostatic step,

$$u_{i+1/2,k}^{n+1} = u_{i+1/2,k}^* - \Delta t P u_{i+1/2,k}^{n+1}. \quad (5.16)$$

5

HYDROSTATIC STEP

In the hydrostatic step, the global continuity equation (5.9) is solved to compute ζ^{n+1} . For this purpose, the horizontal momentum equation (5.16) is substituted into Eq. (5.9), which yields an implicit equation for the unknown ζ^{n+1} . In this work, we use a predictor-corrector technique to solve this implicit equation. With this technique, the computation of the provisional horizontal velocity field u^* (5.15) is divided into two steps. First, we predict an estimate of u^* based on the piezometric head at the previous time step,

$$u_{i+1/2,k}^{**} = u_{i+1/2,k}^n - g \frac{\Delta t}{\Delta x} (\zeta_{i+1}^n - \zeta_i^n). \quad (5.17)$$

Subsequently, the provisional velocity field can be computed based on the piezometric head correction $\Delta\zeta (= \zeta^{n+1} - \zeta^n)$,

$$u_{i+1/2,k}^* = u_{i+1/2,k}^{**} - \theta_{i+1/2} g \frac{\Delta t}{\Delta x} (\Delta\zeta_{i+1} - \Delta\zeta_i). \quad (5.18)$$

To solve this equation, the piezometric head correction needs to be computed first. Substituting the equations for u^{n+1} (5.16) and u^* (5.18) in the global continuity equation (5.9) yields an implicit equation for $\Delta\zeta$,

$$\begin{aligned} & \max(-d_i - \zeta_i^n, \min(-S_i - \zeta_i^n, \Delta\zeta_i)) \\ & - g \frac{\Delta t^2}{\Delta x^2} [\theta_{i+1/2}^2 \hat{H}_{i+1/2}^n (\Delta\zeta_{i+1} - \Delta\zeta_i) - \theta_{i-1/2}^2 \hat{H}_{i-1/2}^n (\Delta\zeta_i - \Delta\zeta_{i-1})] \\ & = \max(-d_i - \zeta_i^n, \min(-S_i - \zeta_i^n, 0)) \\ & - \frac{\Delta t}{\Delta x} [\hat{H}_{i+1/2}^n (\theta_{i+1/2} U_{i+1/2}^{**} + (1 - \theta_{i+1/2}) U_{i+1/2}^n) - \hat{H}_{i-1/2}^n (\theta_{i-1/2} U_{i-1/2}^{**} + (1 - \theta_{i-1/2}) U_{i-1/2}^n)] \\ & + \sum_{k=1}^K \frac{\Delta t^2}{\Delta x} \left(\beta_{i+1/2} \theta_{i+1/2} \overline{h_{i+1/2,k}^n}^x P u_{i+1/2,k}^{n+1} - \beta_{i-1/2} \theta_{i-1/2} \overline{h_{i-1/2,k}^n}^x P u_{i-1/2,k}^{n+1} \right). \end{aligned} \quad (5.19)$$

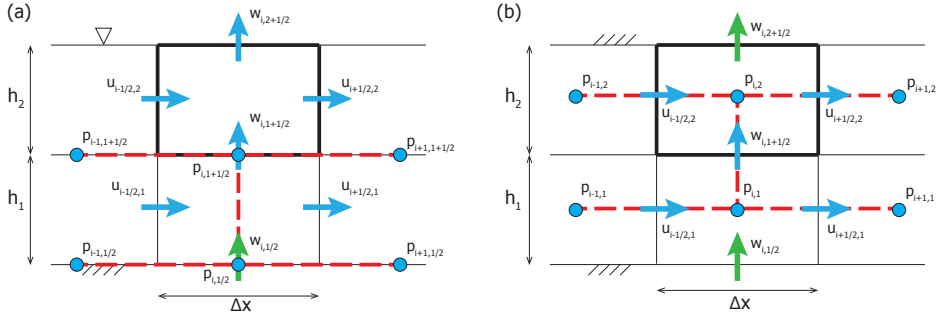


Figure 5.4: The locations of the unknowns, and the stencil of the non-hydrostatic pressure in the outer domain (a) and in the inner domain (b) for a two layer model. The thick black lines indicate the control volume of the local continuity equation. Green velocities are computed using the kinematic boundary condition, and blue velocities are computed using the momentum equations. The dashed red line indicates the stencil of the non-hydrostatic pressure.

This implicit equation represents a (positive definite and symmetric) tridiagonal piecewise linear system of equations for $\Delta\zeta$, which is solved using the Newton-type iterative method of Brugnano and Casulli (2009) in combination with a tridiagonal matrix algorithm¹. The parameter β indicates if the contribution of p^{n+1} is included ($\beta = 1$) or excluded ($\beta = 0$) in the global continuity equation. If $\beta = 1$ in Eq. (5.19), the temporal accuracy of the pressure projection method is second-order in simulating free-surface flows, whereas the method is first-order accurate if $\beta = 0$ (e.g., Vitousek and Fringer, 2013). Similar to $\theta_{i\pm 1/2}$, the parameter $\beta_{i\pm 1/2}$ can be varied in the domain, which will be discussed in §5.2. If $\beta_{i\pm 1/2} = 1$ in any of the cells, Eq. (5.19) cannot be directly solved as the contribution of p^{n+1} in Pu^{n+1} is not yet known. To include this contribution, several iterations over the hydrostatic and non-hydrostatic steps are required.

NON-HYDROSTATIC STEP

In the non-hydrostatic step, the velocity field at $n + 1$ is computed based on the non-hydrostatic pressure at $n + 1$. The u^{n+1} velocity is computed following Eq. (5.16), and w^{n+1} is computed as,

$$w_{i,k+1/2}^{n+1} = w_{i,k+1/2}^n - \Delta t P w_{i,k+1/2}^{n+1}. \quad (5.20)$$

To solve these equations, p^{n+1} is first computed based on the local continuity equation (5.10). Substituting the momentum equations and the relevant kinematic boundary conditions in Eq. (5.10) yields a Poisson equation for p^{n+1} . Fig. 5.4 illustrates the locations of the unknowns and the stencil of the non-hydrostatic pressure in the outer and inner domain for a model with two vertical layers. The Poisson equation (which is asymmetric and not positive definite) is solved using a preconditioned BiCGSTAB solver (e.g., Barrett et al., 1994; Zijlema and Stelling, 2005).

¹In the case of two horizontal dimensions, the system is pentadiagonal and solved using a preconditioned conjugate gradient method (e.g., Barrett et al., 1994).

SOLUTION ALGORITHM

The solution algorithm can be summarised as follows,

1. Start the computation with ζ^n , u^n , w^n , p^n , from the initial conditions or from the previous time step.
2. **Hydrostatic step**
 - (a) Solve Eq. (5.17) to compute the estimate of the provisional horizontal velocity (u^{**}).
 - (b) Solve the global continuity equation (5.19) to compute the piezometric head correction ($\Delta\zeta$).
 - (c) Solve Eq. (5.18) to compute the provisional horizontal velocity field (u^*), which satisfies the global continuity equation.
3. **Non hydrostatic step**
 - (a) Solve the Poisson equation resulting from the local continuity equation (5.10) to compute the non-hydrostatic pressure at the next time step (p^{n+1}).
 - (b) If the non-hydrostatic pressure is included in the hydrostatic step ($\beta = 1$), return to step 2b and repeat until convergence is reached.
4. Solve Eq. (5.16) and Eq. (5.20) to compute the divergence-free velocity field (u^{n+1} , and w^{n+1}), and advance the computation to the next time step.

This algorithm differs from the conventional SWASH model, which uses the explicit leapfrog scheme or the semi-implicit θ -method in combination with the pressure correction method of Van Kan (1986) to solve the layer-averaged RANS equations. However, to simulate the simultaneous occurrence of free surface and pressurised flows, the algorithm presented in this work is based on the semi-implicit version of the SWASH model as explicit schemes are not suited to simulate pressurised flows (e.g., Casulli and Stelling, 2013). Furthermore, we implemented a spatially varying implicitness parameter of the θ scheme, with $\theta = 1$ in the inner domain and $\theta = 1/2$ in the outer domain. This allows the model to compute the steady-state solution of the global continuity equation in the inner domain, and at the same time it prevents undesired numerical wave damping in the outer domain.

The nature of the flow regime in the pressurised region also implies the use of the first-order accurate pressure projection method ($\beta = 0$ in Eq. (5.19)), instead of the second-order accurate pressure correction method. Note that the main difference between the pressure projection and pressure correction method is the inclusion of an explicit non-hydrostatic pressure contribution in the hydrostatic step (see Stelling and Zijlema, 2003, for more details). The disadvantage of the first-order scheme is that it introduces a significant amount of wave damping in the outer domain. To retain the second-order accuracy in the outer domain and to prevent this damping (e.g., Vitousek and Fringer, 2013), the non-hydrostatic pressure contribution was included in the global continuity equation when a cell face is located in the outer domain (i.e., $\beta_{i\pm 1/2} = 1$ in Eq. (5.19)).

COMPUTATION OF HYDRODYNAMIC FORCES AND MOMENTS

The resulting numerical model provides the flow and pressure field in the numerical domain, while accounting for the presence of the floating body. The resulting hydrodynamic forces that act on the body are found by integrating the total pressure over the wet surface of the body,

$$\mathbf{F} = \iint_{\mathcal{H}} P \mathbf{n} \, d\mathcal{H},$$

where $\mathbf{F} = (F_x, F_y, F_z)$, P is the total pressure (i.e., the combined hydrostatic and non-hydrostatic pressure), \mathcal{H} represents the wet surface of the body, and \mathbf{n} is the unit vector normal to the body surface. The individual components of \mathbf{F} are known as the surge force (F_x), the sway force (F_y), and the heave force (F_z). The moments around the centre of gravity of the body are computed as,

$$\mathbf{M} = \iint_{\mathcal{H}} (\mathbf{r} - \mathbf{r}_c) P \mathbf{n} \, d\mathcal{H},$$

where $\mathbf{M} = (M_x, M_y, M_z)$, \mathbf{r} is the position vector of the pressure acting on the body surface, and \mathbf{r}_c is the position vector of the centre of gravity of the body. The individual components of \mathbf{M} are known as the roll moment (M_x), the pitch moment (M_y), and the yaw moment (M_z).

5

5.3. SCATTERING OF LINEAR MONOCHROMATIC WAVES BY A PONTOON

We consider the interaction between linear monochromatic waves and a non-moving pontoon that is located in water of constant depth (see Fig. 5.5 for the geometry and the dimensions of the pontoon). For such a 2DV set-up, Cointe et al. (1991) presented an analytic solution of the linearised potential flow problem. To assess the model capabilities for this problem, model results are compared with the analytic solution for the (partial) reflection and transmission of the waves, and for the hydrodynamic loads that act on the body. A comparison is made for a series of monochromatic waves, with periods varying between 1 to 5 s and a constant small wave steepness ($a/L = 1 \times 10^{-5}$, where a is the wave amplitude and L is the wave length).

In the analytic solution of Cointe et al. (1991), the domain is divided in three sub-domains (up wave, down wave and below the pontoon), in which the velocity potential

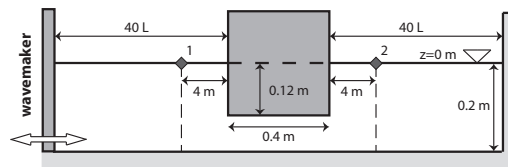


Figure 5.5: Sketch of the numerical set-up, including the geometry and dimensions of the pontoon. Note that the sketch is not at scale. The diamonds markers at the still water level indicate the output locations of the numerical model. These locations were positioned at a distance of 20 water depths away from the body ($= 4$ m), to minimise the effect of evanescent modes (which decay exponentially away from the pontoon).

is expressed by the appropriate eigenfunction expansions. These eigenfunction expansions consist of a single propagating wave mode and an infinite series of evanescent modes. In contrast with a propagating wave, evanescent modes exhibit an exponential behaviour in the horizontal plane, and a sinusoidal variation in the vertical. They are primarily important near sudden changes in the water depth, like the interfaces between the sub-domains. At these interfaces, they are necessary to match the different solutions in the sub-domains. Matching the eigenfunctions and their horizontal derivatives at the two interfaces between the three sub-domains, and truncating them at a certain number of terms, yields an algebraic system of equations for the unknown velocity potential. This system was solved using the Symbolic Toolbox of Matlab. For the wave conditions considered in this work, we found that the analytic solution converged when 21 terms were included in the eigenfunction expansions (not shown).

Fig. 5.5 illustrates the numerical set-up that was used in SWASH to reproduce this test case. A relatively large numerical domain (spanning more than 80 wave lengths) was used to prevent adverse effects on the analysis of wave reflections at the wavemaker and the vertical wall at the end of the domain. In the absence of such reflections, the predicted wave signal at sensor 2 represents a transmitted wave. Furthermore, as the wave conditions are linear, the signal at sensor 1 can be decomposed in an incident and reflected wave component. At this sensor, the incident signal was computed based on a simulation that excluded the floating body. Subsequently, the reflected signal was computed by taking the difference between the total signal and the incident signal at sensor 1. With this model set-up, the reflection and transmission coefficients were computed based on stationary reflected, transmitted, and reflected wave signals with a duration of at least 25 wave periods.

The temporal and grid resolution that was used in the SWASH simulations is based on the wave characteristics. The number of vertical layers was chosen based on the normalised water depth kd (in which k is the wave number), which determines the dispersive properties of the waves. In this test case, the kd values ranged between 0.15 – 1. For this range, two vertical layers are sufficient to resolve the wave dispersion (e.g., Zijlema et al., 2011; Smit et al., 2014). The horizontal grid resolution was set at 100 points per wave length (resulting in $\Delta x \sim 0.008 - 0.04$ m), which provides sufficient grid points to capture the wave shape. Finally, the time step was set at 300 points per wave period (resulting in $\Delta t \sim 0.003 - 0.02$ s) to minimise the numerical dissipation of the waves as they propagated through the relatively large domain.

RESULTS

Fig. 5.6 shows the comparison between the model and the analytic solution for this test case. For increasing wave periods, wave reflections reduce as the transmission increases (Fig. 5.6a-b). The model captures this trend, and the magnitude of the coefficients for the considered range of wave periods (Fig. 5.6a-c). Similarly, the predicted amplitudes of the two force components agree well with the analytic solution. Furthermore, the model captures the phase difference between F_x and F_z (illustrated by the red line and markers in Fig. 5.6e).

Compared to the force components, discrepancies are larger for M_y (which is typically under predicted), although its trend and especially its phase difference with F_z are

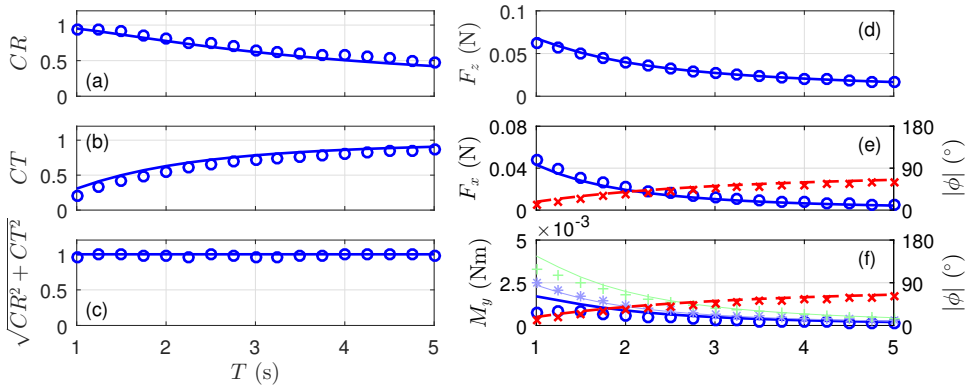


Figure 5.6: Comparison between the predicted (markers) and analytic results (lines) for the scattering of linear waves by a fixed pontoon. The left panels show the results for the reflection CR (a), transmission CT (b), and combined reflection and transmission coefficients $\sqrt{CR^2 + CT^2}$ (c). The right panels show the results for the amplitudes of the heave force F_z (d), surge force F_x (e), and pitch moment M_y (f). The full line and the circles indicate the amplitude of the hydrodynamic loads. The dashed lines and the crosses in panel (e) and (f) depict the absolute phase difference ($|\phi|$) between the respective load component (F_x or M_y) and F_z . In panel (f), the individual contributions of F_z and F_x to M_y are depicted by the light green and light blue results, respectively.

reproduced well (Fig. 5.6f). The moment is a linear combination of the moment contributions by F_z and F_x . These two contributions are nearly out of phase with each other, and the amplitude of M_y is therefore approximately given by the difference between the amplitude of F_z and F_x . Compared to the amplitude of M_y , the predicted amplitudes of these two contributions agree better with the analytic solution (illustrated by the light blue and light green results in Fig. 5.6f), although the F_z contribution is under predicted for shorter wave periods. This illustrates that M_z is sensitive to relatively small discrepancies in the force components.

The results of this test case show that the model predictions are in general agreement with the analytic solution for the transmission and reflection coefficients, and the hydrodynamic loads. This demonstrates that two layers are sufficient to capture the scattering of the waves by the pontoon, and the overall magnitude of the hydrodynamic loads that act on the pontoon.

To gain insight in the temporal accuracy of the model when solving a combination of free surface and pressurised flows, a numerical convergence test was conducted for one wave condition of this analytic test case (i.e., the wave with a period of 1 s). For this condition, we conducted a series of simulations with a gradually decreasing time step (starting at 80 points per wave period), for which the numerical solution is expected to converge to a final solution. By taking the root-mean-square-error between the results of the finest and a coarser temporal resolution, we can gain insight in the convergence behaviour and the temporal accuracy of the model. The results of this convergence test confirm that the overall temporal accuracy of the model is first order when predicting the hydrodynamic loads on a floating body (Fig. 5.7).

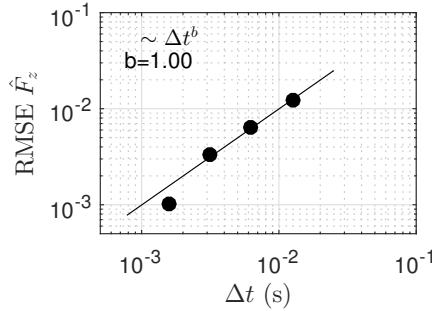


Figure 5.7: Root-mean-square-error of the heave force amplitude \hat{F}_z for a varying temporal resolution. The markers indicate the computed error, and the line indicates the best fit for the Δt^b power function (in which b is a real number). In the top left corner, the b coefficient of the power function is listed.

5

5.4. SCATTERING OF SOLITARY WAVE BY A PONTOON

In a similar 2DV set-up as §5.3, Lin (2006) considered the interactions between a fixed pontoon and a solitary wave. In this test, the still water depth was 1 m, and the pontoon had a width of 5 m and a draft of 0.4 m. The domain had a total length of 100 m, and the centre of the pontoon was positioned at $x = 32.5$ m (see Fig. 5.8a). In this set-up, Lin (2006) solved the scattering of a solitary wave with a height of 0.1 m using a non-hydrostatic σ -coordinate model and a VOF model. Both models yielded similar results with the same horizontal resolution, but with different vertical resolutions (i.e., 20 layers in the σ -model, and 130 meshes in the VOF model). In this work, we compare our model results with the results of Lin (2006), to demonstrate the capabilities of the present approach. To allow for a fair comparison, the spatial resolution was set in accordance with the study of Lin (2006), except for the vertical resolution. In this work, only 2 layers were employed to discretise the vertical domain. The horizontal grid resolution was set at $\Delta x = 0.05$ m, and the time step at $\Delta t = 0.01$ s.

RESULTS

After generation at the wavemaker, the solitary wave propagated towards the pontoon, where it partially reflected and transmitted. After interacting with the pontoon, the reflected part of the wave propagated back towards the wavemaker, where it was absorbed. This wave arrived after about 20 s at sensor 1, which is characterised by an initially positive elevation that is followed by a depression and some small oscillations (Fig. 5.8b). At roughly the same time, the transmitted wave arrived at sensor 2 (Fig. 5.8c). At both wave sensors, the results of the 2 layer SWASH model and the 20 layer σ -model are in excellent agreement. Naturally, the coarse vertical resolution that was used in this work implies that the model did not capture the vertical structure of the flow field in the vicinity of the structure. Nonetheless, the model captured the partial reflection and transmission of the solitary wave, which demonstrates that the present approach can efficiently resolve its interactions with the pontoon.

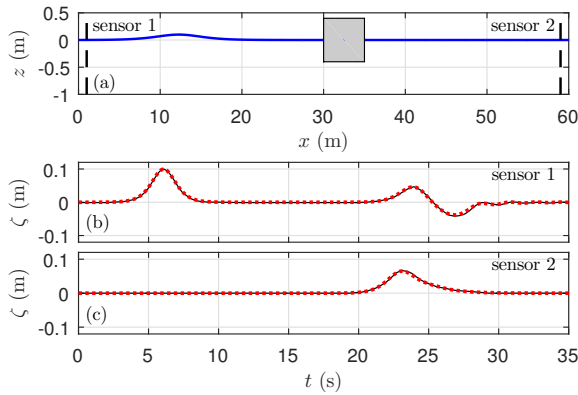


Figure 5.8: Set-up of the solitary wave test case and snapshot of the free surface at $t = 10$ s (a), and the time series of the free-surface elevation at the two wave sensors (b and c). The black line indicates the solution of the 20 layer model of Lin (2006), and the dotted red line indicates the solution of the 2 layer SWASH model.

5.5. SCATTERING OF REGULAR WAVES BY A PONTOON

The third test case considers the scattering of regular waves by a rectangular pontoon that was located inside a wave basin (Wang et al., 2011), see Fig. 5.9 for an overview of the laboratory set-up. The basin had a constant depth of 0.3 m, except for a deep water region near the wavemaker. The pontoon was restrained by four tripods; and had a width of 0.6 m, a length of 2 m, and a draft of 0.24 m. A total of 14 wave sensors were positioned in the vicinity of the pontoon to measure the surface elevation. A wave absorber was positioned along the right boundary of the wave basin, to minimise wave reflections. In this experiment, a total of six wave conditions were forced at the wavemaker, which varied in wave period ($T = 1.5, 2$, and 3 s) and wave height ($H = 3$, and 6 cm). Here, we consider the steepest wave condition and the weakest nonlinear wave condition of this experiment (i.e., a wave with $H = 6$ cm and $T = 1.5$ s, and a wave with $H = 3$ cm and $T = 3$ s, respectively).

The spatial and temporal resolution of the SWASH model were chosen based on the wave characteristics. The grid resolution was set at $\Delta x = \Delta y = 0.05$ m, corresponding

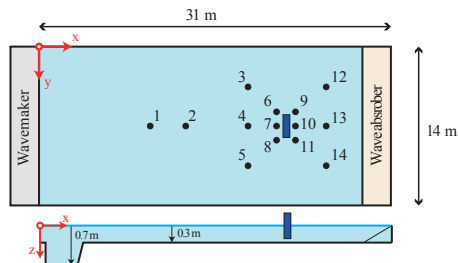


Figure 5.9: Overview of the experimental set-up. The numbered blue markers indicate the location of the wave sensors, and the blue rectangle indicates the position of the pontoon.

to at least 50 points per wave length. The temporal resolution was set at 100 points per wave period, which resulted in $\Delta t = 0.015 - 0.03$ s. Two vertical layers were used, which is sufficient to capture the wave dispersion for the range of normalised water depths encountered in the deep water region (which varied between 0.6 – 1.4). A sponge layer of 5 m width was positioned along the right boundary of the basin to dissipate incoming waves.

RESULTS

Fig. 5.10 shows the time series of the measured and predicted (normalised) surface elevation for the two wave conditions of this test case. They depict the surface elevation for 6 wave periods, after the initial waves have reached sensors 12-14. In this test case, waves are reflected and transmitted by the pontoon, and wave diffraction occurs in the lee of this body. For the steepest wave case, the first waves reached sensors 12-14 after approximately 20 s (Fig. 5.10a). For this relatively short-wave period, the waves reflected significantly at the pontoon and the wave transmission was very small, which is illustrated by the high wave elevation at sensor 7 and the low elevation at sensor 10. Due

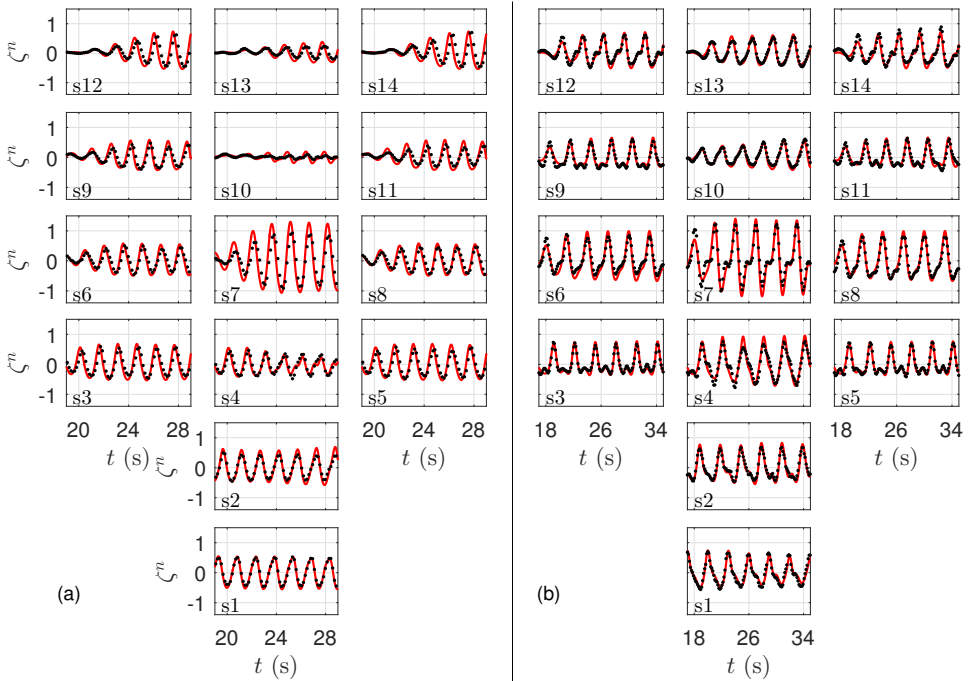


Figure 5.10: Time series of the surface elevation normalised by the incident wave height (ζ^n) at the 14 wave sensors for the steepest wave condition (a), with $H = 6$ cm and $T = 1.5$ s, and for the weakest nonlinear wave condition (b), with $H = 3$ cm and $T = 3$ s. The black dots indicate the measurements, and the red and blue line indicates the model predictions for the steep and weakly nonlinear condition, respectively. In each subplot, the number indicates the position of the respective wave sensor. Please note that the subplots are arranged according to the position of the respective wave sensor in the wave basin.

to the diffraction of waves in the lee of the pontoon, the wave elevation at sensor 13 is larger compared to the signal at sensor 10. At all sensors, the predicted wave signals agree well with the measurements. A small phase difference between the measurements and the predictions can be observed at sensors 12-14 (where the wave field is progressive). This is attributed to a small difference between the analytical and numerical wave celerity ($\sim 0.5\%$). For the simulation that considers a longer wave period, the waves experienced a stronger transmission and diffraction (Fig. 5.10b). The model reproduced the (irregular) wave elevation that was measured at all sensors, which illustrates that it captured this pattern. Overall, the model predictions agree well with the measurements of this laboratory experiment. These results demonstrate that the model captures the scattering of regular waves, and the diffraction in the lee of a rectangular pontoon.

5.6. WAVE IMPACT ON A CONTAINER SHIP

The last test case considers the wave impact on a restrained container ship for a range of wave conditions (Bijleveld, 2004; Van der Molen, 2006). This experimental campaign was conducted in a wave basin that measured approximately $40 \times 40 \text{ m}^2$. In the campaign, a restrained ship, located either in open water or in a harbour basin, was subject to a range of wave conditions, including realistic short-crested sea states (see Fig. 5.11 for a sketch of the experimental set-up). The still water depth in the basin was 0.2 m. To prevent reflections at the side walls of the basin, gravel beaches were constructed along parts of the basin boundaries. When the harbour basin was present, a gravel slope was positioned at the harbour wall that faced the wavemaker to reduce reflections.

The ship, a 1 : 100 scale model of a Panamax container ship, was restrained by six force transducers that fixed the ship to a steel frame. Based on these transducers, the

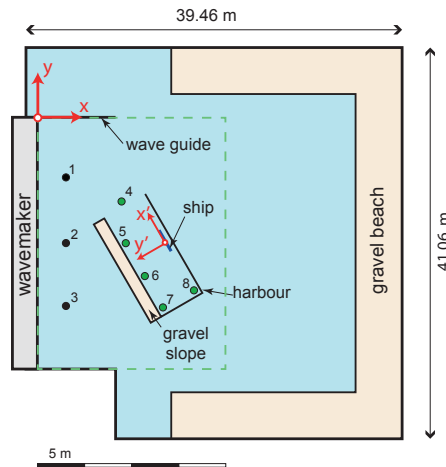


Figure 5.11: Overview of the laboratory set-up, including the harbour and the location of the ship. The numbered circles indicate the location of the wave sensors. Sensors 1-3 were present during all experiments, and sensors 4-8 were only available for the experiments which included the harbour basin. The thin dashed green line illustrates the region of interest.

forces and moments were measured relative to a ship coordinate system ($x' - y'$, illustrated in Fig. 5.11), in which the horizontal coordinates are rotated with 120° relative to the global coordinate system ($x - y$ in Fig. 5.11). With this set-up, small measurement errors in the forces can induce significant errors in the moments, and the roll moment in particular (e.g., Van der Molen, 2006). Nonetheless, we compare the model results and the measurements for all load components, but we anticipate that discrepancies are typically larger for the moments than for the forces. Several wave sensors were positioned inside the basin to measure the surface elevation. Near the wavemaker, three sensors were present for all simulations. For the simulations in which the harbour basin was present, five additional wave sensors were positioned in the vicinity of the ship (see Fig. 5.11).

Waves were forced using a piston-type wavemaker, including second-order wave control and reflection compensation. The wave conditions varied from monochromatic to short-crested waves. In this paper, we distinguish between the conditions in which the ship was moored in open water (labelled as OW) or inside the harbour basin (labelled HB). We consider a total of ten wave conditions: two regular wave conditions (labelled as OWr and HBr) and eight irregular wave conditions (with the label OWi and HBi). In the regular wave experiments, which had a duration of 10 min, a monochromatic wave was forced with an amplitude of 1 cm, a period of 1 s, and a direction perpendicular to the wavemaker. In the irregular experiments, both long-crested and short-crested wave fields were generated, of which the bulk wave parameters are listed in Table 5.1. In these test cases, the wave conditions differed mainly in the wave period, and in directional spreading. They varied from long-crested waves with a relatively long peak period (e.g., OWi2 and HBi2), to short-crested sea states with relatively short peak periods (e.g., OWi3 and HBi3).

Similar to the previous test cases, the temporal and spatial grid resolution of the model were chosen based on the characteristics of the wave conditions. Two vertical

Table 5.1: Wave parameters at the wavemaker for the irregular wave conditions of the experimental program. Listed are the wave height H_{m0} , the peak wave period T_p , the directional distribution of the wave spectrum $D(\theta)$ (which was constant over the frequencies), and the duration of the experiment T_{exp} . The directional distribution is defined as $D(\theta; f) = \frac{S_\zeta(f, \theta)}{S_\zeta(f)}$ (e.g., Holthuijsen, 2007), where $S_\zeta(f, \theta)$ is the frequency-direction spectrum and $S_\zeta(f)$ is the frequency spectrum of the surface elevation (see also Appendix 5.B). $D(\theta) = \delta$ corresponds to long-crested waves, in which δ is the Dirac delta function. The mean wave angle of all wave conditions is perpendicular to the wavemaker.

	H_{m0} (cm)	T_p (s)	$D(\theta)$	T_{exp} (min)
OWi1	1.5	1.0	δ	30
OWi2	1.5	1.5	δ	30
OWi3	1.5	1.0	$\cos^2(\theta)$	30
OWi4	1.5	1.5	$\cos^4(\theta)$	30
HBi1	3.0	1.0	δ	45
HBi2	3.0	1.5	δ	45
HBi3	3.0	1.0	$\cos^2(\theta)$	45
HBi4	3.0	1.5	$\cos^2(\theta)$	45

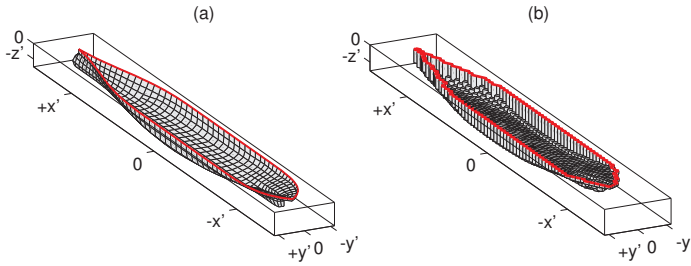


Figure 5.12: Sketch of the ship hull in the ship coordinate system. (a) Panel model of the Panamax ship. (b) Single valued ship function $S(x', y')$ used in the SWASH computations. The thick red line in (a) and (b) indicates the waterline contour.

layers were sufficient to capture the dispersion of the dominant waves (for which the kd values ranged 0.6 – 3.2). The grid resolution was set at $\Delta x = 0.02$ m and $\Delta y = 0.035$ m, which corresponds to at least 20 points per wave length for frequencies up to $2f_p$, where $f_p (= 1/T_p)$ is the peak frequency. The time step was set at 0.01 s, which corresponds to at least 50 points per wave period for frequencies up to $2f_p$. To reduce the computational effort, we reduced the domain size in both horizontal directions. The resulting numerical domain spans approximately 30×36 m². Furthermore, the grid resolution was set to increase linearly away from the region of interest (illustrated by the dashed green line in Fig. 5.11), with a maximum grid resolution of 0.25m. The Manning roughness coefficient was set at the default value used in SWASH, $n = 0.019$ s/m^{1/3}. Waves were generated at the numerical wavemaker using weakly nonlinear wave theory to include the bound infragravity waves (Rijnsdorp et al., 2015a), based on the wave parameters of the laboratory experiment (e.g., Table 5.1). The model simulations were run with the same duration as the laboratory experiment, except for the regular wave conditions which were run for 5 min (corresponding to ~ 300 waves). The wave guides, harbour walls, and gravel slopes were schematised as a porous structure (see Appendix 5.A for a brief description). The impermeable wave guides and harbour walls were schematised with a porosity equal to zero, and the gravel slopes were schematised with a porosity of 0.45, and a characteristic stone size of 2 cm.

In the numerical model, the hull of the ship is represented as a single valued function in $x - y$ space. A panel model of the Panamax ship (Fig. 5.12a) was converted into a single valued function (Fig. 5.12b) by interpolating the panel elements that were located within the waterline contour to the computational grid used in SWASH. Because the ship is represented as a single valued function in $x - y$ space, the bulbous bow of the ship is not included in this schematisation. This model limitation will likely affect the predictions of the hydrodynamic loads that act on the body, as the bulbous bow alters the flow field in the vicinity of the ship (e.g., Bertram, 2012).

Although the set-up of this experiment is relatively simple, it provides a demanding test case for the numerical model as it includes many features that are representative for a real harbour. For example, it includes the reflection and diffraction of waves by the presence of quay walls, and a realistic ship model. Furthermore, the size of the domain and the duration of the simulation are representative for a realistic harbour or

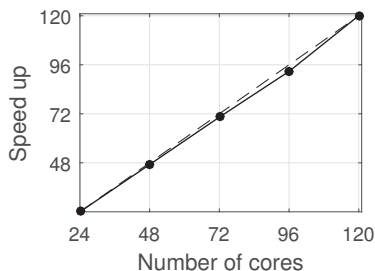


Figure 5.13: Scaling of the Cartesius supercomputer (40960 Intel Xeon cores, 2.4 – 2.6GHz with 64GB internal memory). The line with the markers represents the model speed up. The dashed line illustrates a linear speed up (i.e., if the number of cores is doubled the computational time is halved).

coastal region. At prototype scale, this experimental set-up corresponds to a domain that spans approximately 4×4 km (20 – 30 dominant wave lengths), and a duration of 5 – 7.5 hr (1200 – 2700 dominant wave periods). Given these scales, all simulations of this laboratory experiment were ran with 120 cores on Cartesius, the Dutch national super-computer. The model showed an excellent parallel scaling on Cartesius (Fig. 5.13). The regular wave simulations took on average 4 hr to run, and the irregular wave simulations took on average 32 hr to run. This makes the computational effort significant, but viable on present day multi-processor machines.

5

RESULTS

The model results and measurements are compared based on time series for the regular wave conditions, and based on spectral results for the irregular wave conditions. We compared spectral results for the irregular wave conditions instead of time series as they allow us to gain more insight in the frequency dependence of the wave field and the hydrodynamic loads. In the following, we will focus on the results of the irregular sea states. The results of the two regular wave conditions can be found in Appendix 5.C.

To assess the model performance quantitatively, several bulk parameters were computed: the root-mean-square wave height (H_{rms}) and the mean wave period (T_{m02}) for the wave field, and the bulk load (e.g., $F_{x',rms}$) and mean load period (e.g., $F_{x',m02}$) for the hydrodynamic loads (see Appendix 5.B). Based on these bulk parameters, two statistical measures were computed to quantify the model performance: the relative bias RB and the scatter index SI (see Appendix 5.B). In this work, we qualify the model-data agreement as follows: measures < 15% are considered good, measures between 15% and 30% indicate reasonable agreement, and measures > 30% indicate significant discrepancies.

First, we discuss detailed spectral results of the surface elevation and hydrodynamic loads for two representative simulations. These two simulations represent the results with the best and the worst overall scatter index (SI). This overall SI was computed by averaging the SI over all bulk parameters. The first simulation (case OWi4) corresponds to the lowest SI value (best comparison), and the second (case HBi3) corresponds to the highest SI value (worst comparison).

For the simulation with the lowest scatter index (OWi4), the ship was moored in open

water and subject to a short-crested wave field (Table 5.1). The model reproduced the typical shape and the energy levels of the surface elevation spectra S_ζ near the wavemaker (Fig. 5.14a), except for an over prediction near f_p . This is confirmed by the bulk wave parameters ($|RB| < 0.08$). The predicted and observed wave spectra are comparable to the target wave spectrum (depicted by the dash-dot gray line in Fig. 5.14a). This indicates that the wave field was dominated by the waves generated at the wavemaker, and that the influence of waves reflected at the ship was relatively small. Therefore, these results illustrate that the wavemaker in the model reproduced the wave field that was generated in the laboratory experiment.

The spectral shape of the observed force and moment spectra is similar to S_ζ (Fig. 5.14b-g versus Fig. 5.14a). The predicted force and moment spectra generally agree well with the measurements, especially for the three force components and the pitch moment (M_y). This is confirmed by the low RB values of their bulk parameters ($|RB| < 0.09$), which indicate that they were reproduced with a similar accuracy as that of the wave field. In contrast, the predicted M_x and M_z show bigger discrepancies as their spectral levels are under predicted. Nonetheless, their spectral shape was reproduced well and their bulk parameters were predicted with reasonable accuracy ($|RB| < 0.25$).

In HBi3, the ship was moored inside the harbour and subject to a short-crested wave field (Table 5.1). The predicted spectra and bulk wave parameters agree with the measurements near the wavemaker (Fig. 5.15a). Here, the wave field is dominated by the waves generated at the wavemaker as the spectra compare well with the target wave spectrum. In the harbour basin, the predicted and observed wave spectra and bulk wave parameters are in good agreement ($RB \leq 0.11$), although discrepancies were generally larger compared to the results at the sensors near the wavemaker. Furthermore, the model captured the irregularity of the wave spectra, which is indicative for the occurrence of a (partially) standing wave field. These results show that the model captures the overall wave field in the harbour.

Overall, the spectral shape and the spectral levels were reproduced well for the three force components (Fig. 5.15e-g), including most of the distinct spectral features (e.g., the additional peaks in F'_z , see Fig. 5.15g). The forces on the moored ship were reproduced with larger discrepancies compared to the wave field, although the errors in the bulk parameters were of similar order ($|RB| \leq 0.28$ versus $RB \leq 0.11$). In contrast with the forces, the moments were predicted with significant errors (Fig. 5.15h-j). Only M'_y was reproduced well (Fig. 5.15i), both in terms of the irregular spectral shape and the bulk moment parameters (for which $|RB| \leq 0.13$).

To present the main findings of this test case, Fig. 5.16 and Table 5.2 show a comparison between the predicted and measured bulk parameters for all conditions that were considered. Near the wavemaker, the predicted H_{rms} agree well with the measurements (blue dots in Fig. 5.16a). Inside the harbour basin, the scatter is typically larger (red pluses in Fig. 5.16a). Overall, the model reproduced the wave height with a scatter of 18%. Note that the average RB is smaller than SI, because H_{rms} is both over and under predicted. The outliers in Fig. 5.16a correspond to case HBr (see Fig. 5.C2). The model systematically over predicted T_{m02} with a relatively small bias of 5% (Fig. 5.16b), and there is no clear difference between predictions outside or inside the harbour. Overall, the discrepancies between the predictions and measurements are larger in subset HB

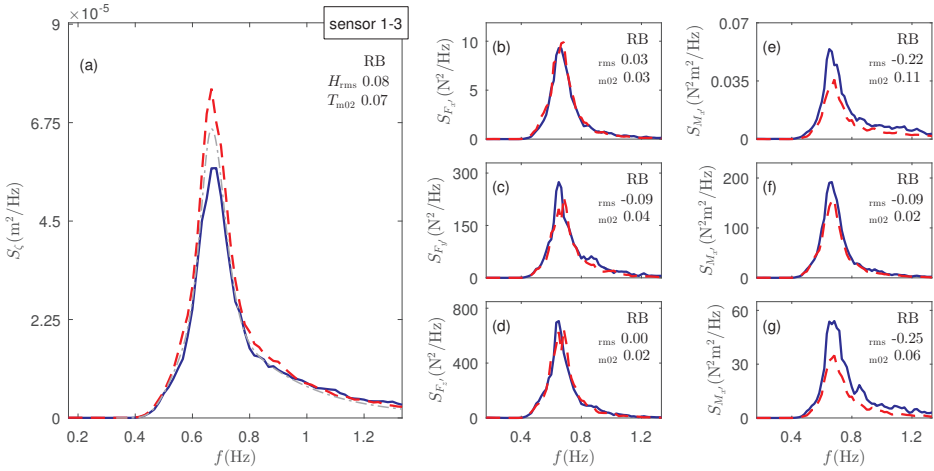


Figure 5.14: Predicted (red line) and observed (blue line) spectra of the surface elevation S_ζ (a), and the forces S_F (b-d) and moments S_M acting on the ship (e-g) for OWi4. The surface elevation spectra plotted in panel (a) is the average of the spectra at sensor 1-3. In panel (a), the thin dash-dot gray line indicates the target JONSWAP spectrum with which the physical and numerical wavemakers were forced. In each panel, the relative bias (RB) of the two bulk parameters are depicted in the top right corner. For brevity, the bulk loads are denoted with rms , and the mean load periods are denoted with m_{02} .

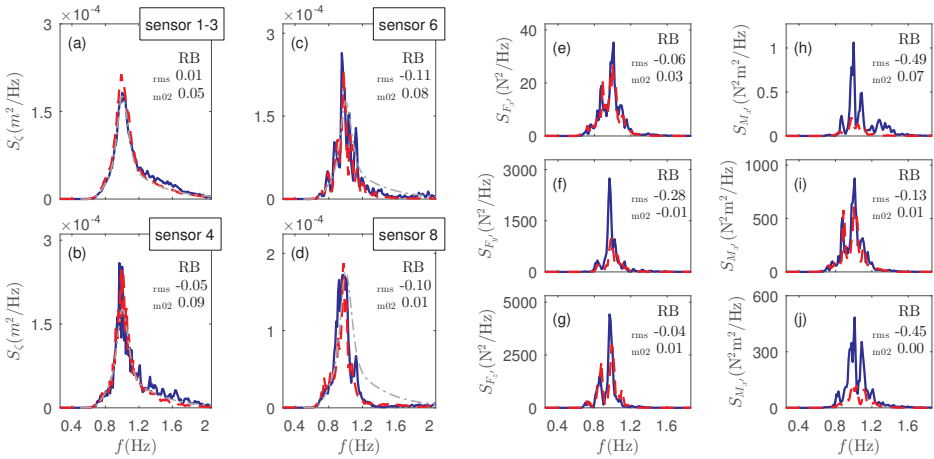


Figure 5.15: Predicted (red line) and observed (blue line) spectra of the surface elevation S_ζ (a-d), and the forces S_F (e-g) and moments S_M acting on the ship (h-j) for HBi3. The plotted surface elevation spectra in panel (a) is the average of the spectra at sensor 1-3. The surface elevation spectra in panel (b-d) are the results at sensors 4, 6, and 8, respectively (see Fig. 5.11 for the sensor positions). In panel (a-d), the thin dash-dot gray line indicates the target JONSWAP spectrum with which the physical and numerical wavemakers were forced. In each panel, the relative bias (RB) of the two bulk parameters are depicted in the top right corner. For brevity, the bulk wave heights and loads are denoted with rms , and the mean wave and load periods are denoted with m_{02} .

than in OW (Table 5.2). This is likely related to the increased complexity of the conditions in subset HB, as a standing wave pattern occurred inside the harbour basin.

The bulk forces and the mean force periods were predicted with an accuracy that is comparable to the wave field (Fig. 5.16c-d). The F'_z and F'_y force components were typically an order of magnitude larger than F'_x , whereas their mean periods were similar. These trends were reproduced well by the model. Overall, F'_z was reproduced with good statistical agreement ($SI \leq 0.05$, see Table 5.2). Discrepancies were larger for the horizontal force components F'_x and F'_y , which were in reasonable agreement with the measurements ($SI \leq 0.12$ and $SI \leq 0.22$, respectively, see Table 5.2). In contrast to the forces, the bulk moments were predicted with significant deviations (Fig. 5.16e), although their mean periods agreed well (Fig. 5.16f). Discrepancies were typically largest for the M'_x and M'_z moment ($SI \leq 0.63$ and $SI \leq 0.39$, respectively), whereas M'_y was reproduced with an SI that is comparable to the forces (see Table 5.2). These findings mirror the results of the individual force components. For example, the error in M'_x (which depends on F'_y and F'_z) is larger than the error in M'_y (which depends on F'_x and F'_z) as the error in F'_y is larger than the error in F'_x (see Table 5.2). These results highlight the sensitivity of the moments to relatively small discrepancies in the force predictions. Although the errors in the predicted moments were significant, the model captured the variation of the bulk moments for the variety of wave conditions that were considered in this work (Fig. 5.16e).

To summarise, these findings show that the wave-induced forces were predicted with an accuracy that is comparable to the wave field, whereas the moments were predicted with more significant discrepancies. This is not surprising given the relatively coarse

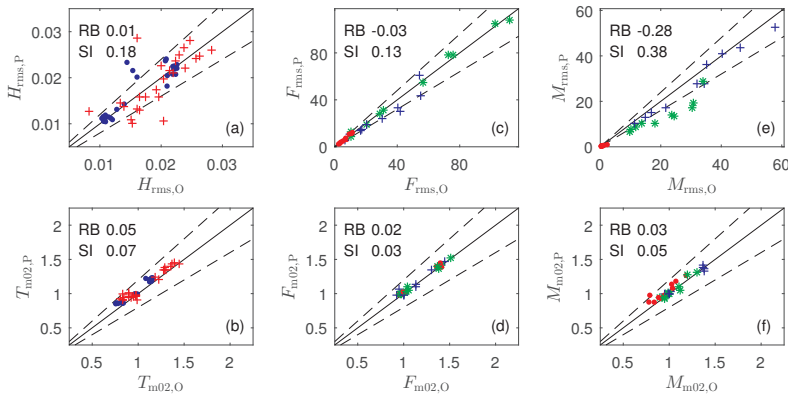


Figure 5.16: Predicted (subscript P) versus observed (subscript O) wave height H_{rms} (a), mean wave period T_{m02} (b), bulk force F_{rms} (c), mean force period F_{m02} (d), bulk moment M_{rms} (e), and mean moment period M_{m02} (f). The solid black line indicates perfect agreement, and the dashed black lines indicate the 20% error bands. In each panel, the overall relative bias (RB) and scatter index (SI) are printed in the top left side. In panel (a) and (b), results of a sensor located outside the harbour are indicated by a blue dot, and results of a sensor located inside the harbour are indicated by a red plus. In panel (c-f), the color and type of the marker indicates the direction of the parameter. That is, a red dot indicates the x' component, a blue plus the y' component, and a green asterisk the z' component.

schematisation of the ship's hull (e.g., the bulbous bow was not included in the simulations), and to difficulties in measuring the moments that act on a restrained ship (e.g., Van der Molen, 2006). Overall, the results of this test case demonstrate the potential of the model in seamlessly simulating the wave field in the basin, their interactions with the restrained ship, and the resulting hydrodynamic loads that act on the body.

Table 5.2: Statistical measures (relative bias RB, and scatter index SI) of the wave parameters (significant wave height and mean wave period), and the hydrodynamic loads (forces and moments) for the simulations with a ship moored in open water (OW), a ship moored inside a harbour basin (HB), and for all simulations combined (Overall).

	OW		HB		Overall	
	RB	SI	RB	SI	RB	SI
H_{rms}	0.02	0.12	0.01	0.19	0.01	0.18
$T_{\text{m}02}$	0.06	0.07	0.05	0.07	0.05	0.07
$F_{x',\text{rms}}$	-0.09	0.14	0.07	0.10	0.02	0.12
$F_{y',\text{rms}}$	-0.10	0.14	-0.13	0.20	-0.12	0.22
$F_{z',\text{rms}}$	-0.01	0.07	0.01	0.04	0.00	0.05
$M_{x',\text{rms}}$	0.22	0.24	-0.48	0.59	-0.42	0.63
$M_{y',\text{rms}}$	-0.16	0.19	-0.05	0.08	-0.09	0.11
$M_{z',\text{rms}}$	-0.34	0.44	-0.34	0.36	-0.34	0.39
$F_{x',\text{m}02}$	0.02	0.02	0.01	0.02	0.01	0.02
$F_{y',\text{m}02}$	0.04	0.05	-0.01	0.02	0.02	0.04
$F_{z',\text{m}02}$	0.03	0.03	0.01	0.01	0.02	0.02
$M_{x',\text{m}02}$	0.11	0.12	0.06	0.06	0.08	0.10
$M_{y',\text{m}02}$	0.01	0.02	0.00	0.03	0.01	0.02
$M_{z',\text{m}02}$	0.03	0.04	-0.02	0.04	0.00	0.04

5.7. DISCUSSION

This paper presents a new numerical approach to simulate the nonlinear evolution of waves and their impact on a restrained ship at the scale of a realistic harbour or coastal region. This model is based on the non-hydrostatic approach, and the SWASH model in particular, which is in essence a direct numerical implementation of the RANS equations. The use of the Keller-Box scheme to discretise the non-hydrostatic pressure allows such models to efficiently resolve a range of nearshore wave and flow phenomena. To include the interactions between the waves and the ship, we developed a new method to account for the presence of a floating body in the non-hydrostatic approach. The findings of this work demonstrated that the model captures the scattering of regular waves and a solitary wave by a rectangular pontoon. Furthermore, the model gave a reasonable prediction of the magnitude and periodicity of the hydrodynamic loads on a restrained container ship for a range of realistic wave conditions. Most importantly, this work demonstrated that a coarse vertical resolution sufficed to capture these interactions, which highlights that the model retains this favourable property of the non-hydrostatic approach when a floating body is included.

Compared to the variety of models that have been developed to solve the wave-ship

interactions (e.g., Newman, 2005; Hadžić et al., 2005; Yan and Ma, 2007; Bouscasse et al., 2013), the primary advantage of the present approach is that it does not rely on predictions of the wave field in the vicinity of the moored ship. To date, the most advanced methodology that was developed to solve both the evolution of waves and their impact on a moored ship coupled a wave model based on the Boussinesq or non-hydrostatic approach with a panel model (Bingham, 2000; Van der Molen and Wenneker, 2008; Dobrochinski, 2014). This coupled approach includes a detailed schematisation of the ship's hull, but is restricted to relatively mild wave conditions, whereas the present approach makes no a-priori assumptions concerning the nonlinearity of the wave field, but is limited to a relatively coarse ship schematisation. Although a direct comparison between these two methods was not the subject of this work, we can make an indirect comparison based on the work of Dobrochinski (2014). In this study, a coupled model (combining SWASH and a panel model) was validated for several wave conditions belonging to the same laboratory experiment that was considered in the present work (§5.6). Overall, the discrepancies in the hydrodynamic load predictions of this coupled model are comparable to the results presented here (§5.6). This suggests that the accuracy of these two methods is similar for these experimental conditions.

The key features of the present approach are thus that (i) it can relatively efficiently resolve the evolution of waves in coastal waters (Zijlema et al., 2011; Smit et al., 2013, 2014), including the infragravity waves which are known to disrupt harbour operations (Rijnsdorp et al., 2014, 2015a; De Bakker et al., 2016), and (ii) that it can seamlessly account for the interactions between the waves and a restrained ship. This demonstrates that the model provides a promising new alternative to simulate the nonlinear evolution of waves and their impact on a restrained ship at the scale of a harbour or coastal region. Based on these considerations, we believe that this work provides a crucial first step towards the development of a new approach to simulate the wave-induced response of a ship that is moored in coastal waters.

So far, the model was used to simulate the wave impact on a restrained ship under idealised conditions (e.g., relatively mild waves, and a relatively simple harbour layout). Further research is therefore required to push the capabilities of the approach towards more realistic conditions. This includes an assessment of the model capabilities for more challenging environments, for example, in a complex coastal region or in the case of significant nonlinear wave effects. Furthermore, future work can be undertaken to resolve the actual wave-induced motions of a moored ship, and to improve the accuracy of the model in resolving the wave-ship interactions. In this study, the model was applied with a relatively coarse vertical resolution, which permits applications at relatively large scale. On the other hand, this implies that the model does not resolve the details of the vertical flow structure in the vicinity of the ship, which are likely important in the case of energetic wave conditions (or significant ship motions) when turbulent effects are significant. Given the flexibility of the non-hydrostatic approach (in contrast to the coupled wave-panel methodology), resolving such features merely requires an increase of the vertical resolution near the ship combined with the use of a proper turbulence model. For example, by implementing a domain decomposition technique, the model can retain its favourable features in simulating nonlinear waves at large scales, while it at the same time can resolve the vertical flow structure in the vicinity of the moored ship.

APPENDICES

5.A. POROUS FLOW

To account for the flow through a porous structure, the governing equations are adapted in accordance with Madsen (1983). In SWASH, only the global continuity and the horizontal momentum equation are adapted to include the effect of the flow through a porous structure, whereas the vertical momentum equation is not adapted. Although an inclusion of the porous influence in the vertical momentum equation is likely more accurate (e.g., Higuera et al., 2014; Ma et al., 2014a; Jacobsen et al., 2015), we are not primarily interested in the flow through a porous medium. We merely mimic the dissipation induced by a gravel beach, and the reflections induced by impermeable walls, for which this approach is expected to be sufficiently accurate.

The modified equations in the outer domain read,

$$\begin{aligned} n \frac{\partial \zeta}{\partial t} + \frac{\partial HU}{\partial x} &= 0, \\ \frac{\partial u_n}{\partial t} + \frac{\partial u_n u_n}{\partial x} + \frac{\partial w u}{\partial z} &= -g \frac{\partial \zeta}{\partial x} - \frac{\partial p}{\partial x} + \frac{\partial \tau_{xx}}{\partial x} + \frac{\partial \tau_{xz}}{\partial z} - f_l u - f_t u |u|, \end{aligned}$$

where n is the porosity, $u_n (= \frac{u}{n})$ is the seepage velocity inside a porous medium, f_l is a laminar friction factor, and f_t is a turbulent friction factor. The friction factors are given by (e.g., Madsen, 1983),

$$\begin{aligned} f_l &= \alpha_e \frac{(1-n)^3}{n^2} \frac{v}{D}, \\ f_t &= \beta_e \frac{1-n}{n^3} \frac{1}{D}, \end{aligned}$$

where v is the kinematic viscosity of water, D is a characteristic stone size, and α_e and β_e are empirical coefficients. In this study, the empirical coefficient were set at their default values ($\alpha_e = 1000$, and $\beta_e = 2.8$).

5.B. QUANTITATIVE MODEL-DATA COMPARISON

BULK PARAMETERS

To quantify the model performance for the laboratory experiment of §5.6, we computed several bulk parameters that represent the wave conditions inside the laboratory basin, and the hydrodynamic loads that act on the ship. We characterise the wave conditions using the root mean square wave height $H_{\text{rms}} = \sqrt{8m_0}$ and the mean wave period $T_{\text{m}02} = \sqrt{m_0/m_2}$, in which $m_n = \int f^n S_\zeta(f) df$, and $S_\zeta(f)$ is the surface elevation spectrum. The H_{rms} provides a measure of the total wave energy, and $T_{\text{m}02}$ provides a measure of the

mean wave period. Furthermore, T_{m02} gives some information on the frequency distribution of the wave energy. Similar to the bulk wave parameters, we computed bulk parameters for the hydrodynamic loads to gain insight in the overall forces and moments acting on the ship. The bulk parameters were computed for each individual component, following the same methodology as the wave height and the mean wave period. For example, the bulk force in x' direction is computed as $F_{x',rms} = \sqrt{8m_0}$, in which $m_0 = \int S_{F_{x'}}(f)df$, and $S_{F_{x'}}$ is the spectrum of $F_{x'}$. All spectra were computed with 60 degrees of freedom, based on ensemble averaged Fourier-transforms of detrended and windowed signals. To account for the spin-up time of the model and the measurements, the first 80 s of the signals was excluded in the case of a regular wave experiment, and the first 120 s were excluded in the case of an irregular wave experiment (see §5.6 for a description of the experiments).

STATISTICAL MEASURES

We quantified the model performance with two statistical measures: the relative bias, and the scatter index. The relative bias is computed as,

$$RB = \frac{\sum_{i=1}^N (Q_p^i - Q_o^i)}{\sum_{i=1}^N Q_o^i}, \quad (5.B1)$$

and the scatter index is computed as,

$$SI = \frac{\sqrt{\frac{1}{N} \sum_{i=1}^N (Q_p^i - Q_o^i)^2}}{\frac{1}{N} \sum_{i=1}^N Q_o^i}, \quad (5.B2)$$

where Q_p is a predicted parameter, and Q_o is an observed parameter in a sample of size N . We computed these statistical measures for the parameters of several groups of simulations. In total we considered three groups, of which one represents all simulations, and of which the two others represent the two simulation subsets (OW and HB). The measures were computed for each bulk parameter of the forces and moments (e.g., $F_{x',rms}$), by taking the summation over the simulations belonging to a group (i.e., $N = 5$ for group OW and HB, and $N = 10$ for the group that contains all simulations). For the wave heights and mean periods, the measures were computed by taking the summation over all available wave measurements in the group.

5.C. REGULAR WAVE IMPACT ON A CONTAINER SHIP

OPEN WATER

First, we compare predictions and measurements of the surface elevation and hydrodynamic loads for OWr, in which the moored ship was subject to a monochromatic wave. In this experiment, the first waves arrived at the wave sensors after approximately 10 s (Fig. 5.C1a-c), and about 10 s later they reached the moored ship (Fig. 5.C1d-i). The signals

are roughly sinusoidal for $t > 60$ s, which indicates that the conditions became approximately stationary. Due to the orientation of the ship with respect to the wave direction, the sway force ($F_{y'}$) is slightly larger compared to the surge force ($F_{x'}$). Furthermore, the pitch and yaw moment ($M_{y'}$ and $M_{z'}$, respectively) are an order of magnitude larger compared to the roll moment ($M_{x'}$). Note that the $M_{x'}$ signal is relatively noisy, as its measurements suffer from significant inaccuracies (e.g., Van der Molen, 2006).

The model reproduced the typical surface elevation signal at the wave sensors (Fig 5.C1a-c), and the predicted wave height and wave period were in reasonable agreement with the measurements ($|RB| \leq 0.27$). The agreement appears best at the start of the simulation ($t < 30$ s), when the wave field at the sensors was progressive. This illustrates that the model reproduced the monochromatic wave that was generated at the numerical wavemaker. For $t > 30$ s, discrepancies between the predicted and observed surface elevation signals can be observed at all wave sensors. At this time, the waves that were reflected at the ship and at the wave guides reached the wavemaker and were (partly) absorbed. These discrepancies are in part related to errors in the scattering of waves at the ship, and to differences between the absorption characteristics of the physical and numerical wavemaker.

The discrepancies between the predicted and measured load signals are typically larger compared to the surface elevation signals, especially for $M_{z'}$ (which is under predicted with 44%, see Fig. 5.C1i). Furthermore, the predicted signals are shifted in time with respect to the measurements. Applying the same time shift of -0.35 s to all load signals (illustrated by the dash-dot gray line in the insets of Fig. 5.C1d-i), the phases of the predicted loads are comparable to the measurements. This shows that the predicted hydrodynamic loads experience the same phase shift, indicating that the relative phasing of the individual load components is correct. The negative phase difference, which is only a small fraction of the time required for the waves to reach the moored ship ($\sim 4\%$), cannot be explained by the error in the numerical wave celerity. Although the actual reason remains unclear, we hypothesise that this time shift (or spatial shift)² is related to a difference between the position of the ship in the laboratory and in the numerical model, and the relatively coarse schematisation of the hull (e.g., the bulbous bow is excluded in the model). However, the model reproduced the global arrival time of the waves at the ship as the load signals become non-zero at approximately the same moment in time (Fig 5.C1d-i). Furthermore, the model captured the order of magnitude and the periodicity of the individual load components, including their mutual dependence (e.g., $M'_x \ll M'_{y'}$, and $M'_{y'} \sim M'_{z'}$).

HARBOUR BASIN

In HBr, the ship which is moored inside the rectangular harbour basin is subject to the same monochromatic wave as in OWr. Near the wavemaker, the predicted surface elevation signal compares well with the measurements for $t < 25$ s, when the (progressive) wave field at the sensors was not yet disturbed by the waves reflected at the gravel slopes in front of the harbour walls, the wave guides, and the wavemaker (Fig. 5.C2a). For $t > 25$ s, the predicted and observed signal became relatively stationary and the wave height is consistently over predicted (likely due to differences in the wave damping that is induced

²A time shift of 0.35 s is equivalent to a wave propagation distance of ~ 0.4 m

by the gravel slopes located in front of the harbour walls).

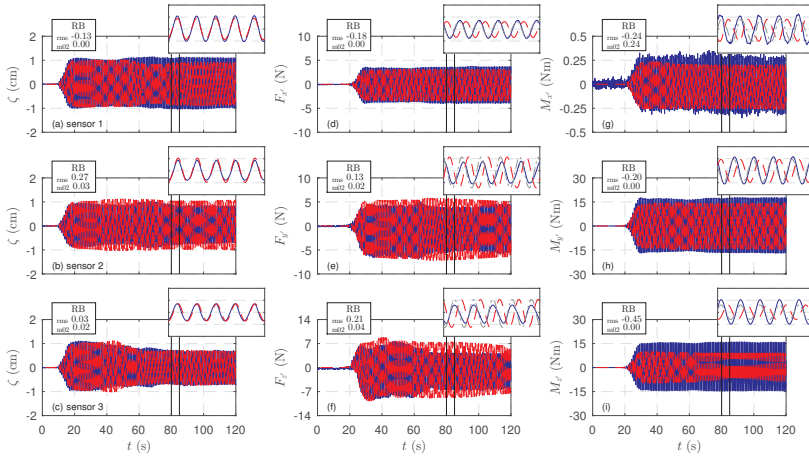


Figure 5.C1: Predicted (dashed red line) and observed (blue line) time series of the surface elevation ζ (a-c), and the forces F (d-f) and moments M acting on the ship (g-i) for the first two minutes of simulation OWr. The insets adjacent to the main panels show a close up of the results for $80 \leq t \leq 85$ s (illustrated by the two vertical black lines in the main panels). To facilitate a comparison between the predicted and observed hydrodynamic load signals, the dash-dot gray line in the insets of (d-i) shows the predicted hydrodynamic load signal including a time shift of -0.35 s. In each panel, the relative bias (RB) of the two bulk parameters are depicted in the top left corner. In panel (a-c), the RB of the wave height H_{rms} and the mean wave period T_{m02} are shown. In panel (d-i), the RB of the bulk hydrodynamic loads (e.g., $F_{x',rms}$) and the mean load period of the loads (e.g., $F_{x',m02}$) are shown. For brevity, the bulk loads are denoted with $_{rms}$, and the mean load periods are denoted with $_{m02}$. Note that in this case the scatter index is equal to the absolute value of RB.

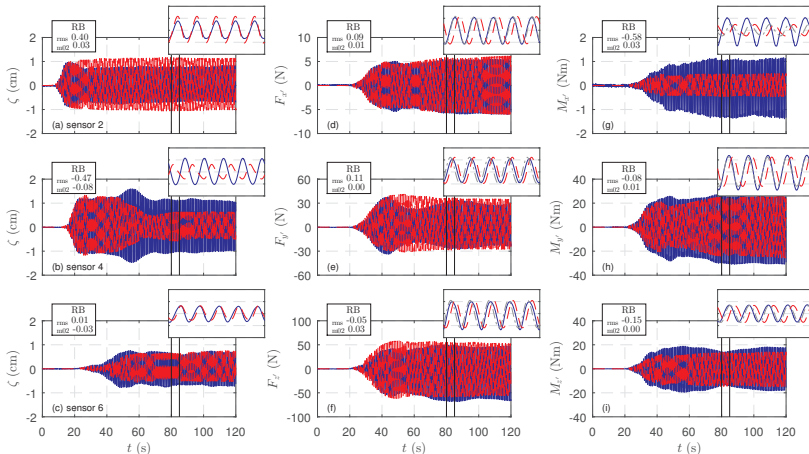


Figure 5.C2: Predicted (dashed red line) and observed (blue line) time series of the surface elevation ζ (a-c), and the forces F (d-f) and moments M acting on the ship (g-i) for HBr. To facilitate a comparison between the predicted and observed hydrodynamic load signals, the dash-dot gray line in the insets of (d-i) shows the predicted hydrodynamic load signal including a time shift of -0.23 s. See Fig. 5.C1 for a further description.

Near the harbour entrance and inside the harbour basin, a (partially) standing wave field occurred due to wave reflections at the harbour walls and wave guides. Here, the conditions became approximately stationary for $t > 80$ s (see Fig. 5.C2b-i). Near the harbour entrance at sensor 4, the predicted wave field differs in magnitude and phase compared to the measurements (Fig. 5.C2b), whereas the predicted wave field agrees well at sensor 6 which is located inside the harbour (Fig. 5.C2c). On average, the discrepancies in the predicted wave field are larger compared to the results of OWr. This is likely due to the increased complexity of the conditions in subset HB due to the partial reflections at the gravel slopes and the occurrence of a standing wave field inside the harbour. Differences between the physical and numerical domain (e.g., due to the discretisation of the harbour) and small errors in the numerical phase velocity may not only result in phase differences, but also in amplitude differences between the predicted and observed wave field (possibly explaining the differences observed at sensor 4).

The wave field near the harbour entrance (sensor 4) and inside the harbour basin (sensor 6), and the wave-induced loads acting on the moored ship became approximately stationary after $t > 60$ s (Fig. 5.C2b-i).

Despite the errors in the predicted wave field inside the harbour, the model reproduced the forces and moments that act on the ship (Fig. 5.C2d-i); except for $M'_{x'}$, and a phase difference between the measured and predicted load signals. Similar to OWr, a constant time shift approximately corrects for the phase difference of all individual load components but $M'_{x'}$. The errors in $M'_{x'}$ suggest that relatively small discrepancies in the force components (in this case, $|RB| \leq 0.11$ for F'_y and F'_z) can cause significant discrepancies in the moment ($|RB| \leq 0.58$ for $M'_{x'}$).

6

CONCLUSIONS AND OUTLOOK

This thesis set out to develop a new modelling approach to predict the wave-induced response of a ship that is moored in coastal waters based on an offshore wave climate. Such predictions require that the model captures both the nearshore wave evolution at the scale of a realistic harbour or coastal region, and the interactions between the waves and the moored ship. The numerical methodology that was adopted in this work is based on the recently developed non-hydrostatic wave-flow model SWASH. This thesis pursues a further development and verification of the SWASH model in (i) simulating the non-linear wave dynamics in a coastal environment (Chapter 3 and 4), and (ii) simulating the interactions between the waves and a restrained ship (Chapter 5). The following presents an overview and discussion of the main conclusions of this thesis, and an outlook for future developments.

6.1. CONCLUSIONS

In coastal waters, the response of a moored ship is not only determined by the short waves, which typically dominate the nearshore wave field, but also by infragravity waves, which are generated through nonlinear interactions amongst pairs of short waves. Although infragravity waves typically have amplitudes which are an order of magnitude smaller compared to the short waves, their relatively low frequencies may align with the natural frequency of a mooring system or harbour basin. The presence of infragravity waves may thus lead to significant response of a moored ship, which adversely affects its operability. Accurate predictions of the nonlinear wave field are therefore essential to ensure safe and continuous operations of a moored ship.

Conceptually, non-hydrostatic models like SWASH capture the key physical processes that affect the wave field in a coastal environment as they are essentially a direct numerical implementation of the RANS equations. In contrast with models that are based on simplifications of these basic equations (like mild slope and Boussinesq models), the accuracy with which non-hydrostatic models resolve these processes primarily depends on the spatial and temporal resolution. The combination of shock capturing numerics

and an efficient numerical technique to account for the non-hydrostatic pressure allows them to efficiently capture the key wave dynamics, especially compared to other RANS based models (e.g., the VOF approach). Amongst others, previous studies showed that non-hydrostatic models like SWASH capture the nonlinear dynamics of short waves in a coastal region (e.g., Ma et al., 2012; Smit et al., 2013, 2014). However, such studies did not address if they can resolve the nearshore evolution of the infragravity waves. Given their importance with respect to the response of moored ships, this work evaluated the potential of the non-hydrostatic approach to resolve the evolution of infragravity waves in a coastal environment.

For this purpose, SWASH was used to simulate the infragravity wave dynamics in both a wave flume and a natural environment. First, the model was used to reproduce two flume experiments (Boers, 1996; Van Noorloos, 2003), to study if it captures the cross-shore evolution of infragravity waves (Chapter 3). These flume experiments cover a range of wave conditions, for which the infragravity wave evolution showed distinct differences. For example, relatively long infragravity waves experienced a mild energy increase as they propagated shoreward, and were nearly fully reflected at the shoreline. In contrast, relatively short infragravity waves experienced a strong energy increase, whereas they almost fully dissipated close to the shoreline. For all conditions, the model captured the bulk wave parameters of the short waves and the infragravity waves with a coarse vertical resolution (2 layers), including the heights of the shoreward and seaward directed infragravity waves. Furthermore, it reproduced the bulk dissipation of the infragravity waves close to the shoreline, including the steepening and eventual breaking of the infragravity waves (which occurred for the dissipative infragravity conditions). Remarkably, the agreement between the predicted and measured bulk wave parameters is comparable to the more involved computations of Torres-Freyermuth et al. (2010), who used a VOF model with 82 cells in the vertical.

Although the good agreement between the model and the flume experiments demonstrated that the model captures the (frequency dependent) cross-shore evolution of infragravity waves in coastal waters, it remained an open question if the model captures their dynamics in the field. In Chapter 4, SWASH was used to study the infragravity wave dynamics at a sandy beach located near Egmond aan Zee (the Netherlands). This field site is characterised by a complex nearshore bottom topography (a double barred beach). A total of six sea states were reproduced with the model (ranging from mild to storm conditions), which were measured as part of a two month measurement campaign (conducted from October to November 1998). For all conditions, the predicted wave field represented the natural conditions that were measured at the field site. A unique feature of such model predictions is their extensive spatial coverage, which allows for analysis of the wave dynamics at scales not easily instrumented by in-situ measurement devices. In this manner, the model can be used to improve our understanding of the complex nearshore wave dynamics. Particularly, this allowed for a quantification of the processes that affect the nearshore infragravity energy balance (e.g., topographic trapping, nonlinear interactions, and the nearshore dissipation). For example, this study highlighted that up to 50% of the infragravity wave motion can be trapped at a bar.

Overall, the findings of the flume and field studies show that the model can resolve the key dynamics that govern the (infragravity) wave field in coastal waters with a coarse

vertical resolution, permitting applications at the scale of a realistic harbour or coastal region. These results illustrate that SWASH is a powerful tool to predict the nonlinear wave field at a coastal berth based on an offshore wave climate. To simulate the resulting wave-induced response of a moored ship, the model has to account for the interactions between the waves and the floating body. As non-hydrostatic models are based on the RANS equations, they can be naturally extended to account for the presence of a floating body. In this manner, the model can intrinsically account for the interactions between the waves and a moored ship.

In Chapter 5, a non-moving floating body was included in the SWASH model to account for the interactions between the waves and a restrained ship (i.e., the scattering of waves by a fixed floating body). To verify this approach, model predictions were compared with four test cases: An analytical solution, a numerical solution, and two laboratory campaigns. These test cases demonstrated that the model captures the scattering of both solitary and regular waves by a fixed rectangular pontoon. Furthermore, the model gave a reasonable prediction of the hydrodynamic loads for a more complex laboratory experiment, in which a realistic container ship was subject to a range of wave conditions (including realistic short-crested sea states). Remarkably, the model captured these dynamics with a coarse vertical resolution (2 layers). In fact, for one of the test cases, the results were nearly identical compared to the solution of a high resolution non-hydrostatic model. These findings illustrate that – by including a fixed floating body in the SWASH model – a relatively efficient tool has been developed to resolve both the evolution of waves and their interactions with a restrained ship.

6.2. OUTLOOK

In this thesis, a new numerical model has been developed to simulate the evolution of waves and their impact on a moored ship in a realistic coastal environment. The key features of this approach are that it seamlessly accounts for the evolution of waves – including the infragravity waves – and their interactions with a restrained ship, and that it makes no a-priori assumptions on the characteristics of the wave field. As such, the model can be seen as an intermediate approach that is positioned between the combined wave-panel models and the high resolution RANS models.

Compared to the wave-panel models (Bingham, 2000; Van der Molen and Wenneker, 2008; Dobrochinski, 2014), a marked advantage of the present approach is that it captures both the propagation of waves and their impact on a moored ship, removing the necessity to use a near field model to simulate the wave-ship interactions. Furthermore, such coupled models have – to date – relied on panel models based on linear potential theory, which limits their validity to conditions in which the wave nonlinearity is small (e.g., Bingham, 2000). In contrast, the non-hydrostatic approach is in principle applicable for any type of sea state, as it makes no assumptions on the wave characteristics. This work further showed that a relatively coarse resolution was sufficient to capture the scattering of waves by a moored ship. Such coarse resolutions make this a relatively efficient approach, especially compared to more detailed RANS models (e.g., Torres-Freyermuth et al., 2010; Hadžić et al., 2005), permitting applications at the scale of a realistic harbour or coastal region.

In this work, simulations of the wave-ship interactions were however restricted to

idealised conditions and a relatively simple harbour layout (e.g., a wave basin of constant depth, and a rectangular harbour), in which the wave-induced loads were dominated by the short-wave field. Further research is required to verify whether the model captures the wave-ship interactions in a complex coastal environment, and in the case of significant nonlinear wave effects (e.g., in the case of energetic infragravity waves). In particular, one of the open question that remains is whether the model can resolve the wave-ship interactions with a coarse vertical resolution in the case of energetic wave conditions.

Naturally, a coarse vertical resolutions implies that the model does not resolve the details of the flow field in the vicinity of the moored ship. Although this work showed that the dominant interactions between the waves and a restrained ship are well captured with such coarse resolutions, this likely becomes restrictive in situations of large wave impacts, when turbulent effects become significant. In such conditions, finer vertical resolutions or more involved models like the high resolution RANS models (e.g., Hadžić et al., 2005; Wilson et al., 2006; Mousaviraad et al., 2016) are likely required to resolve the turbulent flow field in the vicinity of the moored ship. In this respect, a key feature of the non-hydrostatic approach is that it merely requires an increase of the number of vertical layers, combined with the use of an appropriate turbulence model, to simulate the detailed flow field in the vicinity of the moored ship. Naturally, this comes at the expense of an increase in the computational effort, which – at present – restricts such applications to small spatial and temporal scales. To relax this limitation, an interesting future development would be to vary the vertical resolution inside the domain, by increasing the number of layers in regions where more details of the flow field are required (e.g., in the vicinity of the ship). With such a domain decomposition, an optimal balance can be found in simulating the nearshore evolution of waves at relatively large scales, while resolving the detailed flow field in the vicinity of the moored ship.

Besides improving the accuracy of the model, a second development is to advance its capabilities towards simulating the wave-induced motions of a moored ship. For this purpose, the model needs to be extended with the equations that govern the motions of a floating body. These equations follow from Newton's second law of motion: $\mathbf{F} = m\mathbf{a}$, where \mathbf{F} is an external force composed of several contributions (e.g., the hydrodynamic loads, and the forces induced by a mooring system), m is the mass of the body, and \mathbf{a} is the acceleration of the body. Additionally, to account for the impact of a moving ship on the fluid (e.g., the radiation of waves), the boundary conditions at the ship's hull have to include the motions of the ship. Conceptually, this development allows the model to simulate the wave-induced response of a moored ship, as it accounts for the scattering and the radiation of waves induced by the floating body.

The foregoing illustrates that further work is required to advance the capabilities of the model to simulate the wave-induced response of a moored ship based on an off-shore wave climate. Nonetheless, the findings of this study demonstrate that the non-hydrostatic approach provides a promising alternative to solve this challenging problem. Although the use of such models at the scale of a realistic harbour or coastal region requires a significant computational effort, the ever increasing computational powers will eventually make their application viable for both scientific and (routine) engineering purposes. Such developments will promote the use of the non-hydrostatic approach in

simulating, for example, the wave agitation in a harbour and the wave-induced response of a moored ship, in favour of more approximate methods like mild slope models and the coupled wave-panel model. In this context, this thesis sets the stage for future developments that will push the non-hydrostatic approach towards such realistic applications in complex coastal environments.

BIBLIOGRAPHY

- Abbott, M. B., Petersen, H. M., and Skovgaard, O. (1978): On the numerical modelling of short waves in shallow water. *Journal of Hydraulic Research*, 16 (3), 173–204.
- Ai, C., and Jin, S. (2012): A multi-layer non-hydrostatic model for wave breaking and run-up. *Coastal Engineering*, 62, 1–8.
- Ai, C., Jin, S., and Lv, B. (2011): A new fully non-hydrostatic 3D free surface flow model for water wave motions. *International Journal for Numerical Methods in Fluids*, 66 (11), 1354–1370.
- Bai, Y., and Cheung, K. F. (2012): Depth-integrated free-surface flow with a two-layer non-hydrostatic formulation. *International Journal for Numerical Methods in Fluids*, 69 (2), 411–429.
- Bai, Y., and Cheung, K. F. (2013): Depth-integrated free-surface flow with parameterized non-hydrostatic pressure. *International Journal for Numerical Methods in Fluids*, 71 (2), 403–421.
- Barrett, R., et al. (1994): *Templates for the Solution of Linear Systems: Building Blocks for Iterative Methods*. SIAM, Philadelphia, 112 pp.
- Battjes, J. A. (1994): Shallow water wave modelling. In: *International Symposium on Waves - Physical and Numerical Modelling*, University of British Columbia, 1–24.
- Battjes, J. A., Bakkenes, H. J., Janssen, T. T., and Van Dongeren, A. R. (2004): Shoaling of subharmonic gravity waves. *Journal of Geophysical Research*, 109 (C2).
- Battjes, J. A., and Janssen, J. P. F. M. (1978): Energy loss and set-up due to breaking of random waves. In: *Coastal Engineering Proceedings*, ASCE, 569–587.
- Beck, R., and Reed, A. (2001): Modern seakeeping computations for ships. In: *Twenty-Third Symposium on Naval Hydrodynamics*, 1–45.
- Berkhoff, J. C. W. (1972): Computation of combined refraction – diffraction. In: *Coastal Engineering Proceedings*, ASCE, 471–490.
- Bertram, V. (2012): *Practical Ship Hydrodynamics*. Elsevier.
- Bijleveld, H. J. M. (2004): Projectbeschrijving R&D Haves EZ-LIP: H3896.40 Validatie golfkrachten op schepen. Tech. rep., WL | Delft Hydraulics.
- Bingham, H. B. (2000): A hybrid Boussinesq-panel method for predicting the motion of a moored ship. *Coastal Engineering*, 40 (1), 21–38.

- Boers, M. (1996): Simulation of a surf zone with a barred beach; report 1: Wave heights and wave breaking. Tech. rep., Delft University of Technology.
- Bonneton, P., Barthelemy, E., Chazel, F., Cienfuegos, R., Lannes, D., Marche, F., and Tissier, M. (2011): Recent advances in Serre-Green Naghdi modelling for wave transformation, breaking and runup processes. *European Journal of Mechanics - B/Fluids*, 30 (6), 589–597.
- Booij, N., Ris, R. C., and Holthuijsen, L. H. (1999): A third-generation wave model for coastal regions: 1. Model description and validation. *Journal of Geophysical Research*, 104 (C4), 7649–7666.
- Bouscasse, B., Colagrossi, A., Marrone, S., and Antuono, M. (2013): Nonlinear water wave interaction with floating bodies in SPH. *Journal of Fluids and Structures*, 42, 112–129.
- Bowers, E. C. (1977): Harbour resonance due to set-down beneath wave groups. *Journal of Fluid Mechanics*, 79 (1), 71–92.
- Brocchini, M. (2013): A reasoned overview on Boussinesq-type models: the interplay between physics, mathematics and numerics. *Proceedings of the Royal Society A: Mathematical, Physical and Engineering Sciences*, 469 (2160).
- Bromirski, P. D., Sergienko, O. V., and MacAyeal, D. R. (2010): Transoceanic infragravity waves impacting Antarctic ice shelves. *Geophysical Research Letters*, 37 (2).
- Brugnano, L., and Casulli, V. (2009): Iterative solution of piecewise linear systems and applications to flows in porous media. *SIAM Journal on Scientific Computing*, 31 (3), 1858–1873.
- Bryan, K. R., and Bowen, A. J. (1996): Edge wave trapping and amplification on barred beaches. *Journal of Geophysical Research*, 101 (C3), 6543–6552.
- Bryan, K. R., and Bowen, A. J. (1998): Bar-trapped edge waves and longshore currents. *Journal of Geophysical Research*, 103 (C12), 27 867–27 884.
- Bryan, K. R., Howd, P. A., and Bowen, A. J. (1998): Field observations of bar-trapped edge waves. *Journal of Geophysical Research*, 103 (C1), 1285–1305.
- Carrica, P. M., Castro, A. M., and Stern, F. (2010): Self-propulsion computations using a speed controller and a discretized propeller with dynamic overset grids. *Journal of Marine Science and Technology*, 15 (4), 316–330.
- Carrica, P. M., Wilson, R. V., and Stern, F. (2006): Unsteady RANS simulation of the ship forward speed diffraction problem. *Computers & Fluids*, 35 (6), 545–570.
- Casulli, V., and Stelling, G. S. (1998): Numerical simulation of 3D quasi-hydrostatic, free-surface flows. *Journal of Hydraulic Engineering*, 124 (7), 678–686.
- Casulli, V., and Stelling, G. S. (2013): A semi-implicit numerical model for urban drainage systems. *International Journal for Numerical Methods in Fluids*, 73 (6), 600–614.

- Cavaleri, L., et al. (2007): Wave modelling – The state of the art. *Progress in Oceanography*, 75 (4), 603–674.
- Chawla, A., Özkan-Haller, H. T., and Kirby, J. T. (1998): Spectral model for wave transformation and breaking over irregular bathymetry. *Journal of Waterway, Port, Coastal, and Ocean Engineering*, 124 (4), 189–198.
- Chen, Q., Dalrymple, R. A., Kirby, J. T., Kennedy, A. B., and Haller, M. C. (1999): Boussinesq modeling of a rip current system. *Journal of Geophysical Research*, 104 (C9), 20 617–20 637.
- Chen, Q., Kirby, J. T., Dalrymple, R. A., Shi, F., and Thornton, E. (2003): Boussinesq modeling of longshore currents. *Journal of Geophysical Research*, 108 (C11).
- Chorin, A. J. (1968): Numerical solution of the Navier-Stokes equations. *Mathematics of Computation*, 22 (104), 745–745.
- Cienfuegos, R., Barthélemy, E., and Bonneton, P. (2010): Wave-breaking model for Boussinesq-type equations including roller effects in the mass conservation equation. *Journal of Waterway, Port, Coastal, and Ocean Engineering*, 136 (1), 10–26.
- Clark, D. B., Elgar, S., and Raubenheimer, B. (2012): Vorticity generation by short-crested wave breaking. *Geophysical Research Letters*, 39 (24).
- Cointe, R., Geyer, P., King, B., Molin, B., and Tramoni, M. (1991): Nonlinear and linear motions of a rectangular barge in a perfect fluid. In: *Naval Hydrodynamics Proceedings*, NAP, 85–99.
- Cui, H., Pietrzak, J. D., and Stelling, G. S. (2012): Improved efficiency of a non-hydrostatic, unstructured grid, finite volume model. *Ocean Modelling*, 54-55, 55–67.
- Cui, H., Pietrzak, J. D., and Stelling, G. S. (2014): Optimal dispersion with minimized Poisson equations for non-hydrostatic free surface flows. *Ocean Modelling*, 81, 1–12.
- Dalrymple, R. A., and Rogers, B. D. (2006): Numerical modeling of water waves with the SPH method. *Coastal Engineering*, 53 (2-3), 141–147.
- De Bakker, A. T. M., Herbers, T. H. C., Smit, P. B., Tissier, M. F. S., and Ruessink, B. G. (2015): Nonlinear infragravity-wave interactions on a gently sloping laboratory beach. *Journal of Physical Oceanography*, 45, 589–605.
- De Bakker, A. T. M., Tissier, M. F. S., and Ruessink, B. G. (2014): Shoreline dissipation of infragravity waves. *Continental Shelf Research*, 72, 73–82.
- De Bakker, A. T. M., Tissier, M. F. S., and Ruessink, B. G. (2016): Beach steepness effects on nonlinear infragravity-wave interactions: A numerical study. *Journal of Geophysical Research: Oceans*, 121 (1), 554–570.
- De Hauteclocque, G., Rezende, F., Waals, O., and Chen, X.-B. (2012): Review of approximations to evaluate second-order low-frequency loads. In: *Proceedings of the 31st International Conference on Ocean, Offshore and Arctic Engineering*, ASME, 363–371.

- De Jong, M. P. C., Borsboom, M. J. A., and Dekker, J. (2009): Calculation of low-frequency waves in shallow water and comparison to common practice in diffraction methods. In: *Proceedings of the 28th International Conference on Ocean, Offshore and Arctic Engineering*, ASME, 395–405.
- Diaz-Hernandez, G., Mendez, F. J., Losada, I. J., Camus, P., and Medina, R. (2015): A nearshore long-term infragravity wave analysis for open harbours. *Coastal Engineering*, 97, 78–90.
- Dingemans, M. W. (1994): Water wave propagation over uneven bottoms. Ph.D. thesis, Delft University of Technology.
- Dobrochinski, J. P. H. (2014): A combination of SWASH and Harberth to compute wave forces on moored ships. M.Sc. thesis, Delft University of Technology.
- Eatock Taylor, R., and Chau, F. P. (1992): Wave diffraction theory – some developments in linear and nonlinear theory. *Journal of Offshore Mechanics and Arctic Engineering*, 114 (3), 185–194.
- Eldeberky, Y. (1996): Nonlinear transformation of wave spectra in the nearshore. Ph.D. thesis, Delft University of Technology.
- Fang, K., Liu, Z., and Zou, Z. (2015): Efficient computation of coastal waves using a depth-integrated, non-hydrostatic model. *Coastal Engineering*, 97, 21–36.
- Farahani, R. J., and Dalrymple, R. A. (2014): Three-dimensional reversed horseshoe vortex structures under broken solitary waves. *Coastal Engineering*, 91, 261–279.
- Feddersen, F. (2014): The generation of surfzone eddies in a strong alongshore current. *Journal of Physical Oceanography*, 44 (2), 600–617.
- Feddersen, F., Clark, D. B., and Guza, R. T. (2011): Modeling surf zone tracer plumes: 1. Waves, mean currents, and low-frequency eddies. *Journal of Geophysical Research*, 116 (C11).
- Feddersen, F., Gallagher, E. L., Guza, R. T., and Elgar, S. (2003): The drag coefficient, bottom roughness, and wave-breaking in the nearshore. *Coastal Engineering*, 48 (3), 189–195.
- Feddersen, F., Guza, R. T., Elgar, S., and Herbers, T. H. C. (1998): Alongshore momentum balances in the nearshore. *Journal of Geophysical Research*, 103 (C8), 15 667–15 676.
- Gómez-Gesteira, M., Cerqueiro, D., Crespo, C., and Dalrymple, R. A. (2005): Green water overtopping analyzed with a SPH model. *Ocean Engineering*, 32 (2), 223–238.
- González-Marco, D., Sierra, J. P., Fernández de Ybarra, O., and Sánchez-Arcilla, A. (2008): Implications of long waves in harbor management: The Gijón port case study. *Ocean & Coastal Management*, 51 (2), 180–201.

- Guedes, R. M. C., Bryan, K. R., and Coco, G. (2013): Observations of wave energy fluxes and swash motions on a low-sloping, dissipative beach. *Journal of Geophysical Research: Oceans*, 118 (7), 3651–3669.
- Guza, R. T., and Thornton, E. B. (1982): Swash oscillations on a natural beach. *Journal of Geophysical Research*, 87 (C1), 483–491.
- Guza, R. T., and Thornton, E. B. (1985): Observations of surf beat. *Journal of Geophysical Research*, 90 (C2), 3161–3172.
- Hadžić, I., Hennig, J., Perić, M., and Xing-Kaeding, Y. (2005): Computation of flow-induced motion of floating bodies. *Applied Mathematical Modelling*, 29 (12), 1196–1210.
- Harlow, F. H., and Welch, J. E. (1965): Numerical calculation of time-dependent viscous incompressible flow of fluid with free surface. *Physics of Fluids*, 8, 2182–2189.
- Hasselmann, K. (1962): On the non-linear energy transfer in a gravity-wave spectrum: Part 1. General theory. *Journal of Fluid Mechanics*, 12 (4), 481–500.
- Hasselmann, K. (1974): On the spectral dissipation of ocean waves due to white capping. *Boundary-Layer Meteorology*, 6 (1-2), 107–127.
- Hasselmann, S., and Hasselmann, K. (1985): Computations and parameterizations of the nonlinear energy transfer in a gravity-wave spectrum. Part I: a new method for efficient computations of the exact nonlinear transfer integral. *Journal of Physical Oceanography*, 15 (11), 1369–1377.
- Henderson, S. M., and Bowen, A. J. (2002): Observations of surf beat forcing and dissipation. *Journal of Geophysical Research*, 107 (C11).
- Henderson, S. M., Guza, R. T., Elgar, S., Herbers, T. H. C., and Bowen, A. J. (2006): Nonlinear generation and loss of infragravity wave energy. *Journal of Geophysical Research*, 111 (C12).
- Herbers, T. H. C., Elgar, S., and Guza, R. T. (1995): Generation and propagation of infragravity waves. *Journal of Geophysical Research*, 100 (C12), 24 863–24 872.
- Hess, J. L., and Smith, A. M. (1962): Calculation of non-lifting potential flow about arbitrary three-dimensional bodies. Tech. rep., Douglas Aircraft Division, Long Beach, California, 190 pp.
- Hibberd, S., and Peregrine, D. H. (1979): Surf and run-up on a beach: a uniform bore. *Journal of Fluid Mechanics*, 95 (2), 323–345.
- Higuera, P., Lara, J. L., and Losada, I. J. (2014): Three-dimensional interaction of waves and porous coastal structures using OpenFOAM®. Part I: Formulation and validation. *Coastal Engineering*, 83, 243–258.
- Hirt, C. W., and Nichols, B. D. (1981): Volume of fluid (VOF) method for the dynamics of free boundaries. *Journal of Computational Physics*, 39 (1), 201–225.

- Holthuijsen, L. H. (2007): *Waves in oceanic and coastal waters*. Cambridge University Press.
- Hong, S. Y., Kim, J. H., Cho, S. K., Choi, Y. R., and Kim, Y. S. (2005): Numerical and experimental study on hydrodynamic interaction of side-by-side moored multiple vessels. *Ocean Engineering*, 32 (7), 783–801.
- Howd, P. A., Bowen, A. J., and Holman, R. A. (1992): Edge waves in the presence of strong longshore currents. *Journal of Geophysical Research*, 97 (C7), 11 357–11 371.
- Howd, P. A., Oltman-Shay, J., and Holman, R. A. (1991): Wave variance partitioning in the trough of a barred beach. *Journal of Geophysical Research*, 96 (C7), 12 781–12 795.
- Huijsmans, R. H. M., Pinkster, J. A., and de Wilde, J. J. (2001): Diffraction and radiation of waves around side-by-side moored vessels. In: *The Eleventh International Offshore and Polar Engineering Conference*, ISOPE.
- Huntley, D. A., Guza, R. T., and Thornton, E. B. (1981): Field observations of surf beat: 1. Progressive edge waves. *Journal of Geophysical Research*, 86 (C7), 6451–6466.
- Jacobsen, N. G., Van Gent, M. R. A., and Wolters, G. (2015): Numerical analysis of the interaction of irregular waves with two dimensional permeable coastal structures. *Coastal Engineering*, 102, 13–29.
- Janssen, T., and Battjes, J. (2007): A note on wave energy dissipation over steep beaches. *Coastal Engineering*, 54 (9), 711–716.
- Janssen, T. T., Battjes, J. A., and Van Dongeren, A. R. (2003): Long waves induced by short-wave groups over a sloping bottom. *Journal of Geophysical Research*, 108 (C8).
- Jiang, T., Henn, R., and Sharma, S. D. (2002): Wash waves generated by ships moving on fairways of varying topography. In: *24th Symposium on Naval Hydrodynamics*, NAP, Vol. 2, 8–13.
- Johnson, D., and Pattiaratchi, C. (2006): Boussinesq modelling of transient rip currents. *Coastal Engineering*, 53 (5-6), 419–439.
- Karambas, T. V., and Koutitas, C. (1992): A breaking wave propagation model based on the Boussinesq equations. *Coastal Engineering*, 18 (1-2), 1–19.
- Kennedy, A. B., Chen, Q., Kirby, J. T., and Dalrymple, R. A. (2000): Boussinesq modeling of wave transformation, breaking, and runup. I: 1D. *Journal of Waterway, Port, Coastal, and Ocean Engineering*, 126 (1), 39–47.
- Kenyon, K. E. (1972): Edge waves with current shear. *Journal of Geophysical Research*, 77 (33), 6599–6603.
- Kevorkian, J., and Cole, J. D. (1981): *Perturbation methods in applied mathematics*, Applied Mathematical Sciences, Vol. 34. Springer New York, New York, NY, 558 pp.

- Kirby, J. T. (1997): Nonlinear, dispersive long waves in water of variable depth. In: *Gravity waves in water of finite depth*, J. N. Hunt, Ed., Computational Mechanics Publications, chap. 3, 55–125.
- Kirby, J. T. (2003): Boussinesq models and applications to nearshore wave propagation, surf zone processes and wave-induced currents. In: *Advances in Coastal Modeling*, V. C. Lakhan, Ed., Vol. 67, Elsevier, chap. 1, 1–41.
- Kirby, J. T., and Dalrymple, R. A. (1983): A parabolic equation for the combined refraction–diffraction of Stokes waves by mildly varying topography. *Journal of Fluid Mechanics*, 136, 453–466.
- Kirby, J. T., and Dalrymple, R. A. (1986): Modeling waves in surfzones and around islands. *Journal of Waterway, Port, Coastal, and Ocean Engineering*, 112 (1), 78–93.
- Kirby, J. T., Dalrymple, R. A., and Liu, P. L.-F. (1981): Modification of edge waves by barred-beach topography. *Coastal Engineering*, 5, 35–49.
- Kleefsman, K. M. T., Fekken, G., Veldman, A. E. P., Iwanowski, B., and Buchner, B. (2005): A Volume-of-Fluid based simulation method for wave impact problems. *Journal of Computational Physics*, 206 (1), 363–393.
- Kobayashi, N., DeSilva, G. S., and Watson, K. D. (1989): Wave transformation and swash oscillation on gentle and steep slopes. *Journal of Geophysical Research*, 94 (C1), 951–966.
- Korvin-Kroukovsky, B. V., and Jacobs, W. R. (1957): Pitching and heaving motions of a ship in regular waves. *Transactions of The Society of Naval Architects and Marine Engineers*, 65, 590–632.
- Kuik, A. J., Van Vledder, G. P., and Holthuijsen, L. H. (1988): A method for the routine analysis of pitch-and-roll buoy wave data. *Journal of Physical Oceanography*, 18 (7), 1020–1034.
- Lam, D. C. L., and Simpson, R. B. (1976): Centered differencing and the box scheme for diffusion convection problems. *Journal of Computational Physics*, 22 (4), 486–500.
- Lamb, H. (1932): *Hydrodynamics*. Cambridge university press, 768 pp.
- Lara, J. L., Ruju, A., and Losada, I. J. (2011): Reynolds averaged Navier-Stokes modelling of long waves induced by a transient wave group on a beach. *Proceedings of the Royal Society A: Mathematical, Physical and Engineering Sciences*, 467 (2129), 1215–1242.
- Lin, P. (2006): A multiple-layer σ -coordinate model for simulation of wave–structure interaction. *Computers & Fluids*, 35 (2), 147–167.
- Lin, P. (2007): A fixed-grid model for simulation of a moving body in free surface flows. *Computers & Fluids*, 36 (3), 549–561.
- Lin, P., and Liu, P. L.-F. (1998): A numerical study of breaking waves in the surf zone. *Journal of Fluid Mechanics*, 359, 239–264.

- Lippmann, T. C., Herbers, T. H. C., and Thornton, E. B. (1999): Gravity and shear wave contributions to nearshore infragravity motions. 231–239 pp.
- List, J. H. (1992): A model for the generation of two-dimensional surf beat. *Journal of Geophysical Research*, 97 (C4), 5623–5635.
- Liu, Y., Xue, M., and Yue, D. K. P. (2001): Computations of fully nonlinear three-dimensional wave-wave and wave-body interactions. Part 2. Nonlinear waves and forces on a body. *Journal of Fluid Mechanics*, 438, 41–66.
- Longuet-Higgins, M. S., and Stewart, R. W. (1960): Changes in the form of short gravity waves on long waves and tidal currents. *Journal of Fluid Mechanics*, 8 (4), 565–583.
- Longuet-Higgins, M. S., and Stewart, R. W. (1962): Radiation stress and mass transport in gravity waves, with application to ‘surf beats’. *Journal of Fluid Mechanics*, 13 (4), 481–504.
- Longuet-Higgins, M. S., and Stewart, R. W. (1964): Radiation stresses in water waves; a physical discussion, with applications. *Deep Sea Research*, 11, 529–562.
- López, M., and Iglesias, G. (2014): Long wave effects on a vessel at berth. *Applied Ocean Research*, 47, 63–72.
- Lynett, P., and Liu, P. L.-F. (2004): A two-layer approach to wave modelling. *Proceedings of the Royal Society A: Mathematical, Physical and Engineering Sciences*, 460 (2049).
- Lynett, P. J., Wu, T.-R., and Liu, P. L.-F. (2002): Modeling wave runup with depth-integrated equations. *Coastal Engineering*, 46 (2), 89–107.
- Ma, G., Shi, F., Hsiao, S.-C., and Wu, Y.-T. (2014a): Non-hydrostatic modeling of wave interactions with porous structures. *Coastal Engineering*, 91, 84–98.
- Ma, G., Shi, F., and Kirby, J. T. (2012): Shock-capturing non-hydrostatic model for fully dispersive surface wave processes. *Ocean Modelling*, 43-44, 22–35.
- Ma, G., Su, S.-F., Liu, S., and Chu, J.-C. (2014b): Numerical simulation of infragravity waves in fringing reefs using a shock-capturing non-hydrostatic model. *Ocean Engineering*, 85, 54–64.
- Ma, Q. W., Wu, G. X., and Eatock Taylor, R. (2001a): Finite element simulation of fully non-linear interaction between vertical cylinders and steep waves. Part 1: methodology and numerical procedure. *International Journal for Numerical Methods in Fluids*, 36 (3), 265–285.
- Ma, Q. W., Wu, G. X., and Eatock Taylor, R. (2001b): Finite element simulations of fully non-linear interaction between vertical cylinders and steep waves. Part 2: numerical results and validation. *International Journal for Numerical Methods in Fluids*, 36 (3), 287–308.

- Ma, Q. W., and Yan, S. (2009): QALE-FEM for numerical modelling of non-linear interaction between 3D moored floating bodies and steep waves. *International Journal for Numerical Methods in Engineering*, 78 (6), 713–756.
- MacMahan, J. H., Reniers, A. J. H. M., Thornton, E. B., and Stanton, T. P. (2004): Surf zone eddies coupled with rip current morphology. *Journal of Geophysical Research: Oceans*, 109 (7).
- Madsen, P. A. (1983): Wave reflection from a vertical permeable wave absorber. *Coastal Engineering*, 7 (4), 381–396.
- Madsen, P. A., Murray, R., and Sørensen, O. R. (1991): A new form of the Boussinesq equations with improved linear dispersion characteristics. *Coastal Engineering*, 15 (4), 371–388.
- Madsen, P. A., and Sørensen, O. R. (1992): A new form of the Boussinesq equations with improved linear dispersion characteristics. Part 2. A slowly-varying bathymetry. *Coastal Engineering*, 18 (3-4), 183–204.
- Madsen, P. A., and Sørensen, O. R. (1993): Bound waves and triad interactions in shallow water. *Ocean Engineering*, 20 (4), 359–388.
- Madsen, P. A., Sørensen, O. R., and Schäffer, H. A. (1997): Surf zone dynamics simulated by a Boussinesq type model. Part II: surf beat and swash oscillations for wave groups and irregular waves. *Coastal Engineering*, 32 (4), 289–319.
- Mahadevan, A., Oliger, J., and Street, R. (1996): A nonhydrostatic mesoscale ocean model. Part II: numerical implementation. *Journal of Physical Oceanography*, 26 (9), 1881–1900.
- Marshall, J., Hill, C., Perelman, L., and Adcroft, A. (1997): Hydrostatic, quasi-hydrostatic, and nonhydrostatic ocean modeling. *Journal of Geophysical Research: Oceans*, 102 (C3), 5733–5752.
- Masselink, G. (1995): Group bound long waves as a source of infragravity energy in the surf zone. *Continental Shelf Research*, 15 (13), 1525–1547.
- Mei, C. C., Stiassnie, M., and Yue, D. K.-P. (2005): *Theory and applications of ocean surface waves*, Vol. 23. World Scientific.
- Miles, J. W. (1957): On the generation of surface waves by shear flows. *Journal of Fluid Mechanics*, 3 (02), 185.
- Miles, M. D., and Funke, E. R. (1989): A comparison of methods for synthesis of directional seas. *Journal of Offshore Mechanics and Arctic Engineering*, 111 (1), 43–48.
- Mofidi, A., and Carrica, P. M. (2014): Simulations of zigzag maneuvers for a container ship with direct moving rudder and propeller. *Computers & Fluids*, 96, 191–203.
- Molin, B. (1979): Second-order diffraction loads upon three-dimensional bodies. *Applied Ocean Research*, 1 (4), 197–202.

- Monaghan, J. J. (1994): Simulating free surface flows with SPH. *Journal of Computational Physics*, 110 (2), 399–406.
- Morison, M. L., and Imberger, J. (1992): Water Level Oscillations in Esperance Harbour. American Society of Civil Engineers, 352–367 pp.
- Mousaviraad, S. M., Sadat-Hosseini, S. H., Carrica, P. M., and Stern, F. (2016): Ship–Ship interactions in calm water and waves. Part 2: URANS validation in replenishment and overtaking conditions. *Ocean Engineering*, 111, 627–638.
- Munk, W. H. (1949): Surf beats. *Transactions, American Geophysical Union*, 30 (6), 849.
- Naciri, M., Buchner, B., Bunnik, T., Huijsmans, R., and Andrews, J. (2004): Low frequency motions of LNG carriers moored in shallow water. In: *23rd International Conference on Offshore Mechanics and Arctic Engineering, Volume 3*, ASME, 995–1006.
- Newman, J. N. (1974): Second-order, slowly-varying forces on vessels in irregular waves. In: *Proceedings of the symposium on the dynamics of marine vehicles and structures in waves*, R. Biship, and W. G. Price, Eds., Mechanical Engineering Publications Limited, London, 182–186.
- Newman, J. N. (1977): *Marine hydrodynamics*. MIT press, 432 pp.
- Newman, J. N. (1985): Algorithms for the free-surface Green function. *Journal of Engineering Mathematics*, 19 (1), 57–67.
- Newman, J. N. (2005): Efficient hydrodynamic analysis of very large floating structures. *Marine Structures*, 18 (2), 169–180.
- Newman, J. N., and Lee, C.-H. (2002): Boundary-element methods in offshore structure analysis. *Journal of Offshore Mechanics and Arctic Engineering*, 124 (2), 81–89.
- Nwogu, O. (1993): Alternative Form of Boussinesq Equations for Nearshore Wave Propagation. *Journal of Waterway, Port, Coastal, and Ocean Engineering*, 119 (6), 618–638.
- Ohyama, T., and Tsuchida, M. (1997): Expanded mild-slope equations for the analysis of wave-induced ship motion in a harbor. *Coastal Engineering*, 30 (1-2), 77–103.
- Okihiro, M., Guza, R. T., and Seymour, R. J. (1992): Bound infragravity waves. *Journal of Geophysical Research*, 97 (C7), 11 453–11 469.
- Okihiro, M., Guza, R. T., and Seymour, R. J. (1993): Excitation of seiche observed in a small harbor. *Journal of Geophysical Research*, 98 (C10), 18 201–18 211.
- Oltman-Shay, J., and Guza, R. T. (1987): Infragravity edge wave observations on two California beaches. *Journal of Physical Oceanography*, 17 (5), 644–663.
- Osher, S., and Sethian, J. A. (1988): Fronts propagating with curvature-dependent speed: Algorithms based on Hamilton-Jacobi formulations. *Journal of Computational Physics*, 79 (1), 12–49.

- Özkan-Haller, H. T., and Kirby, J. T. (1999): Nonlinear evolution of shear instabilities of the longshore current: A comparison of observations and computations. *Journal of Geophysical Research*, 104 (C11), 25 953–25 984.
- Panchang, V., Chen, W., Xu, B., Schlenker, K., Demirbilek, Z., and Okihiro, M. (2000): Exterior bathymetric effects in elliptic harbor wave models. *Journal of Waterway, Port, Coastal, and Ocean Engineering*, 126 (2), 71–78.
- Péquignet, A.-C. N., Becker, J. M., and Merrifield, M. A. (2014): Energy transfer between wind waves and low-frequency oscillations on a fringing reef, Ipan, Guam. *Journal of Geophysical Research: Oceans*, 119 (10), 6709–6724.
- Peregrine, D. H. (1967): Long waves on a beach. *Journal of Fluid Mechanics*, 27 (4), 815–827.
- Pessoa, J., and Fonseca, N. (2013): Investigation of depth effects on the wave exciting low frequency drift forces by different approximation methods. *Applied Ocean Research*, 42, 182–199.
- Phillips, O. M. (1957): On the generation of waves by turbulent wind. *Journal of Fluid Mechanics*, 2 (5), 417–445.
- Pinkster, J. A. (1980): Low frequency second order wave exciting forces on floating structures. Ph.D. thesis, Delft University of Technology.
- Pomeroy, A., Lowe, R., Symonds, G., Van Dongeren, A., and Moore, C. (2012): The dynamics of infragravity wave transformation over a fringing reef. *Journal of Geophysical Research*, 117 (C11).
- Ren, B., He, M., Dong, P., and Wen, H. (2015): Nonlinear simulations of wave-induced motions of a freely floating body using WCSPH method. *Applied Ocean Research*, 50, 1–12.
- Reniers, A. J. H. M. (2004): Morphodynamic modeling of an embayed beach under wave group forcing. *Journal of Geophysical Research*, 109 (C1).
- Reniers, A. J. H. M., Groenewegen, M. J., Ewans, K. C., Masterton, S., Stelling, G. S., and Meeck, J. (2010): Estimation of infragravity waves at intermediate water depth. *Coastal Engineering*, 57 (1), 52–61.
- Reniers, A. J. H. M., MacMahan, J. H., Thornton, E. B., and Stanton, T. P. (2006): Modelling infragravity motions on a rip-channel beach. *Coastal Engineering*, 53 (2-3), 209–222.
- Reniers, A. J. H. M., MacMahan, J. H., Thornton, E. B., and Stanton, T. P. (2007): Modeling of very low frequency motions during RIPEX. *Journal of Geophysical Research*, 112 (C7).
- Reniers, A. J. H. M., Van Dongeren, A. R., Battjes, J. A., and Thornton, E. B. (2002): Linear modeling of infragravity waves during Delilah. *Journal of Geophysical Research*, 107 (C10).

- Rijnsdorp, D. P., Ruessink, G., and Zijlema, M. (2015a): Infragravity-wave dynamics in a barred coastal region, a numerical study. *Journal of Geophysical Research: Oceans*, 120 (6), 4068–4089.
- Rijnsdorp, D. P., Smit, P. B., and Zijlema, M. (2012): Non-hydrostatic modelling of infragravity waves using SWASH. In: *Coastal Engineering Proceedings*.
- Rijnsdorp, D. P., Smit, P. B., and Zijlema, M. (2014): Non-hydrostatic modelling of infragravity waves under laboratory conditions. *Coastal Engineering*, 85, 30–42.
- Rijnsdorp, D. P., and Zijlema, M. (2013): Numerical modelling of interactions between non-hydrostatic free-surface flows and a non-moving floating body. In: *Proceedings of the 35th IAHR World Congress*.
- Rijnsdorp, D. P., and Zijlema, M. (2016): Simulating waves and their interactions with a restrained ship using a non-hydrostatic wave-flow model. *Coastal Engineering*, 114, 119–136.
- Rijnsdorp, D. P., Zijlema, M., and Pietrzak, J. D. (2015b): Predicting wave-induced loads on a moored ship with a non-hydrostatic wave-flow model. In: *Proceedings of the 36th IAHR World Congress*.
- Roelvink, D., Reniers, A., Van Dongeren, A., Van Thiel de Vries, J., McCall, R., and Lescinski, J. (2009): Modelling storm impacts on beaches, dunes and barrier islands. *Coastal Engineering*, 56 (11-12), 1133–1152.
- Ruessink, B. G. (2010): Observations of turbulence within a natural surf zone. *Journal of Physical Oceanography*, 40 (12), 2696–2712.
- Ruessink, B. G., Miles, J. R., Feddersen, F., Guza, R. T., and Elgar, S. (2001): Modeling the alongshore current on barred beaches. *Journal of Geophysical Research*, 106 (C10), 22 451–22 463.
- Ruessink, B. G., Van Enckevort, I. M. J., Kingston, K. S., and Davidson, M. A. (2000): Analysis of observed two- and three-dimensional nearshore bar behaviour. *Marine Geology*, 169 (1-2), 161–183.
- Ruju, A., Lara, J. L., and Losada, I. J. (2012): Radiation stress and low-frequency energy balance within the surf zone: A numerical approach. *Coastal Engineering*, 68, 44–55.
- Ruju, A., Lara, J. L., and Losada, I. J. (2014): Numerical analysis of run-up oscillations under dissipative conditions. *Coastal Engineering*, 86, 45–56.
- Russell, P. E. (1993): Mechanisms for beach erosion during storms. *Continental Shelf Research*, 13 (11), 1243–1265.
- Sakakibara, S., and Kubo, M. (2008): Characteristics of low-frequency motions of ships moored inside ports and harbors on the basis of field observations. *Marine Structures*, 21 (2-3), 196–223.

- Salmon, J. E., Holthuijsen, L. H., Zijlema, M., Van Vledder, G. P., and Pietrzak, J. D. (2015): Scaling depth-induced wave-breaking in two-dimensional spectral wave models. *Ocean Modelling*, 87, 30–47.
- Schäffer, H. A., Madsen, P. A., and Deigaard, R. (1993): A Boussinesq model for waves breaking in shallow water. *Coastal Engineering*, 20 (3-4), 185–202.
- Schönfeldt, H.-J. (1994): Randwellen in der Ostsee und anomale Dispersion in der Brandungszone. *Deutsche Hydrographische Zeitschrift*, 46 (1), 81–98.
- Sheremet, A., Guza, R. T., Elgar, S., and Herbers, T. H. C. (2002): Observations of nearshore infragravity waves: Seaward and shoreward propagating components. *Journal of Geophysical Research*, 107 (C8).
- Sheremet, A., Guza, R. T., and Herbers, T. H. C. (2005): A new estimator for directional properties of nearshore waves. *Journal of Geophysical Research*, 110 (C1).
- Shimozono, T., Cui, H., Pietrzak, J. D., Fritz, H. M., Okayasu, A., and Hooper, A. J. (2014): Short wave amplification and extreme runup by the 2011 Tohoku tsunami. *Pure and Applied Geophysics*, 171 (12), 3217–3228.
- Smagorinsky, J. (1963): General circulation experiments with the primitive equations. *Monthly Weather Review*, 91 (3), 99–164.
- Smit, P., Janssen, T., Holthuijsen, L., and Smith, J. (2014): Non-hydrostatic modeling of surf zone wave dynamics. *Coastal Engineering*, 83, 36–48.
- Smit, P., Zijlema, M., and Stelling, G. (2013): Depth-induced wave breaking in a non-hydrostatic, near-shore wave model. *Coastal Engineering*, 76, 1–16.
- Smit, P. B. (2014): Deterministic and stochastic modelling of ocean surface waves. Ph.D. thesis, Delft University of Technology.
- Smit, P. B., Janssen, T. T., and Herbers, T. H. C. (2015a): Stochastic modeling of coherent wave fields over variable depth. *Journal of Physical Oceanography*, 45 (4), 1139–1154.
- Smit, P. B., Janssen, T. T., and Herbers, T. H. C. (2015b): Stochastic modeling of inhomogeneous ocean waves. *Ocean Modelling*, 96, 26–35.
- Stansby, P. K., and Zhou, J. G. (1998): Shallow-water flow solver with non-hydrostatic pressure: 2D vertical plane problems. *International Journal for Numerical Methods in Fluids*, 28 (3), 541–563.
- Stelling, G., and Zijlema, M. (2003): An accurate and efficient finite-difference algorithm for non-hydrostatic free-surface flow with application to wave propagation. *International Journal for Numerical Methods in Fluids*, 43 (1), 1–23.
- Stelling, G. S., and Duinmeijer, S. P. A. (2003): A staggered conservative scheme for every Froude number in rapidly varied shallow water flows. *International Journal for Numerical Methods in Fluids*, 43 (12), 1329–1354.

- Stern, F., Yang, J., Wang, Z., Sadat-Hosseini, H., Mousaviraad, M., Bhushan, S., and Xing, T. (2013): Computational ship hydrodynamics: Nowadays and way forward. *International Shipbuilding Progress*, 60 (1-4), 3–105.
- Symonds, G., Huntley, D. A., and Bowen, A. J. (1982): Two-dimensional surf beat: Long wave generation by a time-varying breakpoint. *Journal of Geophysical Research*, 87 (C1), 492–498.
- Thomson, J., Elgar, S., Raubenheimer, B., Herbers, T. H. C., and Guza, R. T. (2006): Tidal modulation of infragravity waves via nonlinear energy losses in the surfzone. *Geophysical Research Letters*, 33 (5).
- Tissier, M., Bonneton, P., Marche, F., Chazel, F., and Lannes, D. (2012): A new approach to handle wave breaking in fully non-linear Boussinesq models. *Coastal Engineering*, 67, 54–66.
- Tolman, H. L. (1991): A third-generation model for wind waves on slowly varying, unsteady, and inhomogeneous depths and currents. *Journal of Physical Oceanography*, 21 (6), 782–797.
- Tonelli, M., and Petti, M. (2012): Shock-capturing Boussinesq model for irregular wave propagation. *Coastal Engineering*, 61, 8–19.
- Torres-Freyermuth, A., Lara, J. L., and Losada, I. J. (2010): Numerical modelling of short- and long-wave transformation on a barred beach. *Coastal Engineering*, 57 (3), 317–330.
- Tucker, M. J. (1950): Surf beats: sea waves of 1 to 5 min. period. *Proceedings of the Royal Society A: Mathematical, Physical and Engineering Sciences*, 202 (1071), 565–573.
- Van der Molen, W. (2006): Behaviour of moored ships in harbours. Ph.D. thesis, Delft University of Technology.
- Van der Molen, W., Monardez, P., and Van Dongeren, A. (2006): Numerical simulation of long-period waves and ship motions in Tomakomai port, Japan. *Coastal Engineering Journal*, 48 (1), 59–79.
- Van der Molen, W., and Wenneker, I. (2008): Time-domain calculation of moored ship motions in nonlinear waves. *Coastal Engineering*, 55 (5), 409–422.
- Van Dongeren, A., Battjes, J., Janssen, T., van Noorloos, J., Steenhauer, K., Steenbergen, G., and Reniers, A. (2007): Shoaling and shoreline dissipation of low-frequency waves. *Journal of Geophysical Research*, 112 (C2).
- Van Dongeren, A., Lowe, R., Pomeroy, A., Trang, D. M., Roelvink, D., Symonds, G., and Ranasinghe, R. (2013): Numerical modeling of low-frequency wave dynamics over a fringing coral reef. *Coastal Engineering*, 73, 178–190.
- Van Dongeren, A., Reniers, A., Battjes, J., and Svendsen, I. (2003): Numerical modeling of infragravity wave response during DELILAH. *Journal of Geophysical Research*, 108 (C9).

- Van Kan, J. (1986): A second-order accurate pressure-correction scheme for viscous incompressible flow. *SIAM Journal on Scientific and Statistical Computing*, 7 (3), 870–891.
- Van Leer, B. (1979): Towards the ultimate conservative difference scheme. V. A second-order sequel to Godunov's method. *Journal of Computational Physics*, 32 (1), 101–136.
- Van Noorloos, J. C. (2003): Energy transfer between short wave groups and bound long waves on a plane slope. M.S. thesis, Delft University of Technology.
- Van Oortmerssen, G. (1976): The motions of a ship in shallow water. *Ocean Engineering*, 3 (4), 221–255.
- Van Thiel de Vries, J. S. M., Van Gent, M. R. A., Walstra, D. J. R., and Reniers, A. J. H. M. (2008): Analysis of dune erosion processes in large-scale flume experiments. *Coastal Engineering*, 55 (12), 1028–1040.
- Van Vledder, G. P., Ruessink, G., and Rijnsdorp, D. P. (2013): Individual wave height distributions in the coastal zone: Measurements and simulations and the effect of directional spreading. In: *Coastal Dynamics Proceedings*.
- Veldman, A. E. P., et al. (2011): Extreme wave impact on offshore platforms and coastal constructions. In: *Proceedings of the 30th International Conference on Ocean, Offshore and Arctic Engineering*, ASME, 365–376.
- Vitousek, S., and Fringer, O. B. (2013): Stability and consistency of nonhydrostatic free-surface models using the semi-implicit θ -method. *International Journal for Numerical Methods in Fluids*, 72 (5), 550–582.
- Vitousek, S., and Fringer, O. B. (2014): A nonhydrostatic, isopycnal-coordinate ocean model for internal waves. *Ocean Modelling*, 83, 118–144.
- Walters, R. A. (2005): A semi-implicit finite element model for non-hydrostatic (dispersive) surface waves. *International Journal for Numerical Methods in Fluids*, 49 (7), 721–737.
- Wang, D.-G., Zou, Z.-L., and Tham, L. G. (2011): A 3-D time-domain coupled model for nonlinear waves acting on a box-shaped ship fixed in a harbor. *China Ocean Engineering*, 25 (3), 441–456.
- Webb, S. C., Zhang, X., and Crawford, W. (1991): Infragravity waves in the deep ocean. *Journal of Geophysical Research*, 96 (C2), 2723–2736.
- Wei, G., Kirby, J. T., Grilli, S. T., and Subramanya, R. (1995): A fully nonlinear Boussinesq model for surface waves. Part 1. Highly nonlinear unsteady waves. *Journal of Fluid Mechanics*, 294, 71–92.
- Wei, G., Kirby, J. T., and Sinha, A. (1999): Generation of waves in Boussinesq models using a source function method. *Coastal Engineering*, 36 (4), 271–299.

- Wei, Z., and Jia, Y. (2014): Non-hydrostatic finite element model for coastal wave processes. *Coastal Engineering*, 92, 31–47.
- Wilson, R. V., Carrica, P. M., and Stern, F. (2006): Unsteady RANS method for ship motions with application to roll for a surface combatant. *Computers & Fluids*, 35 (5), 501–524.
- Wu, G. X., and Eatock Taylor, R. (1995): Time stepping solutions of the two-dimensional nonlinear wave radiation problem. *Ocean Engineering*, 22 (8), 785–798.
- Xiong, L., Lu, H., Yang, J., and Zhao, W. (2015): Motion responses of a moored barge in shallow water. *Ocean Engineering*, 97, 207–217.
- Yamazaki, Y., Cheung, K. F., and Kowalik, Z. (2011): Depth-integrated, non-hydrostatic model with grid nesting for tsunami generation, propagation, and run-up. *International Journal for Numerical Methods in Fluids*, 67 (12), 2081–2107.
- Yamazaki, Y., Kowalik, Z., and Cheung, K. F. (2009): Depth-integrated, non-hydrostatic model for wave breaking and run-up. *International Journal for Numerical Methods in Fluids*, 61 (5), 473–497.
- Yan, S., and Ma, Q. (2007): Numerical simulation of fully nonlinear interaction between steep waves and 2D floating bodies using the QALE-FEM method. *Journal of Computational Physics*, 221 (2), 666–692.
- You, J., and Faltinsen, O. M. (2015): A numerical investigation of second-order difference-frequency forces and motions of a moored ship in shallow water. *Journal of Ocean Engineering and Marine Energy*, 1 (2), 157–179.
- Zelt, J. A. (1991): The run-up of nonbreaking and breaking solitary waves. *Coastal Engineering*, 15 (3), 205–246.
- Zhao, W. H., Yang, J. M., Hu, Z. Q., and Wei, Y. F. (2011): Recent developments on the hydrodynamics of floating liquid natural gas (FLNG). *Ocean Engineering*, 38 (14-15), 1555–1567.
- Zhou, B. Z., and Wu, G. X. (2014): Resonance of a tension leg platform excited by third-harmonic force in nonlinear regular waves. *Philosophical Transactions of the Royal Society A: Mathematical, Physical and Engineering Sciences*, 373 (2033).
- Zhou, Z., Sangermano, J., Hsu, T.-J., and Ting, F. C. K. (2014): A numerical investigation of wave-breaking-induced turbulent coherent structure under a solitary wave. *Journal of Geophysical Research: Oceans*, 119 (10), 6952–6973.
- Zijlema, M., Stelling, G., and Smit, P. (2011): SWASH: An operational public domain code for simulating wave fields and rapidly varied flows in coastal waters. *Coastal Engineering*, 58 (10), 992–1012.
- Zijlema, M., and Stelling, G. S. (2005): Further experiences with computing non-hydrostatic free-surface flows involving water waves. *International Journal for Numerical Methods in Fluids*, 48 (2), 169–197.

Zijlema, M., and Stelling, G. S. (2008): Efficient computation of surf zone waves using the nonlinear shallow water equations with non-hydrostatic pressure. *Coastal Engineering*, 55 (10), 780–790.

ACKNOWLEDGEMENTS

After spending just over a decade at the University of Delft, the time has finally come to finalise my studies. While writing these acknowledgements, I can't help looking back in time, which make me realise that I really enjoyed these last four years of research. During this period, I have shared my time with a great deal of people that in many ways contributed to this thesis, and life in general.

Naturally, this thesis would not have been completed without the aid and support of my supervisors: Julie Pietrzak, Guus Stelling, and Marcel Zijlema. First of all, Guus and Marcel, thank you for initiating the NWO project and granting me the opportunity to start my academic endeavours. Ever since I started modelling waves as a part of my MSc thesis, Marcel has been instrumental in my understanding of these digital waves. Thank you for supporting me over these years, for your careful reading of all my drafts that saw the light of day, but most of all for trusting me with the freedom to find my own way in the world of research. Roughly halfway down the project, Guus retired and Julie stepped in to take over his responsibility. Although retired, I really enjoyed the times that Guus stopped by my office to ask if the ship was floating already. Thank you Julie for taking over, for your guidance throughout these years, and especially for your feedback in the last few months that pushed me just that one step further.

I also like to take the opportunity to thank my co-authors of the papers that compose this thesis. Pieter, thank you for help with Chapter 3 and for our numerous enjoyable discussions on wave dynamics. Gerben, thank you for providing the field data set and your contribution to Chapter 4. I am also grateful for the support of the staff of the section. In particular, I like to thank Ad for the possibility to continue as a researcher right after finishing the final draft of this thesis. Furthermore, I greatly appreciate the assistance and help of the supporting staff, and especially Otti.

By times, the work of a PhD can be quite solitary, were it not for the great atmosphere at the department. I have enjoyed all the lunches, coffee breaks, and the drinks that we shared, be it either in Delft or away on a conference. First of all, the people that I shared an office with deserve some special attention. In sort of chronological order, James, Ocean, Pieter, Gu, and Sabine, thanks for being such great office mates. Thanks also, Xuexue, Victor, Andres, Nicolette, Marion, Adam, Saulo, Vincent, Nils, Sotiria, Steffie, Floris and all others that crossed my path. Thank you all for the great time that we shared at our department.

Besides all the people at university, a lot of others have helped me in one way or another to finish this piece of work. They provided for a great distraction from the daily realms of work. It's refreshing to stop talking about waves (and ships), and to talk about many of the other great things that make life worth living. Thanks Arnold, Claudia, Christiaan, Sander, my study friends and hockey buddies. Sorry for not naming all of you, and if you feel let down by me, please let me make up for it with a beer or two.

Furthermore, I wish to thank my family and family-in-law, but especially my parents, Adriaan and Inge, and my brother Joep. We shared a rocky road with the passing of mum just before I started my studies in Delft, but I take great pride in how we came out stronger. We will never know how life would have been, but I am very grateful for how life has become.

By now, I know that Christiaan and Joep will be my paranimfen. Thanks guys, I am really happy that you will stand next to me during my defence. For the beautiful illustration that covers this work, thanks Jonathan.

Finally, Justine, I truly don't know how to thank you enough. Thank you for bursting my little bubble when I got soaked up by work... Thank you for being there with me, always! We shared quite some time already, but in a way it feels like our adventure is just starting to unfold.

Dirk Rijnsdorp
June 2016

LIST OF PUBLICATIONS

JOURNAL ARTICLES

Rijnsdorp, D. P., Smit, P. B., and Zijlema, M. (2014): Non-hydrostatic modelling of infragravity waves under laboratory conditions. *Coastal Engineering*, 85, 30–42.

Rijnsdorp, D. P., Ruessink, G., and Zijlema, M. (2015a): Infragravity-wave dynamics in a barred coastal region, a numerical study. *Journal of Geophysical Research: Oceans*, 120 (6), 4068–4089.

Rijnsdorp, D. P., and Zijlema, M. (2016): Simulating waves and their interactions with a restrained ship using a non-hydrostatic wave-flow model. *Coastal Engineering*, 114, 119–136.

CONFERENCE PROCEEDINGS

FIRST AUTHOR

Rijnsdorp, D. P., Smit, P. B., and Zijlema, M. (2012): Non-hydrostatic modelling of infragravity waves using SWASH. In: *Coastal Engineering Proceedings*.

Rijnsdorp, D. P., and Zijlema, M. (2013): Numerical modelling of interactions between non-hydrostatic free-surface flows and a non-moving floating body. In: *Proceedings of the 35th IAHR World Congress*.

Rijnsdorp, D. P., Zijlema, M., and Pietrzak, J. D. (2015b): Predicting wave-induced loads on a moored ship with a non-hydrostatic wave-flow model. In: *Proceedings of the 36th IAHR World Congress*.

CO-AUTHOR

Van Vledder, G. P., Ruessink, G., and Rijnsdorp, D. P. (2013): Individual wave height distributions in the coastal zone: Measurements and simulations and the effect of directional spreading. In: *Coastal Dynamics Proceedings*.

CV

After being born on the 13th of December 1986 in Haarlem, I grew up in the nearby village of Santpoort-Zuid. I received my secondary education at the Gymnasium Felisenum in Velsen-Zuid, which I completed in 2005. In September of that same year, I started my academic education (BSc and MSc) in Civil Engineering and Geosciences at the Delft University of Technology. In 2011, I graduated with distinction at the section of Environmental Fluid Mechanics. Following the completion of my MSc study, I started as a PhD student at the same section in December 2011. After finishing my doctoral study in 2016, I continued working for six months at the section of Environment Fluid Mechanics. In October 2016, I will continue my career in academia as a post-doctoral researcher at the University of Western Australia.